Ultrahigh Field Functional Magnetic Resonance Electrical Impedance Tomography (fMREIT) in Neural Activity Imaging

by

Fanrui Fu

A Dissertation Presented in Partial Fulfillment
of the Requirements for the Degree
Doctor of Philosophy

Approved March 2019 by the
Graduate Supervisory Committee:

Rosalind J. Sadleir, Chair
Vikram Kodibagkar
Jeffrey Kleim
Jitendran Muthuswamy
Stephen Helms Tillery

ARIZONA STATE UNIVERSITY

May 2019

ABSTRACT

A direct Magnetic Resonance (MR)-based neural activity mapping technique with high spatial and temporal resolution may accelerate studies of brain functional organization.

The most widely used technique for brain functional imaging is functional Magnetic Resonance Image (fMRI). The spatial resolution of fMRI is high. However, fMRI signals are highly influenced by the vasculature in each voxel and can be affected by capillary orientation and vessel size. Functional MRI analysis may, therefore, produce misleading results when voxels are nearby large vessels. Another problem in fMRI is that hemodynamic responses are slower than the neuronal activity. Therefore, temporal resolution is limited in fMRI. Furthermore, the correlation between neural activity and the hemodynamic response is not fully understood. fMRI can only be considered an indirect method of functional brain imaging.

Another MR-based method of functional brain mapping is neuronal current magnetic resonance imaging (ncMRI), which has been studied over several years. However, the amplitude of these neuronal current signals is an order of magnitude smaller than the physiological noise. Works on ncMRI include simulation, phantom experiments, and studies in tissue including isolated ganglia, optic nerves, and human brains. However, ncMRI development has been hampered due to the extremely small signal amplitude, as well as the presence of confounding signals from hemodynamic changes and other physiological noise.

Magnetic Resonance Electrical Impedance Tomography (MREIT) methods could have the potential for the detection of neuronal activity. In this technique, small external currents are applied to a body during MR scans. This current flow produces a magnetic field as well as an electric field. The altered magnetic flux density along the main magnetic field direction caused by this current flow can be obtained from phase images. When there is neural activity, the conductivity of the neural cell membrane changes and the current paths around the neurons change consequently. Neural spiking activity during external current injection, therefore, causes differential phase accumulation in MR data. Statistical analysis methods can be used to identify neuronal-current-induced magnetic field changes.

ACKNOWLEDGMENTS

It has been the greatest wealth in my life to be able to study at Arizona State University (ASU). ASU not only provided advanced facilities for my research but also offered immense help to my life and career. I appreciate ASU for bringing amazing people around me.

I would like to express my great appreciation to my excellent supervisor Dr. Rosalind Sadleir for her academical and spiritual guidance during the development of my research work. Dr. Sadleir is knowledgeable as well as accommodating. Her guidance is the most important help for me to survive my Ph.D. study.

I would like to express my sincere gratitude to Dr. Vikram Kodibagkar for introducing me to other distinguished scholars and for helping me with my career planning. Dr. Kodibagkar also brought constructive ideas for experimental design and inspired me to think about new solutions.

I sincerely appreciate my dissertation committee. Dr. Jeffrey Kleim's neural plasticity class was the first neurological class I took. This class brought me into the world of neuroscience and stirred up my interest in it. I want to thank Dr. Stephen Helms Tillery and Dr. Jitendran Muthuswamy for their encouragement and insightful comments. Their feedback helped me grow professionally. Through their suggestions, I was able to narrow down my research.

Dr. Munish Chauhan is not only my senior but also my good friend. I will never forget the nights we spent together at Barrow Neurological Institute and Magnetic

Resonance Research Center at ASU collecting data and completing experiments. Dr. Chauhan helped me a lot and always selflessly shared his knowledge with me.

I would like to thank my comrades in Lab: Aprinda Indahlastari, Steven Keim, Neeta Kumar, Sulagna Sahu, Dr. Saurav Zaman Khan Sajib, and Dr. Benjamin Schwartz for their support and kindness.

I would like to thank Brian R. Cherry and Samrat Amin for helping me operating the MR machine.

I would also like to extend my thanks to Dr. May Boggess and Dr. Rick Gerkin for their statistical analysis advises.

I wish to thank my academic advisor Laura Hawes for her patience, motivation, and enthusiasm.

I wish to thank ASU graduate writing centers especially Jessica Kuna for helping me with my dissertation writing.

Finally, I would like to thank my great mother Lin Fu and my wife Yahan Zhang for their full support and understanding.

The research presented in this dissertation was funded by the National Institute of Health. Additional travel grants to attend professional conferences were provided by the School of Biological and Health Systems Engineering and the Graduate and Professional Student Association at Arizona State University.

TABLE OF CONTENTS

Page

CHAPTER Page

CHAPTER Page

APPENDIX

LIST OF TABLES

Table Page

Table Page

LIST OF FIGURES

Figure Page

Figure Page

Figure Page

Figure Page

Figure Page

1 INTRODUCTION

1.1 Models and Methods for Electrophysiology

The Aplysia abdominal ganglion (AAG) and salamander retina were used as sources of neuronal activity in our study. The large size of the AAG allows observation of neuronal architecture with MRI. Cells in the AAG have different spontaneous firing patterns, have been well characterized and can be detected by microelectrode array (MEA) recordings. The salamander retina generates action potentials in the ganglion cell axons. Different ganglion cells respond differently to light stimulation, which makes it a favorite object for neuro electrophysiological study.

1.1.1 Hodgkin Huxley Model of Neural Activity

To understand the action potential, the excitable cell membrane can be described by the Hodgkin-Huxley model (Alan L Hodgkin & Andrew F Huxley, 1952) as shown in Figure 1.1.

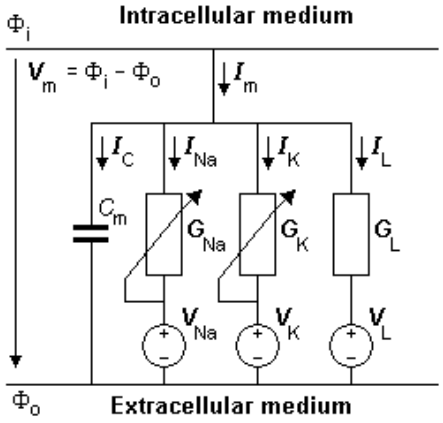

Figure 1.1 Electric circuit representation of a cell membrane. This figure is adapted from http://www.bem.fi/book/

The capacitor represents the cell membrane capacitance. The ion permeability of the membrane with respect to sodium, potassium, and other ions are denoted with the variable resistors. The voltage sources represent the Nernst voltages of the sodium, potassium, and chloride channels, respectively. Active transporters and ion channels work against each other to generate concentration gradients: Active transporters move selected ions against concentration gradients, meanwhile, ion channels allow specific ions to cross the membrane in the direction of concentration gradients. The Nernst potential is described as:

$$V_m^{eq} = \Phi_i - \Phi_e = \frac{-RT}{Z_p F} \ln\left(\frac{|C_p|_i}{|C_p|_e}\right), \quad (1.1)$$

where V_m^{eq} is the potential difference at equilibrium across the membrane, defined as the difference between intracellular (i) and extracellular (e) potentials. Z_p is the valence of the ion p, T is the absolute temperature, and F and R are Faraday's constant and the gas constant respectively. C_p denotes the concentration of the species p.

The variable resistors in Figure 1.1 indicate membrane ion channel conductance per unit area for sodium, potassium and chloride ions. Hodgkin and Huxley hypothesized that potassium channels were controlled by four n-particles. The probability of an n-particle being in the open position is described by the dimensionless parameter n. The potassium channel would be open only if four n-particles had high probabilities. Sodium channel operation was described using three m-particles and one h-particle. Similarly, m and h indicate the probability of m and h particles being in the open position. The membrane conductance of ion specific channels may be expressed as:

$$G_K = G_{K\,max} n^4, \quad (1.2)$$

$$G_{Na} = G_{Na\,max} m^3 h, \quad (1.3)$$

where G_K^{max} and G_{Na}^{max} are the maximum value of potassium and sodium conductance [mS/cm²].

Values of n, m and h are found by solving differential equations of the form:

$$\frac{dk}{dt} = \alpha_k(1 - k) - \beta_k k. \quad (1.4)$$

Where k represents n, m, and h, respectively. α_k and β_k are the transfer rate coefficients of the gating variables n, m, and h [1/s]. They describe the dependence of particles moving from closed to open state (α_k) or the opposite (β_k). The parameters α_k and β_k are voltage dependent and are expressed as:

$$\alpha_n = \frac{0.1 - 0.01V'}{e^{(1-0.1V')} - 1}, \beta_n = \frac{0.125}{e^{0.0125V'}},$$

$$\alpha_m = \frac{2.5 - 0.1V'}{e^{(2.5-0.1V')} - 1}, \beta_m = \frac{4}{e^{(V'/18)}},$$

$$\alpha_h = \frac{0.07}{e^{0.05V'}}, \beta_h = \frac{1}{e^{(3-0.1V')} + 1}, \quad (1.5)$$

where $V' = V_m - V_r$, V_r is the resting membrane voltage. V_m is the transmembrane voltage. The transmembrane current I_m is:

$$I_m = C_m \frac{dV_m}{dt} + (V_m - V_{Na})G_{Na} + (V_m - V_K)G_K + (V_m - V_L)G_L. \quad (1.6)$$

From the Hodgkin-Huxley equations, we see that the cell membrane conductivity changes along with the transmembrane voltages. This correlation indicates that it may be feasible to detect neural activity by observing conductivity contrasts instead of membrane voltages or extracellular potential changes.

1.1.2 AAG

The AAG was thoroughly studied by Frazier et al. (Frazier, Kandel, Kupfermann, Waziri, & Coggeshall, 1967). Most of the nerve cells of AAG in large animals are about 50-100 μm in size. The cells within the ganglion are diverse. A schematic diagram of the AAG from Frazier is shown in figures 1.2-1.3.

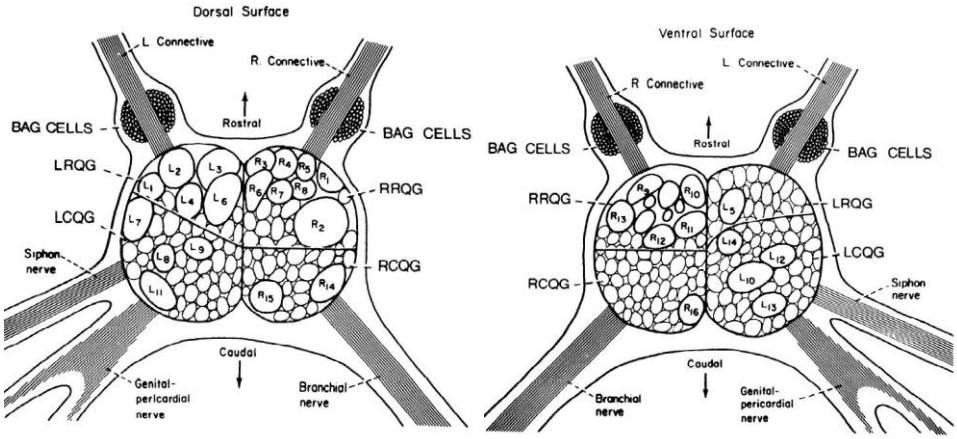

Figure 1.2 Sketch of an AAG. The dorsal surface is shown on the left and the ventral surface on the right. This figure is adapted from Frazier et al. (Frazier et al., 1967).

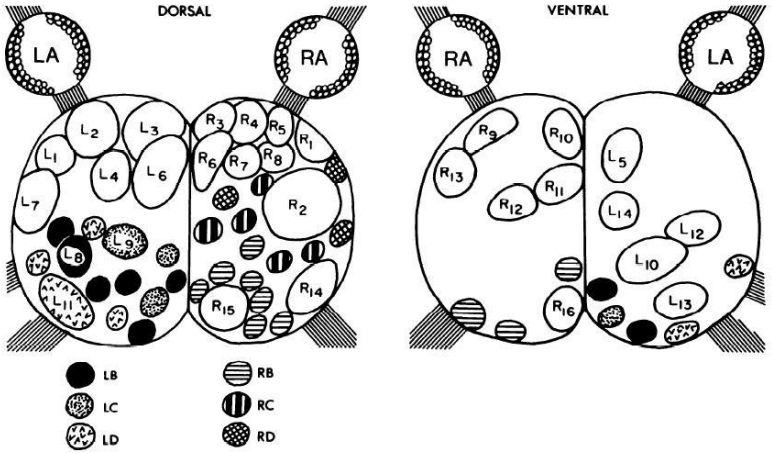

Figure 1.3 Schematic diagram of cell clusters. This figure is adapted from Frazier et al. (Frazier et al., 1967).

The ganglion can be divided into four quarters: the right rostral quarter-ganglion (RRQG), the right caudal quarter-ganglion (RCQG), the left rostral quarter-ganglion (LRQG) and the left caudal quarter-ganglion (LCQG). The AAG electrophysiology is described in the following paragraphs.

The identified cells in RRQG are the rostral white cells (R3-R13), R1 and R2. The rostral white cells have similar electrophysiological properties with a firing rate of about 0.5-1 spikes/s. The R1 produces fast spikes. The R2 is the largest cell in the ganglion and is often silent.

The identified cells of the RCQG are the caudal white cells (R14, R15), R16, cluster RB, and parts of clusters RC and RD. R14 does not usually generate spontaneous activity. R15 fires in bursts. R16 is a small cell and shares common excitatory

postsynaptic potential (EPSP) with nearby cells. The RB and RC clusters fire irregularly; LD bursts when stimulated.

The identified cells of the LRQG are L1-L6. L1 is silent and topographically symmetrical with R1. L2, L3, L4, and L6 can generate a burst of spikes and can be silent or fire continuously.

The identified cells of the LCQG are L7-L14 and clusters LB, LC, and LD. L7, L8, and L9 spontaneously fire at 1-3 spikes/s. L11 usually fires at a rate of 2-4 spikes/sec and sometimes fires high-frequency bursts. Cell L10 can be either silent or firing regularly. Cells L12 and L13 fire with the frequency of 4-6 spikes/s. L14 is silent. The properties of LB and LC clusters have properties similar to L8 and L9. The LD group shares properties with L11.

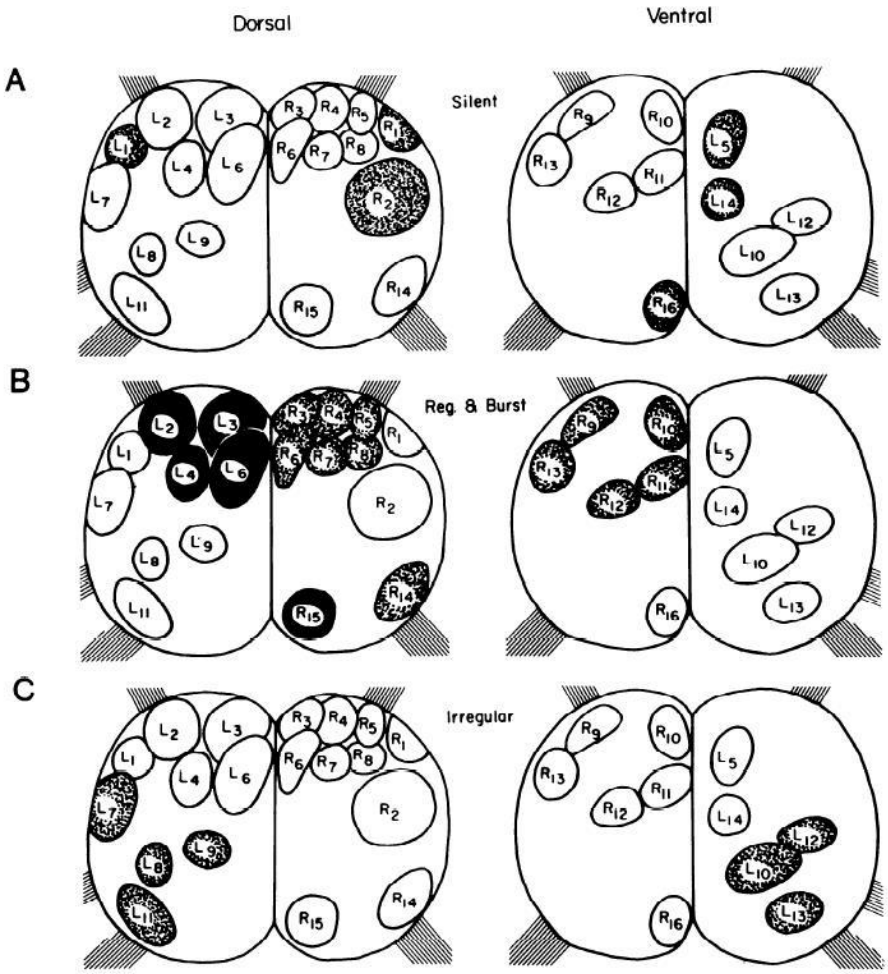

Figure 1.4 Sketch of cells distinguished by firing pattern. Silent cells are shown stippled in A; the cells that fire regularly are stippled in B; burst firing cells are blackened in B and irregularly firing cells are stippled in C. This figure is adapted from Frazier et al. (Frazier et al., 1967).

The electrophysiological properties of the AAG are divided into three categories: silent, regular & burst, and irregular. These are schematically described by Frazier et al. (Frazier et al., 1967) in figure 1.4.

In summary, 30 cells and eight cell clusters in the AAG were defined by Frazier et al. (Frazier et al., 1967). Twenty four out of thirty are spontaneously active. The rhythm of rostral white cells (L3, L13) is highly regular. L2, L3, L4, L6, and R15 have bursting rhythms.

1.1.3 Salamander Retina

The vertebrate retina has multilayer neural networks. It is composed of five types of neurons: photoreceptors, horizontal cells, bipolar cells, amacrine cells, and ganglion cells. A schematic diagram made by Meister is shown in Figure 1.5 (Meister, Pine, & Baylor, 1994):

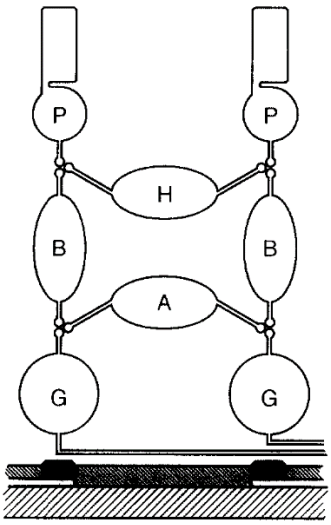

Figure 1.5 Schematic diagram of the vertebrate retina showing photoreceptors (P), horizontal cells (H), bipolar cells (B), amacrine cells (A), and ganglion cells (G). This figure is adapted from Meister et al. (Meister et al., 1994).

The retina can function in vitro for several hours, and its neural activities can be easily modulated by light. These make it a good subject for neural electrophysiology

study. The ganglion cells produce different responses to different light wavelength, light intensity, flicker frequency, field size and shape (Meister et al., 1994).

The salamander retina is also well suited for extracellular multi-electrode array recording due to its large ganglion size and monolayer cell (Segev, Puchalla, & Berry, 2006).

1.2 Neural Stimulation

Electrical stimulation has been widely applied for neurological disorder treatment and neuromodulation. Applications include but are not limited to use in extremity prostheses, cochlear and brain-stem auditory prostheses, retinal and cortical visual prostheses, as well as treating epilepsy, essential tremor, Parkinson's disease, dystonia, and depression (Cogan, 2008).

Neural stimulation methods are considered either invasive or non-invasive. Stimulation methods such as Intracortical Microstimulation (ICMS) and deep brain stimulation (DBS) are considered invasive; and Transcranial Direct Current Stimulation (tDCS), Transcranial Alternating Current Stimulation (tACS), and Transcranial magnetic stimulation (TMS) are considered non-invasive.

1.2.1 Invasive Stimulation Methods

Invasive stimulation methods require electrode implantation. There are two important concepts in ICMS: Strength-duration relationship and strength-distance relationship.

The strength-duration relationship was first introduced by Lapicque (Lapicque, 1901). It describes the relationship between pulse width and current intensity required to

activate neuronal tissue. A spherical cell model is assumed to describe this theory. The spherical cell is a poor model for most cells, but it has a geometrical uniformity that avoids the additional complexity of spatial variation. The model is shown in figure 1.6 (a). The transmembrane potential is uniformly distributed on the cell membrane and the equivalent electrical circuit can be simplified as shown in figure 1.6 (b). Here, R and C are the resistance and capacitance of the cell. If a stimulus current I_0 continues over a time t, the corresponding evoked transmembrane potential is:

$$v_m = I_0 R(1 - e^{-t/\tau}) \tag{1.7}$$

where $\tau = RC$ is the time constant. Rewriting (1) for a stimulus (S) just strong enough and long enough to reach a threshold voltage level V_T with stimulus duration (T), we have:

$$V_T = S(1 - e^{-T/\tau}) \tag{1.8}$$

Rearranging equation 1.8 and divide R on both sides, we get:

$$I_{th} = I_R/(1 - e^{-T/\tau}) \tag{1.9}$$

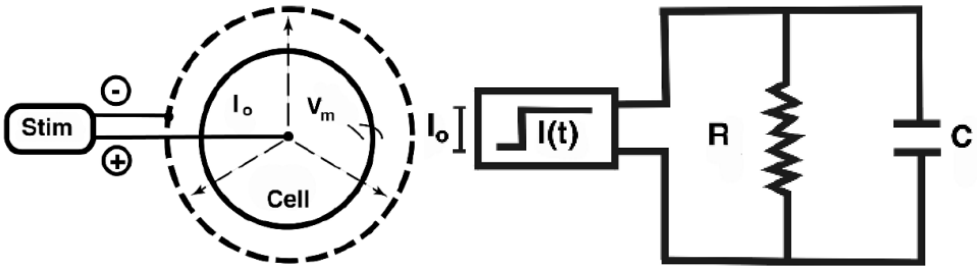

Figure 1.6 Simplified equivalent electrical circuit of a spherical cell. (a) spherical cell model and its (b) equivalent electrical circuit. This figure is adapted from Plonsey and Roger C (Plonsey & Barr, 2007).

The quantity IR is termed the rheobase, while I_{th} is the minimum current required to reach the threshold with stimulus duration T. The rheobase is the minimum stimulus intensity that can induce neuronal activity. A current lower than rheobase cannot induce action potential no matter how long it is applied. The pulse duration when the current intensity is twice rheobase is called chronaxie. The rheobase and chronaxie are illustrated in figure 1.7.

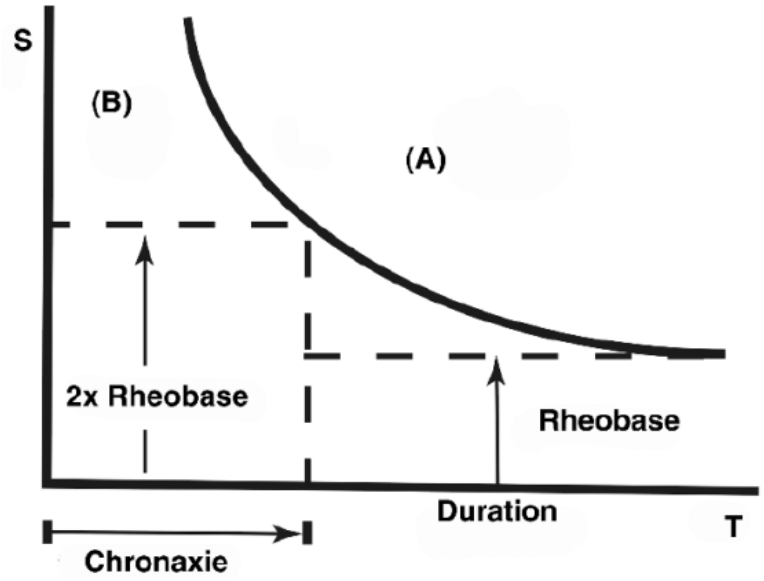

Figure 1.7 Strength-Duration Curve. The region marked (A) represents the intensity-duration combination that can induce neuronal activity, whereas area marked (B) are below the threshold level. The figure is adapted from Plonsey and Roger C (Plonsey & Barr, 2007).

Chronaxie can be used as a guide for time period that is required to reach the threshold voltage when a real stimulus is used.

The distance between the electrode and the neuron also affects the stimulus intensity needed to activate the neuron. This strength-distance relationship can be described by the following function:

$$I = kr^2 + I_{min} \quad (1.10)$$

where I_{min} is the minimum stimulus intensity that required to activate a neuron with an electrode immediately adjacent to the axon. Here, r is the distance between the electrode and the axon, k is the excitability constant. The value of k depends on cell type and it varies widely. For example, axons of spinal cord interneurons have k values of around 80 $\mu A/mm^2$ while axon in the medial forebrain bundle have k values between 1000 and 6400 $\mu A/mm^2$ (L. G. Nowak & Bullier, 1996). From the equation, we can see that the closer the neuron is located to the electrode, the more likely it will be activated. But neurons located further away may also be recruited if they have higher excitability constants.

The numerical simulation studies showed that the distance between electrode and axon can alter the strength-duration relationship (Barr & Plonsey, 1995). Under space clamp conditions, the threshold is no longer dependent on stimulus duration. Results found in the study are shown in figure 1.8. As the electrode became further away from the axon, the threshold was also independent of stimulus duration. This can be explained because as the axial variation of the applied field becomes increasingly uniform, the condition better approximates a space-clamped experiment.

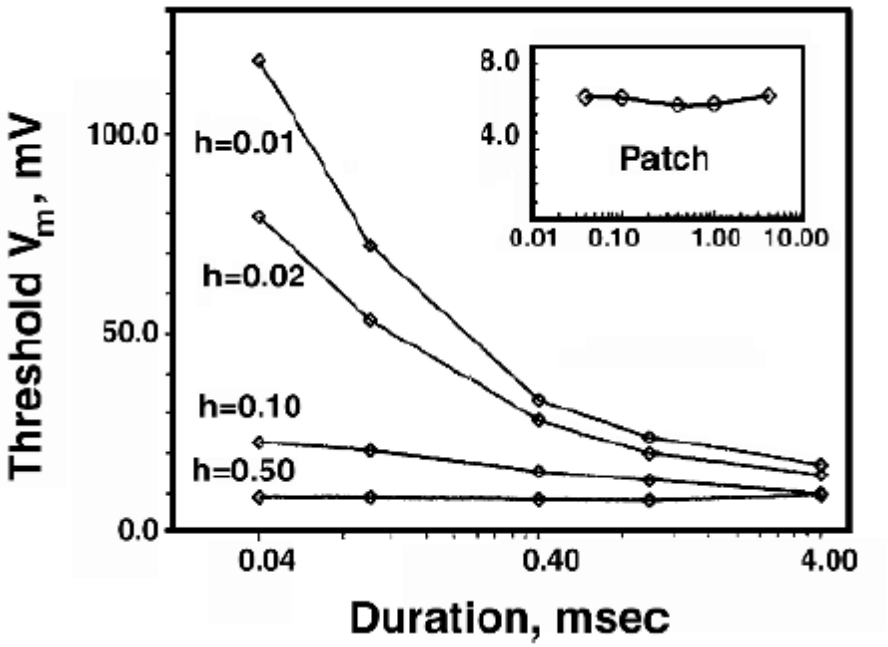

Figure 1.8 Threshold of transmembrane voltage V_m versus Stimulus Duration for a Point Stimulus. Outer: Results of field stimulation study. Each curve represents a source-fiber distance as indicated by h (in cm). Inset: For space-clamped stimulation study. No spatial variability was found in the configuration. The largest transmembrane voltage observed when using a stimulus without producing a propagating action potential is plotted. All transmembrane potentials shown are relative to a baseline of -57 mV. The figure is from Barr and Plonsey (Barr & Plonsey, 1995).

From the above study, we can see that the axon stimulation threshold is not a fixed number, it changes with stimulus duration and the distance between the electrode and the fiber. When the stimulating electrode is close, but the duration is long, the membrane may take longer time to respond, but only within the restricted membrane surface. The consequence is that the stimulus threshold in this case is greater than for a

more distant electrode with the same stimulus duration. Since a small area of the membrane has to provide the same amount of current to stimulate the remainder of the fiber, a closer stimulus has to produce a larger potential gradient to offset the depolarized membrane decay that is accelerated by longitudinal current flowing into the hyperpolarized regions. This explains the very large threshold requirements for small values of h.

The knowledge of strength-duration and strength-distance relationships is not enough for us to fully understand neural stimulation. Neurons can be directly activated by the electrode, and also can be affected by excitatory synapses and inhibitory synapses from cells that are directly activated by the electrode. To detect both directly and indirectly activated neurons is not trivial. The most direct way of detecting the activated neuron is by using recording electrodes. However, neural activity voltages may often be drowned out by effects of the injected current, which makes this method impracticable. To address this problem, behavioral tasks are used to predict neuronal recruitment. The ability of animal to perform a specific motor task can be affected by the stimulation, and this provides information about which part of cortical tissue has been affected. Neuron activation by ICMS has been reported by Histed et al. (Histed, Bonin, & Reid, 2009). Neurons being activated within a single plane near an electrode can be observed using two-photon calcium imaging. It was found that only a small fraction of the neurons in the vicinity of a stimulating electrode was activated during weak microstimulation (tens of μA). Moving the electrode tip by as little as tens of μm could vary the activated cells. Blocking synaptic transmission had little effect on the number of neurons being activated

by microstimulation. This study indicates that most of the spiking neurons nearby the electrode are directly activated.

Other research has found that stimulation primarily initiates action potentials in axon (L. Nowak & Bullier, 1998). The explanation for this phenomenon is that the sodium channel density on the axonal membranes is much higher than on the somatodendritic membranes. For vertebrate unmyelinated axons, this density is around 100-200 channels/μm^2. For nodes of Ranvier on myelinated axons, this number can be as high as 12 000 channels/μm^2. For the membranes of neocortical cell bodies and dendrites, this number is 2.5-7 channels/μm^2. A second reason is the difference in temporal properties of membrane tissue, specifically the time constant τ, which is the product of the membrane resistivity R_m and capacitance C_m. Unmyelinated axons have R_m values between 1000 and 5000 $\Omega.cm^2$. For nodes of Ranvier, this number is between 25 and 125 $\Omega.cm^2$ and would be between 20 000 and 200 000 $\Omega.cm^2$ for cell bodies. Thus, for a given intensity of stimulation, axons are depolarized much faster than cell bodies and are more likely to generate action potentials.

Intracortical microstimulation (ICMS)

Intracortical microstimulation (ICMS) is a brain stimulation method that requires stimulation electrodes placed into the parenchyma of the nervous system. During ICMS, small current injections from microelectrodes can change the electrical potential of extracellular space nearby the electrode. These fluctuations can induce transmembrane current in neurons, and may initiate an action potential if the current is suprathreshold. The stimulation waveform also affects the ICMS outcomes. If direct current is applied, a

large quantity of charge will be injected into the brain. This will lead to oxidization of water at the electrode surface (Merrill, Bikson, & Jefferys, 2005) and produce bubbles of hydrogen gas as well as free radicals. As a consequence, the electrode will be degraded, and neural tissue will be damaged by these byproducts. The problem can be solved by applying alternating pulses (Lilly, Hughes, Alvord Jr, & Galkin, 1955). With this technique, the charge will not accumulate at one electrode, and quantities of possibly neurotoxic substances can be significantly reduced. Both negative and positive currents stimulation can activate neural tissue. Cathodal stimulation depolarizes the cell membrane directly, whereas anodal stimulation causes local hyperpolarization, and can cause depolarization elsewhere on the cell membrane (BeMent & Ranck Jr, 1969). A common pulse used by many researches has a width of 0.2 ms per phase with an interval of 0 to 0.1 ms, and amplitude below 150 μA (Tehovnik, 1996). Under these conditions, the stimulation can be applied safely over several days (Agnew, Yuen, McCreery, & Bullara, 1986).

Deep Brain Stimulation (DBS)

DBS is a neurosurgical procedure involving permanent electrode implantation in the brain. The electrical impulses are sent to specific brain areas via the electrodes, to treat specific disease indications. DBS has been used clinically for treating movement disorders for about 20 years, and shows promising experimental results in treating depression and epilepsy. The full mechanism of DBS is still unclear. Electrophysiology, imaging and biochemistry method have been used to reveal some parts of the mechanism of DBS. This is well summarized by Udupa and Chen (Udupa & Chen, 2015).

The DBS target and stimulation parameters are dependent on the disease targeted. Commonly used targets for movement disorders are the Globus pallidus interna (GPi), subthalamic nucleus (STN), and thalamic ventral intermediate nucleus (Vim).

A common stimulation voltage used in DBS is between 1 and 9 V, pulse widths are between 60 and 250 ms, and frequencies between 5-180 Hz. The mechanisms of DBS may depende on the disease, the stimulation method, and the animal model used. Transcranial magnetic stimulation (TMS) studies showed that DBS can change the excitability of motor cortex, and the effect is dependent on the stimulation location and clinical condition (Hershey et al., 2003). It also showed that DBS may induce plastic changes inside the target region (Gradinaru, Mogri, Thompson, Henderson, & Deisseroth, 2009). Electrophysiological studies showed decreased neuronal firing rates in the target area with DBS in the subthalamic nucleus (STN) and globus pallidus internus (GPi) (Filali, Hutchison, Palter, Lozano, & Dostrovsky, 2004), which is consistent with the neuronal inhibition hypnosis. The explanation is that high-frequency stimulation increases potassium currents and decreases sodium currents (Beurrier, Bioulac, Audin, & Hammond, 2001; Shin et al., 2007). Another explanation is that the repeated stimulation depletes neuronal energy and causes synaptic activity failure (Lozano, Dostrovsky, Chen, & Ashby, 2002). Analysis of the firing pattern of the basal ganglia (BG) circuits indicated that reduction of entropy could be a mechanism of DBS (Brown & Eusebio, 2008). Neuroimaging studies on DBS have revealed effects on neuronal networks (Ko, Tang, & Eidelberg, 2013). It also has been found to modulate several neurotransmitter systems

like dopamine, adenosine, Gamma-aminobutyric acid (GABA), glutamate, and serotonin (Udupa & Chen, 2015).

1.2.2 Non-invasive Stimulation Method

Transcranial Direct Current Stimulation (tDCS)

Transcranial direct current stimulation (tDCS) is a non-invasive brain stimulation technique for modulating central nervous system excitability. The technique is achieved by attaching two or more electrodes on the head. The electrodes' location is critical, as the relative location of electrodes results in significant differences in where and how much current is delivered to the brain. The location of electrodes is typically specified using the International 10-20 EEG measurement system, as this method is reproducible for different head sizes (Woods, Bryant, Sacchetti, Gervits, & Hamilton, 2015) or using other reference locations on the scalp. As an example, the stimulating electrode may be placed over the motor cortex (M1) and a reference electrode placed over the contralateral supraorbital ridge (Stagg & Nitsche, 2011). An example of a full setup tDCS experiment is shown in Figure 1.9. In general, anodal stimulation causes is thought to increase neural excitability, whereas cathodal stimulation results in decreased excitability. The effect may last for some time after tDCS application has ceased ('after effect'). The induced short or long-lasting after effects depend on the applied current intensity, current density, current injection time and electrode polarity. Commonly used current intensities are 1-2 mA. A typical tDCS therapy duration is less than 20mins. The current density applied depends on electrode size, and it is usually less than 0.06 mA/cm^2 (Kuo, Paulus, & Nitsche, 2014).

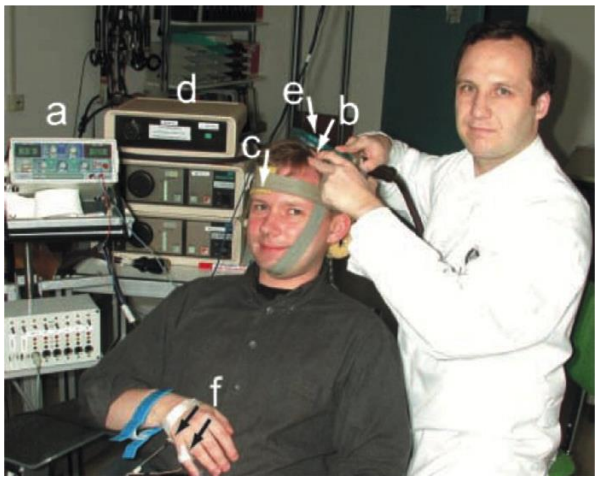

Figure 1.9 Illustration of tDCS experiment, showing (a) current source, (b) stimulation electrode, (c) reference electrode at contralateral orbit, (d) TMS stimulator, (e) TMS coil, (f) electromyography electrodes for recording Muscle evoked potentials. This figure is adapted from Nitsche et al. (M. A. Nitsche, Boggio, Fregni, & Pascual-Leone, 2009).

High-intensity (>2 mA) current can lead to increasing excitability at both current polarities. The typical relationship between polarity of current flow and excitability, can be reversed during a cognitive task, whereas a reduced excitability may be observed during a motor task following both anodal and cathodal stimulation. The state of affected neurons (e.g., tasks, practice, fatigue) prior to stimulation can also change the effects of stimulation (Filmer, Dux, & Mattingley, 2014). Neurons in deep cortical layers were often deactivated by anodal and activated by cathodal stimulation (Stagg & Nitsche, 2011). It has been hypothesized that tDCS modulates neural activity by affecting the resting membrane potential (M. Nitsche et al., 2003; M. A. Nitsche, Kuo, et al., 2009; M. A. Nitsche et al., 2004; M. A. Nitsche et al., 2005), but the mechanism of this neuronal excitability modulation is not yet fully understood.

Transcranial Alternating Current Stimulation (tACS)

Transcranial alternating current stimulation (tACS) externally applies alternating electrical currents to stimulate the brain and can also influence cortical activity (Antal et al., 2008). The effects of tACS are affected by 3 factors: frequency, amplitude, and phase. It has been shown that tACS within the EEG frequency range (0.1-80 Hz) can synchronize neuronal networks and induce oscillatory brain activity changes. Studies using tACS showed an intensity-dependent effect at 140 Hz: an 0.4 mA intensity was found to inhibit the neural activity, while 0.2, 0.6 and 0.8 mA intensities had no significant effect (Moliadze, Atalay, Antal, & Paulus, 2012). Polania et al.'s study showed that cognitive performance increased when stimulating the left frontal and parietal cortex by 6 Hz in phase, and decreased when out of phase (Polanía, Nitsche, Korman, Batsikadze, & Paulus, 2012). However, as with tDCS, the mechanisms underlying these effects have not yet been clarified.

A form of tACS has also been found useful in treatment of brain cancer: a 200 kHz frequency has been used for treating recurrent glioblastoma and showed promising result without side effect (Kirson et al., 2007).

Transcranial Magnetic Stimulation (TMS)

Transcranial magnetic stimulation (TMS) is another non-invasive brain stimulation method. During TMS stimulation, a short pulse of electric current is passed through a magnetic coil, which in turn induces a brief, high-intensity magnetic field. This induced magnetic field is perpendicular to the coil plane, and has a maximum intensity of 2 Tesla, and lasts about 100 μs. This induced magnetic field can induce a perpendicular

electric field inside the brain and can either excite or inhibit a small cortical region beneath the coil. TMS is often used to locate the motor cortex by positioning the coil such that a motor-evoked potential (MEP) is produced, and a muscle twitch results. The neuronal elements parallels to the induced electric field are mostly activated by the field geometry. The most common magnetic coil shapes are figure-eight and round. Figure-eight coils produce a focal field shape about the coil intersection point, and round coils produce larger fields. TMS pulses may be single, or high-frequency (1-50 Hz) repetitive (rTMS). Single pulse TMS is considered very safe. However, rTMS has the potential to cause seizure (Hallett, 2007). Because of the risk of seizure, a set of safety guide lines for TMS was produced by Wassermann (Wassermann, 1998). Both TMS and rTMS have been used for mapping the motor cortex (Wassermann, McShane, Hallett, & Cohen, 1992), studying the function of the motor system (Chen et al., 1997), helping localize memory processes (Mulleners, Chronicle, Palmer, Koehler, & Vredeveld, 2001), understanding brain physiology (Ziemann, Rothwell, & Ridding, 1996), and inducing neural plasticity (Chen et al., 1997; Pascual-Leone, Valls-Solé, Wassermann, & Hallett, 1994). At 0.9 Hz, TMS was found to depress motor cortex excitability (Chen et al., 1997). TMS also has potential therapeutic applications such as in treating Parkinson's disease, dystonia, and stroke. This maybe because TMS stimulation has been found to change synaptic strength (Hallett, 2007).

1.3 Magnetic Resonance Imaging (MRI)

MRI is a modern medical imaging technique that requires strong magnetic fields and radio frequency spectrometry. Its non-invasive and non-ionizing nature distinguishes

it from other medical imaging techniques such as X-Ray, CT, and PET. An MRI scanner is composed of a superconducting electromagnet that generates a strong static magnetic field, multiple radio frequency coils that are used to generate and receive RF energy from the subject being imaged, and gradient coils that are used to create spatial magnetic field variation in all three spatial directions.

1.3.1 Physical Principles

MRI has a variety of applications, but they all share the same physical principles: The nuclear spin status of atoms can be changed by radio frequency (RF) pulses. Protons are the most utilized nucleus in medical imaging. They can be viewed as spinning positive charged spheres. The proton spins are randomly oriented in the absence of an external magnetic field. No signal can be received because the net magnetization is zero in this condition. Once an external magnetic field is applied, each proton will re-orient and spin around the axis which is aligned with the magnetic field. Thus, a net longitudinal magnetization (M) aligned with the main magnetic field is created. This phenomenon is called precession. The spin precession frequency is called the Larmor frequency (ω_0) and its relationship with the magnitude of the main magnetic field (B_0) and the gyromagnetic ratio (γ) is expressed by equation 1.7.

$$\omega_0 = \gamma B_0. \tag{1.7}$$

In order to measure signals, RF pulses at the Larmor frequency are used to tip the magnetization away from the longitudinal plane (M_z) to the transverse plane (M_{xy}) and force the nuclei in phase. Once the RF pulse is removed, the system starts to return to equilibrium. Nuclei start to diphase and the transverse magnetization starts to disappear.

This phenomenon is known as transversal relaxation. Meanwhile, the longitudinal magnetization returns to its original size, which is called longitudinal relaxation. During these processes the protons emit RF energy that can be detected by receiver coils. The spin-lattice relaxation time (T1) is a time constant used to describe how (M_z) returns to equilibrium status. This process is described by equation 1.8.

$$M_z = M_0(1 - e^{-t/T1}), \quad (1.8)$$

where M_0 is the equilibrium magnetization.

The spin-spin relaxation time, T2, is used to describe transversal relaxation. This process is described by equation 1.9.

$$M_{xy} = M_{xy0}e^{-t/T2}, \quad (1.9)$$

where M_{xy0} is the initial transverse magnetization. Evolution of T1 recovery and T2 decay are described in figure 1.10.

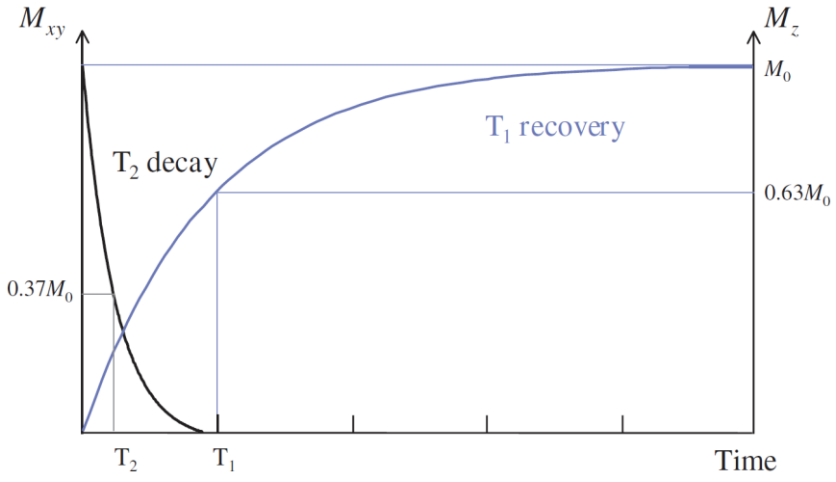

Figure 1.10 Plots of T1 recovery and T2 decay. This graph was adapted from McRobbie et al. (McRobbie, Moore, Graves, & Prince, 2017).

The time T2* is similar to T2, but it considers the effect on transverse relaxation of local magnetic field inhomogeneity. Different tissues have different T1 and T2 values, thus, depending on pulse sequence timing, they can be differentiated in the MR images. The electromagnetic signal that is generated immediately after an 90° RF pulse is called the Free induction decay (FID). It is described by equation 1.10 (Liang & Lauterbur, 2000).

$$S(t) = M_z^0 e^{-t/T_2} e^{-i\omega_0 t}$$

Or

$$S(t) = M_z^0 e^{-t/T_2} e^{-i2\pi(\gamma B t)}. \quad (1.10)$$

Differences in T1, T2, and proton density (i.e., the number of the hydrogen atoms per unit volume) can cause tissue contrast in images. The repetition time (TR) and the echo time (TE) are two key factors in determine the image contrast. TR is the time between two RF excitation pulses. TE is the time between the RF pulse and the received echo signal. Typically, short TR and TE produce T1-weighted images, long TR and TEs produce T2-weighted images, and long TR and short TEs produce proton-density-weighted images. This effect is described in figure 1.11.

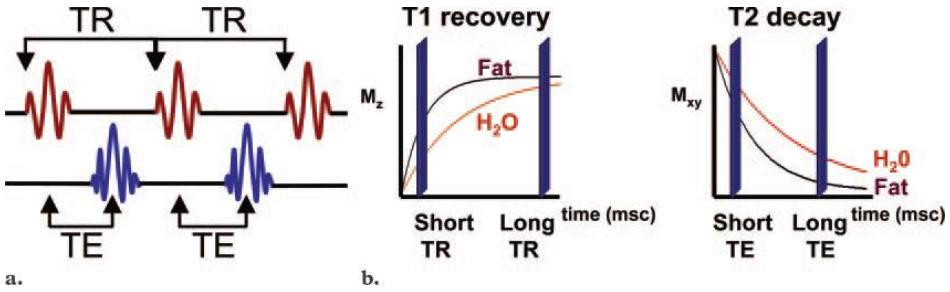

Figure 1.11 Schematic diagram of TE, TR, T1 recovery and T2 decay. In a., a schematic description of TR and TE is shown. b. shows graphs of the difference between short and long TRs and TEs. On the left, a short TR brings higher contrast between water and fat in T1 recovery, while on the right, a long TE brings higher contrast between water and fat in T2 decay. The figure was adapted from Bitar et al. (Bitar et al., 2006).

In T1-weighted images, tissues with short T1s (like fat) display as high signal and tissues with long T1s (like water tissue) have low signal. In T2-weighted images, tissues with long T2 values have high signal and tissues with short T2s have low signal. Examples are shown in figure 1.12. In proton density weighted images, tissue with higher proton densities appear brighter.

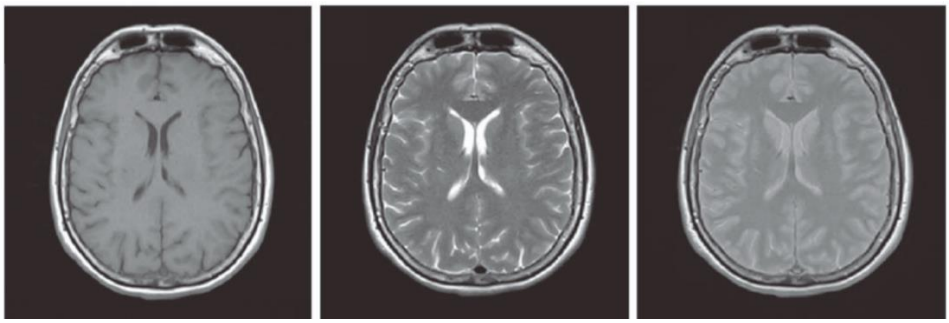

(a) (b) (c)

Figure 1.12 Examples of T1, T2 and proton density weighted images. Part (a) shows a T1-weighted image, (b) T2-weighted image, (c) Proton-density-weighted image. The figure was adapted from Plewes and Kucharczyk (Plewes & Kucharczyk, 2012).

To image nuclei in different regions, each region should have a unique precession frequency. This is achieved by adding a gradient magnetic field along the three orthogonal axes x, y, and z. Usually, magnetic field variation along the z-axis (B_0 direction) is used for slice selection, the x- and y-axes are used for frequency and phase encoding respectively. A slice selection gradient is always applied first as a linear gradient magnetic field along B_0. After that, the applied RF pulse frequency is changed to match the Larmor frequency of the selected slice. The slice thickness selected depends on the RF pulse bandwidth. The spatial frequency difference caused by gradient coils on one slice can be described by function 1.11 and 1.12.

$$k_x = \gamma G_x t \tag{1.11}$$

$$k_y = \gamma G_y t_{PE} \tag{1.12}$$

where G_x and G_y are the gradient magnetic field strength, t_{PE} is the phase encoding time and t is the frequency encoding time. The encoded MR signals are acquired in k-space.

The k-space is described pictorially by Plewes and Kucharczyk (Plewes & Kucharczyk, 2012) as shown in figure 1.13.

Considering the gradient magnetic field, the signal generated by a collection of hydrogen atoms becomes equation 1.13.

$$S(t) = M_z^0 e^{-t/T_2} e^{-i2\pi(\gamma(B_0+Gx)t)}, \quad (1.13)$$

where G is the gradient magnetic field strength and x is the location of the atoms. The k-space data is described by equation 1.14 (Mezrich, 1995). We can see that one point in k-space contains the information on the whole slice, as.

$$S(k_x, k_y) = \int_{-\infty}^{\infty}\int_{-\infty}^{\infty} M_z^0 e^{-i2\pi(k_x x+k_y y)} dxdy. \quad (1.14)$$

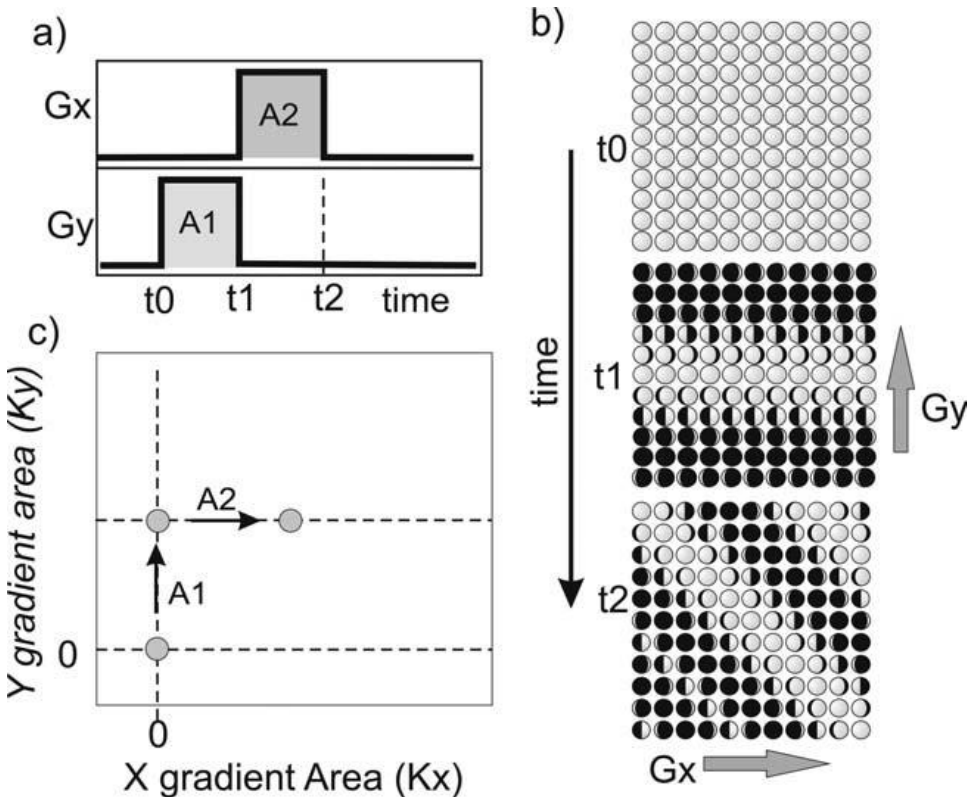

Figure 1.13 Schematic diagram for k-space filling. Gradient magnetic field is shown in (a), y-gradient turns on between t0 and t1, x-gradient turns on between t1 and t2. Nuclei in one slice are shown in (b), all nuclei are in phase at t0, then start to dephase along the y-axis when y-gradient turns on, and finally dephase along the x-axis when x-gradient turns on. The k-space is shown in (c), when y-gradient turns on, the data changes from (0, 0) to (0, A1) along the K_y-axis, then changes to (A2, A1) along the K_x-axis. The figure is adapted from Plewes and Kucharczyk (Plewes & Kucharczyk, 2012).

1.3.2 Pulse Sequence

A pulse sequence diagram is used to show times at which gradients and RF excitation pulses are applied in MR image acquisition. Even though many pulse

sequences are available for both clinical or research purposes, there are only two fundamental types of pulse sequence: spin echo (SE) and gradient echo (GRE) (Bitar et al., 2006).

A spin echo sequence starts with a 90^o excitation RF pulse, which is accompanied by the slice selection gradient pulse. A phase encoding gradient is applied and is followed by an 180^o RF pulse and slice selection gradient pulse.

The frequency encoding gradient between the 90^o and 180^o pulse is to dephase the spins so that they will rephase at the middle during the echo collection. Finally, the frequency encoding gradient is applied, and the echoes are collected. This is shown in figure 1.14(a).

A gradient echo sequence starts with an RF excitation pulse and slice selection gradient pulse, then phase encoding as for the spin echo case. At the same time, a dephasing frequency encoding gradient is applied to ensure that the maximum echo will be received at the middle of the echo collection. Finally, the frequency encoding gradient is applied, and echo is collected just like in spin echo. This is shown in figure 1.14(b).

To accelerate the image acquisition time, fast imaging techniques have been developed. In the fast SE sequence, a 90^o RF pulse is followed by multiple 180^o RF pulses. Phase encoding gradients are applied between each pair of 180^o pulses. In this way, multiple k-space lines are acquired in one TR and the scanning time can be significantly decreased. This is shown in figure 1.15.

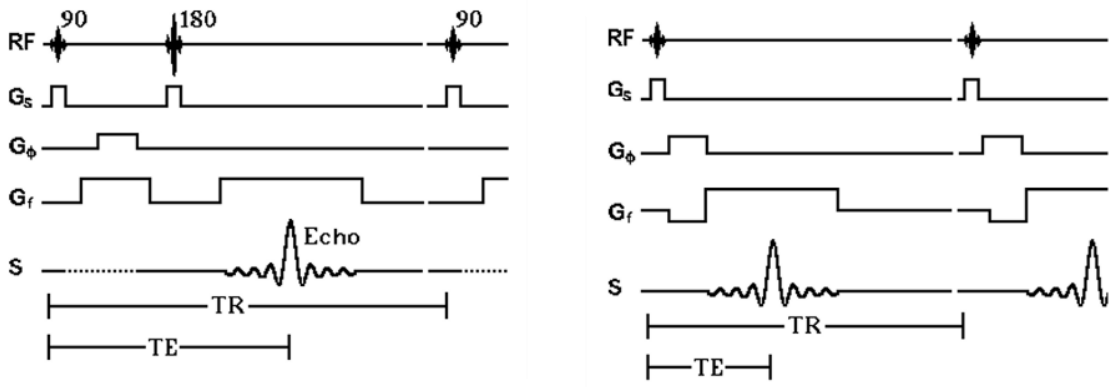

(a) (b)

Figure 1.14 Spin echo and gradient echo pulse sequences. (a) Spin echo sequence and (b) gradient echo sequence. Each sequence is composed of five waveforms, they are RF pulse, slice selection gradient, phase encoding gradient, frequency encoding gradient, and echo collection. The figures are adapted from Hornak (Hornak, 2008).

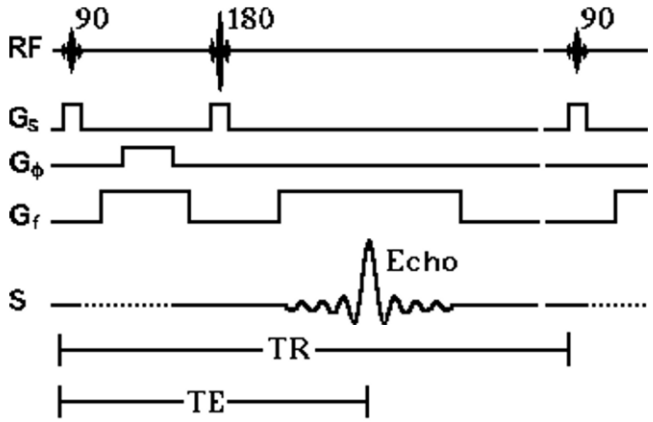

Figure 1.15 Fast spin echo pulse sequence. The sequence is composed of five waveforms, they are RF pulse, slice selection gradient, phase encoding gradient, frequency encoding gradient, and echo collection. The figure is adapted from Hornak (Hornak, 2008).

To accelerate the image acquisition speeds in GRE, partial flip angle are used instead of 90^{o} pilses. The M_z can recover faster in this way without much signal loss, and TR can be decreased.

Echo-planar Imaging (EPI) is a rapid MR imaging technique which has the potential to obtain the whole image in one TR. This is done by alternately switching on and off the phase and frequency encoding gradient repetitively during one TR and covering all k-space lines in this period. An EPI pulse sequence is shown in figure 1.16.

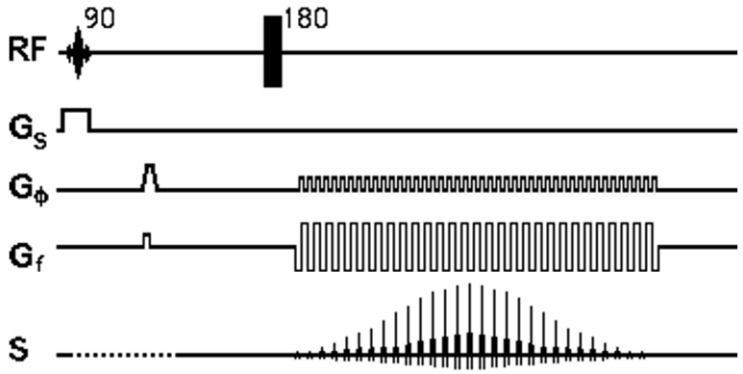

Figure 1.16 Echo-planar Imaging pulse sequence. The sequence is composed of five waveforms, they are RF pulse, slice selection gradient, phase encoding gradient, frequency encoding gradient, and echo collection. The figure is adapted from Hornak (Hornak, 2008).

1.3.3 Signal and Imaging Processing

Equation 1.14 has a similar form to the equation that defines the Fourier transform (equation 1.15).

$$F(\omega) = \int f(t)e^{-j2\pi\omega t}dt. \quad (1.15)$$

Thus, the image can be obtained by performing a 2-D inverse Fourier transform on the k-space data. The signals are received by using quadrature detection, thus each data point in k-space, and in the transformed laboratory frame, contains a real part and an imaginary part. The corresponding magnitude and phase images are obtained by using equation 1.16 and 1.17 respectively.

$$\sqrt{\text{Real}^2 + \text{Imag}^2}, \tag{1.16}$$

$$\tan^{-1}(\text{Imag}/\text{Real}). \tag{1.17}$$

Magnitude images are mostly used in clinical studies to delineate different soft-tissue structures, phase images can be useful for studying flow inside the tissue.

1.3.4 Ultrahigh Field (UHF) MRI

Currently, 1.5 and 3 Tesla are the magnetic field strengths (B_0) most commonly used in clinical MRI systems. For preclinical studies, 7 and 9.4 Tesla are standard magnetic field since animal imaging often requires higher resolution. High field MRI systems have both advantages and disadvantages compared to conventional MRI systems. In general, images generated using high field systems provide higher signal to noise ratios (SNR), are more sensitive to susceptibility artifact, decrease T1 contrast and increase T2 contrast, and emphasize chemical shift (Nakada, 2007). These characteristics makes high field MRI a good candidate for MR spectroscopy (MRS), functional MRI (fMRI), and Quantitative Susceptibility Mapping (QSM) applications. Partial advantages and disadvantages have been summarized in table 1.1 by Ladd et al. (Ladd et al., 2018). The relationship between SNR and B_0 is generally expressed with the function shown in equation 1.18:

$$SNR \propto B_0^{7/4}. \quad (1.18)$$

From equation 1.18, we can see that increased B_0 can increase SNR. Higher SNR is the most attractive reason for pursuing a higher magnetic field and it benefits most MR applications. Higher SNR can be used to generate higher spatial resolution images, can increase acquisition speed in the dynamic imaging, and even help identify new MR applications in either research or clinical diagnostics.

The RF specific absorption rate (SAR) safety limits are the same for all field strengths, but there are several additional issues to be considered in high field systems. The RF wavelength is shorter at high fields, thus, RF heating on foci may happen. Limitation of SAR must be reconsidered in this situation (Fiedler, Ladd, & Bitz, 2018). This can be controlled by extending the repetition time, reducing the number of slices, and lowering flip angles.

Physiological responses to the high static magnetic fields is always a concern. It has been reported that static magnetic fields can cause dizziness, nausea, magnetophosphenes, and metallic tastes (Heilmaier et al., 2011), but these effects are always transient. A recently identified effect is that high fields distorts the electrocardiogram. The reason for this is that the electrically-conducting blood is being pumped through the aortic arch at high speed. This could limit the utility of sequences that rely on cardiac triggering (Keltner, Roos, Brakeman, & Budinger, 1990; Krug, Rose, Clifford, & Oster, 2013). However, to date, there have been no long-term side-effects identified due to exposure to high field MRI (Ladd et al., 2018).

Table 1.1

Potential advantages and disadvantages for high field MRI. The table is adapted from Ladd et al. (Ladd et al., 2018).

Characteristic	Trend as $B_0 \uparrow$	Pro	Con
SNR	↑	Higher resolution, shorter scan time	None
SAR	↑	None	Fewer slices, smaller flip angle, longer TR
Physiological side-effects	↑	None	Dizziness, nausea, metallic taste
Relaxation times	T1↑	TOF, ASL, cardiac tagging	Longer scan time
	T2↓		DWI, DTI
	$T2^*\downarrow$	SWI, BOLD	
RF field uniformity	↓	Parallel reception, Parallel transmission	Position dependent flip angle, poor inversion, unexpected contrast
Susceptibility effects	↑	BOLD, SWI, $T2^*$	Geometric distortions, intravoxel dephasing
Chemical shift	↑	Fat saturation, CEST, MR spectroscopy	Fat/water and metabolite misregistration

Abbreviations:

SNR: signal to noise ratio, SAR: specific absorption rate, TOF: time of flight, ASL: arterial spin labeling, DWI: diffusion weighted imaging, DTI: diffusion tensor imaging, SWI: susceptibility weighted imaging, BOLD: blood oxygen level dependent, CEST: chemical exchange saturation transfer

Phase changes due to susceptibility changes are described by equation 1.19.

$$\Delta\emptyset = -\gamma\chi B_0 TE. \quad (1.19)$$

We can see that the phase change is directly proportional to B_0 and TE. Larger phase effects observed at UHF can benefit imaging. Spins dephase faster (Peters et al., 2007) and lead to a better contrast among tissues with different susceptibilities in susceptibility weighted imaging (SWI). MR phase and quantitative susceptibility mapping (QSM) also benefiting from the high spatial resolution and high contrast provided by UHF MRI.

Improving fMRI performance was one of the important reasons for developing UHF MRI (Uğurbil, 2014), as it increases both the spatial accuracy of fMRI signals and BOLD sensitivity. However, since fMRI images are acquired with Echo-planar imaging (EPI), increased B_0 inhomogeneity reduces the quality of EPI images (Uğurbil, 2014).

1.4 Functional Brain Imaging Techniques

Functional brain imaging techniques are important for studying neurology and understanding brain function. They are either disruption-based or activation-based, as classified in figure 1.17. Mapping with disruption-based methods is done by evaluating changes in images due to induced changes in brain function and allows correlation of affected areas with observed image changes. Activation-based techniques map the brain by correlating observed images change with task execution (Pouratian, Sheth, Bookheimer, Martin, & Toga, 2003). The methods may be either metabolically- or electrophysiologically-based. Metabolically-based methods, like fMRI and PET, typically have high spatial resolution, while electrophysiologically-based methods, such as EEG and MEG, have high temporal resolution. Activation-based methods will be considered in the following sections.

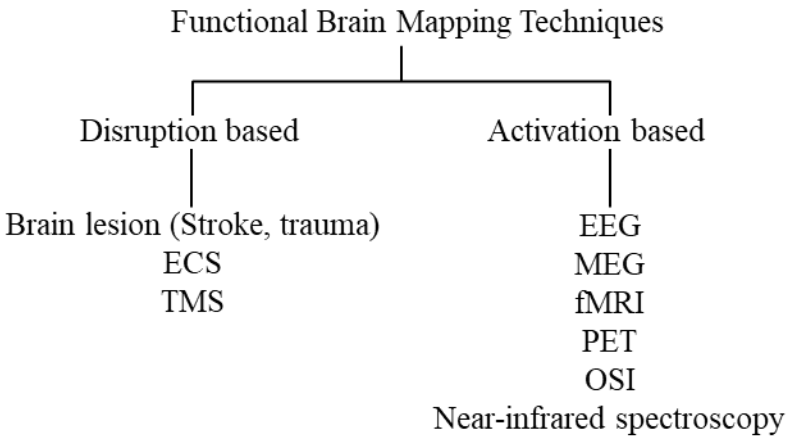

Figure 1.17 Classification of brain mapping techniques. ECS = electrocortical stimulation, TMS = transcranial magnetic stimulation, EEG = electroencephalography, MEG = magnetoencephalography, fMRI = functional magnetic resonance imaging, PET = positron emission tomography, and OSI = optical imaging of intrinsic signals. The figure is adapted from Pouratian et al. (Pouratian et al., 2003).

1.4.1 Electroencephalogram (EEG) and Magnetoencephalography (MEG)

Electroencephalography (EEG) measures the spontaneous activity of neurons on the basis of electrodes placed on the scalp. Neuronal activation in the brain induces bioelectrical currents that produce electric fields. EEG measures the voltages resulting on the surface of the head. EEG directly measures all electrical signals from the brain, but only significantly in the areas close to the skull because deep brain electrical current effects are greatly attenuated. EEG has excellent temporal resolution and it is sensitive to both tangential and radial components of a current source in a spherical volume conductor. The limitations of EEG are its poor spatial resolution and it is hard to identify the sources from the scalp fields (Quigg & Quigg, 2006).

Magnetoencephalography (MEG) records the magnetic field induced by brain electrical activity, rather than electrical signals directly. Thus, unlike EEG, MEG detects independent sources of current flow, without reference to other currents. MEG signals arise from intracellular postsynaptic currents that flow from dendrites to the soma. Magnetic fields generated by the neuronal currents induce an electric current within a detection coil. The coil is coupled to a superconducting quantum interference device (SQUID), which produces a proportional voltage output. Magnetic fields are less distorted than electric fields by the skull and scalp, thus in some cases it has better spatial resolution than EEG. MEG is more sensitive to superficial cortical activity, which makes it useful for the study of neocortical epilepsy. However, MEG is sensitive to tangential components of dipolar sources but not to the radial components, and it is also hard to locate the source of brain activity (Burgess, 2014).

1.4.2 Functional Magnetic Resonance Imaging (fMRI)

The most widely used technique for brain functional imaging is functional Magnetic Resonance Image (fMRI) (Ogawa, Lee, Kay, & Tank, 1990). Blood-oxygenation-level-dependent (BOLD) contrast is the key factor underlying fMRI contrast. During brain activity, blood flow increases in active brain regions and decreases deoxyhemoglobin concentrations in these areas. Deoxyhemoglobin is paramagnetic, which can rapidly distort the local magnetic field and dephase the transverse magnetization. Thus, deoxyhemoglobin decreases can lead to the increase of signal intensity around active areas. The spatial resolution of fMRI is high. However, fMRI signals are highly influenced by the vasculature in each voxel and can be affected by

capillary orientation and vessel size. Functional MRI analysis may therefore produce misleading results when voxels are nearby large vessels (Faro & Mohamed, 2006). Another problem in fMRI is that hemodynamic responses are slower than the neuronal activity. The signal increases typically start approximately two seconds after the beginning of the neuronal activity and reach a maximum at four to eight seconds. Therefore, temporal resolution is limited in fMRI. Furthermore, the correlation between neural activity and the hemodynamic response is not fully understood (Chu et al., 2004). Thus, fMRI can only be considered an indirect method of functional brain imaging.

1.4.3 Neural Current Magnetic Resonance Imaging (ncMRI)

Neuronal current magnetic resonance imaging (ncMRI) has been studied over several years (Jiang et al., 2014). The goal of ncMRI is to directly detect neuronal activity. Neuronal activity produces a flow of ionic current across cell membranes. This ionic current produces a magnetic flux density that interferes with the main magnetic field (B_0), and thus can alter the phase of surrounding water protons. Theoretically, this current-induced magnetic field change can be detected in both magnitude and phase MR images. However, the amplitude of these neuronal current signals is an order of magnitude smaller than the BOLD signals and physiological noise (Bandettini, Petridou, & Bodurka, 2005). Works on ncMRI include simulation (Cassarà, Hagberg, Bianciardi, Migliore, & Maraviglia, 2008; Konn, Gowland, & Bowtell, 2003; Luo, Jiang, Chen, Zhu, & Gao, 2011; Xue, Gao, & Xiong, 2006), phantom experiments (Jerzy Bodurka & Bandettini, 2002; J Bodurka et al., 1999; Konn et al., 2003), and studies in tissue including isolated ganglia (T. S. Park, Lee, Park, Cho, & Lee, 2006), optic nerves (Chow,

Cook, Whitby, & Paley, 2006) and human brains (Truong, Avram, & Song, 2008). Some positive results have been reported (Bianciardi, Di Russo, Aprile, Maraviglia, & Hagberg, 2004; Chow, Cook, Whitby, & Paley, 2007; Kamei, Iramina, Yoshikawa, & Ueno, 1999; Konn, Leach, Gowland, & Bowtell, 2004; Xiong, Fox, & Gao, 2003). For instance, Xiong et al. (Xiong et al., 2003) claimed that they could detect neuronal activity in the human brain with ncMRI. However, this result was questioned by others as the signal could have been due to fatigue or attention, which could contaminate the nc signal (Chu et al., 2004). Overall, ncMRI development has been hampered due to the extremely small signal amplitude, as well as the presence of confounding signals from hemodynamic changes and other physiological noise (Truong et al., 2008).

1.4.4 Other Techniques

Electrical Impedance Tomography (EIT)

Electrical impedance tomography (EIT) is an imaging technique which utilizes non-invasive surface electrodes to produce tomographic images of electrical property changes. The surface electrodes measure multiple transfer impedances between each pair and these data are used to reconstruct the image. Usually, one measurement is made by injecting current through a pair of electrodes and measuring the voltages resulting at other electrodes. The injected current frequency usually is between 1 Hz-1 MHz. Hundreds of similar measurements are combined with finite element model-based (FEM) inverse mathematical methods and used to reconstruct the internal electrical impedance tomographic images (Bayford, 2006). Regularization is required to avoid image artifacts caused by errors in measured voltages because the EIT inverse problem is ill-posed.

Impedances of ion channels change during action potential and depolarization, and EIT approaches may have the ability to image these changes. Low-frequency current mostly travels through the extracellular space, but may be more likely to pass through active cells as ion channels are open. High-frequency currents may more easily penetrate the cell membrane compared to low-frequency currents. Thus, impedance changes observed are also depend on current frequency. For direct current (DC), the impedance of neuronal cells changes about 1% during activity, and at 10 kHz, the changes are reduced to about 0.01%. However, it is possible to image this activity if electrodes are close enough to neuronal tissue and a frequency near 1 kHz is used. The first accurate reconstructed images of fast neural activity were reported by Aristovich et al. (Aristovich et al., 2016).

Near-infrared (NIR) Spectroscopy (NIRS)

NIRS has several alternative names, such as diffuse optical tomography (DOT) and near-infrared imaging (NIRI). The physical principles of NIRS are that NIR light (700-1000 nm) penetrates tissues, such as skin, skull, subcutaneous fat, and brain, and chromophores inside these tissues absorb and scatter the light. A schematic representation of NIRS imaging is shown in figure 1.18. The causes of attenuation of NIR light are categorized into three groups: (a) Oxygen-dependent absorption from Hemoglobin (Hb), myoglobin (Mb), and cytochrome oxidase; (b) absorption from chromophores of fixed concentration and (c) light scattering (Ferrari, Mottola, & Quaresima, 2004).

Hb has two forms: oxygenated (oxyhemoglobin, HbO_2) and deoxygenated (deoxyhemoglobin, HbR). HbO_2 absorption is higher for wavelengths (λ) > 800 nm, and HbR absorption is higher for λ < 800 nm. When the brain is active, demand for oxygen

and glucose increases. As the regional cerebral blood supply increases, the HbO_2 concentration increases and HbR concentration decreases. These changes can be reflected as increased light attenuation and scattering in fNIRS. Changes in light attenuation at a given wavelength is related to concentration changes in HbO_2 and HbR (Pinti et al., 2018).

Information provided by these absorptions can be related to brain function. NIRS provides better spatial resolution compared to EEG and MEG, and better temporal resolution compared to fMRI as described in figure 1.19.

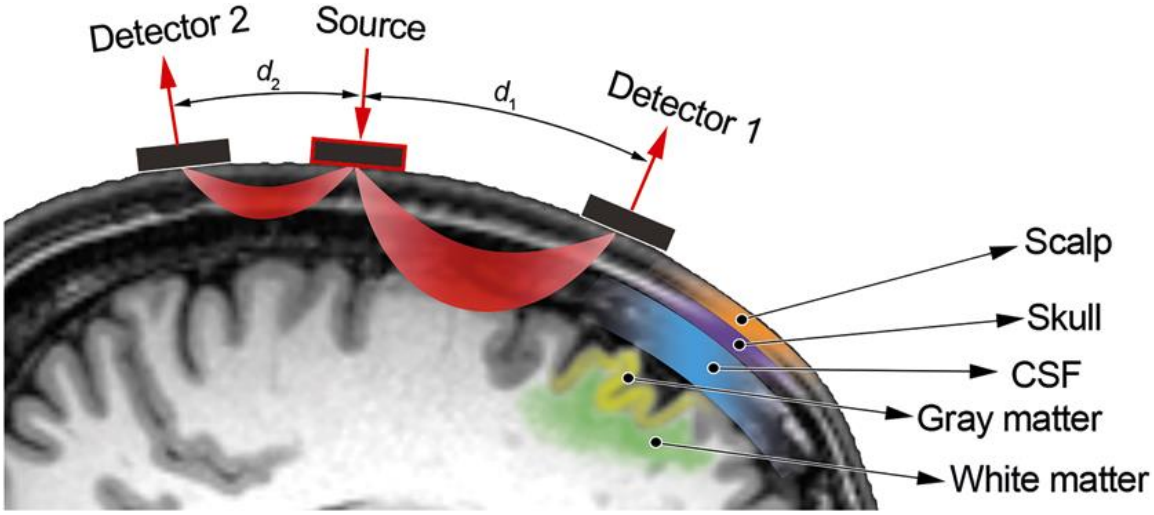

Figure 1.18 Schematic representation of NIR light traveling through the head. The figure is from Pinti et al. (Pinti et al., 2018).

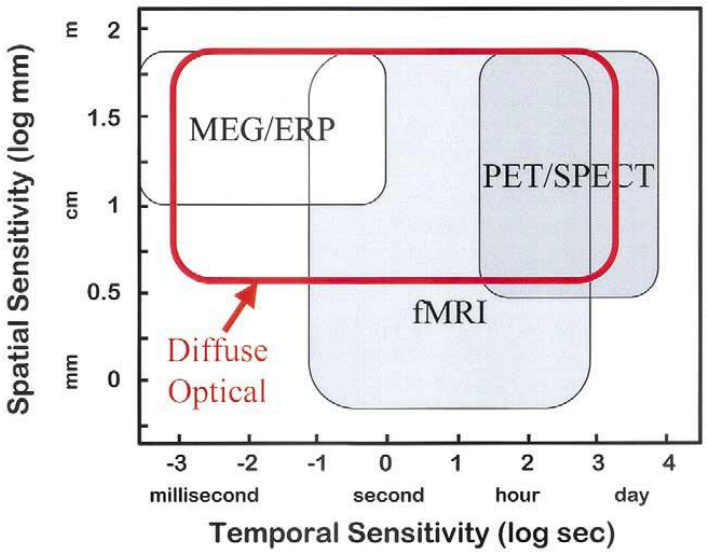

Figure 1.19 Comparison of the temporal and spatial sensitivities of different non-invasive neuroimaging methods. This figure is from Strangman et al. (Strangman, Boas, & Sutton, 2002).

Beside hemoglobin-based measurements, cytochrome oxidase also can be measured and can provide more direct neuroactivity information (Heekeren et al., 1999). Thus, NIRS has the potential to use indirect and direct methods simultaneously to monitor neuronal activity.

Three main categories of diffuse optical measurements have been developed: time domain, frequency domain, and continuous-wave (CW) measurements. A time domain measurement detects the photons' time distribution as they interact with tissue. Picosecond-pulse light is applied and fast time resolved detector is used to receive the re-emerging photons. This information reflects tissue absorption and scattering. In frequency domain measurements, the light remains turned on and the amplitude is

modulated at 10 to 100 of MHz. The amplitude decay and phase shift between the detected signal and the incident signal is used to obtain the tissue absorption and scattering information. The continuous-wave (CW) system is similar to frequency domain systems, but the incident light amplitude remains constant. The CW system only measures the amplitude decay (Strangman et al., 2002). These measurements can either be used for point measurement or an imaging configuration, depending on the number of sources and detectors used. Point measurement usually needs one source and one or more detectors. Meanwhile, imaging configurations require two or more sources and detectors (Strangman et al., 2002).

Deeper light penetration depth can be obtained by extending the source-detector distance. However, the signal to noise ratio (SNR) decreases as the source-detector distance increases. Typical source-detector distances are between 30-35 mm for adults and 20-25 mm for infants (Pinti et al., 2018).

NIRS is portable, movement tolerable, and safe to use, thus it is suitable for investigating brain function in infants and children (Pinti et al., 2018), muscle physiology (Perrey & Ferrari, 2017) and cerebral cortex pathophysiology (Yücel, Selb, Huppert, Franceschini, & Boas, 2017).

The main limitations of NIRS measurements are its lower spatial resolution than fMRI, lower temporal resolution than EEG/MEG, shorter penetration depth (1.5-2 cm), the fact that it is nearly impossible to gather anatomy and structure information, variable SNR, and lack of standardization in data analysis (Pinti et al., 2018).

Manganese enhanced MRI (MEMRI)

Divalent manganese ion (Mn^{2+}) is a useful contrast agent for imaging the brain with magnetic resonance imaging (MRI). It is paramagnetic and causes strong reduction of both T1 and T2 relaxation time constants of tissue water. T1 is the time required to recover 63% of M_z after a 90^o RF pulse (figure 1.20). The shorter the T1, the greater the shift in the longitudinal magnetization recovery curve to the left. T2 is the transverse component magnetization (M_t) relaxation time. It describes the dephasing of M_t after a 90^o RF pulse. As with T1, M_t never fully relaxes to reach a vector sum of zero but approaches it asymptotically. T2 is the time required for 63% of M_t to be lost. In T1-contrast images, tissues with short T1 constants have high signal, because short T1 values represents fast M_z recovery and large M_0 after the next 90^o RF pulse. For T2-contrast images, tissues with long T2 values are brighter, since long T2 constant indicates a slow dephasing rate, thus the signals remain at a high level.

Mn^{2+} has a high-chemical similarity with calcium (Ca^{2+}), thus it may enter neurons and other excitable cells through voltage-gated calcium channels, the sodium (Na^+)/Ca^{2+} exchanger, the Na+/magnesium (Mg^{2+}) antiporter, and the active Ca^{2+} uniporter in mitochondria. Because Mn^{2+} is paramagnetic and has a distinct effect on T1 values, Mn^{2+}-based functional MRI (fMRI) can therefore be used to produce a contrast is correlated with activity-dependent ion accumulation in excitable cells. Thus, this imaging mode is more directly related to neural activity than fMRI blood oxygenation level dependent (BOLD). The other advantage of MEMRI is that Mn^{2+} uptake after systemic injections takes place over a long time in awake and freely moving animals. It is more

convenient when compared to BOLD fMRI, which requires stimuli and MRI scans to be performed at the same time.

The major drawback of Mn^{2+} application is its toxicity and its potential to causes neurological deficits. Long time exposure to Mn can lead to manganism. An acute over-exposure to Mn^{2+} can result in cardiac toxicity, hepatic failure, and even death.

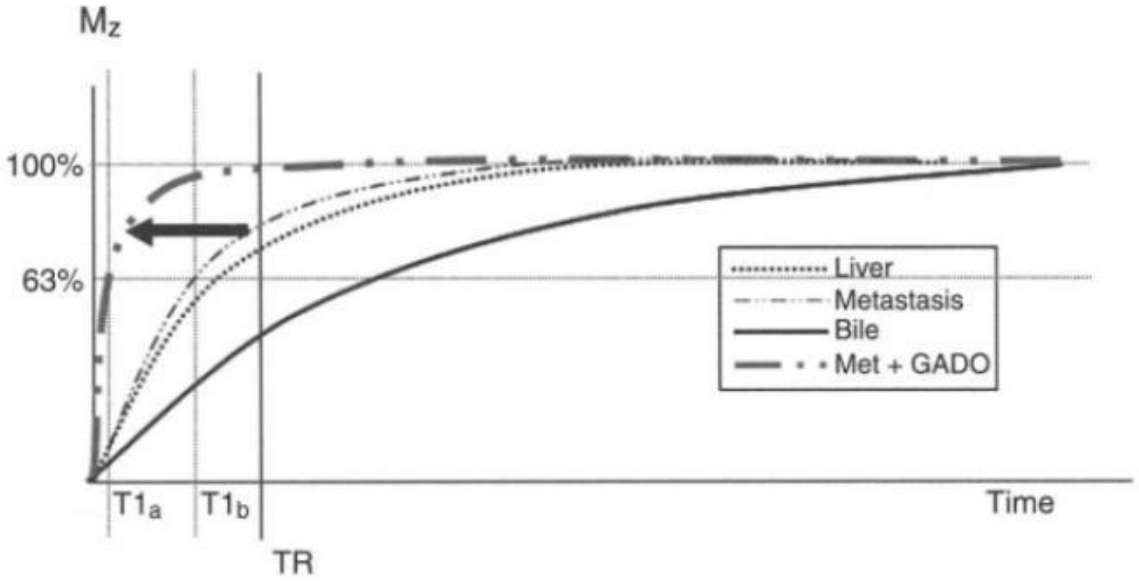

Figure 1.20 T1 shortening effect of gadolinium-containing contrast material (GADO). T1 recovery of metastasis and liver tissue are very similar and hard to distinguish. GADO shortens the T1 of the metastasis (from T1b to T1a) due to tumor vascularity and makes the tissues more distinguishable. The figure is from Lipton and Michael (Lipton, 2010).

There are two ways to deliver Mn^{2+}. The most common way is directly injecting $MnCl_2$ into the brain. Toxicity is the minimum in this way, since Mn^{2+} is restricted to the injection site and adjacent regions. The second way is systemic injection. $MnCl_2$ can be injected intravenously, intraperitoneally or subcutaneously. It has been reported that the

dose can be as high as 175 mg/kg intravenously in healthy rats up to 250 g body weight and in mice up to 25 g body weight. The main consideration for systemic administration is its distribution in organs other than brain, such as liver, kidney and heart, which increases the risk of acute toxic effects.

It is hard for Mn^{2+} to penetrate the blood-brain barrier (BBB), thus it may take 24 h for contrast enhancement to reach equilibrium. BBB disruption is needed to accelerate uptake. After disruption, Mn^{2+} accumulates in active regions at a small scale and does not leave these regions for several hours. Once in the brain, Mn^{2+} can be transported along axons or across synapses. The distribution of Mn^{2+} depends on the accessibility of tissue. Mn^{2+} can infiltrate poorly accessed tissue via axons. Once in the cell, Mn^{2+} accumulates in the endoplasmic reticulum, being subsequently packaged into vesicles and transported in axonal tracts. Finally, it is released from the presynaptic membrane of the first neuron and absorbed by subsequent neurons.

Two-photon excited fluorescence laser scanning microscopy

Two-photon excited fluorescence laser scanning microscopy (TPLSM) enabled imaging of living tissues in vivo (Denk, 1994; Svoboda, Denk, Kleinfeld, & Tank, 1997). It is a functional imaging technique with great temporal resolution and is ideal for studying dynamic processes on the cellular and subcellular level. In a two-photon absorption process, two photons are absorbed to promote a molecular transition. A near-infrared light excites fluorescent dyes, and photons released by the dyes are detected.

The first advantage of TPLSM is the use of near-infrared light. This is because longer wavelength light penetrates deeper and scatters less compared to confocal

microscopy. The second advantage is that the relation between fluorescent signals and the excitation light intensity is not linear. This allows the fluorescence to be concentrated on a focus spot (Frostig, 2009).

TPLSM requires fluorescence labeling. This may be achieved using synthetic organic dyes (traditional dyes), fluorescent proteins, and short peptide sequences. Traditional dyes can be taken up from the intracellular and extracellular space using physical or chemical methods. Fluorescent proteins can be introduced by viral transfections (Dittgen et al., 2004; Lendvai, Stern, Chen, & Svoboda, 2000), targeting using single-cell DNA electroporation (Haas, Sin, Javaherian, Li, & Cline, 2001; Kitamura, Judkewitz, Kano, Denk, & Häusser, 2008), or by generating transgenic animals.

Fluorescent calcium indicators play a very important role in neuroscience. Calcium ion activity underlies many biological processes in almost all cell types and forms the basis for neuronal communication processing (Berridge, Lipp, & Bootman, 2000). These include controlling heart muscle cell contraction (Dulhunty, 2006), and regulating cell cycles from cell proliferation to cell death (Lu & Means, 1993; Orrenius, Zhihotovsky, & Nicotera). Calcium is also a vitally important intracellular messenger in mammalian neurons. During the electrical activity, the intracellular calcium concentration can rise 100 times from 50-100 nM (Berridge et al., 2000). Calcium indicators are used to study calcium-dependent processes such as transmitter release and synaptic plasticity.

Another application is to evaluate electrical excitation from fluorescence measurements. Action potentials require the opening of calcium channels. These brief surges of calcium ions can be indirectly detected by sensitive calcium indicators and thus, neuronal spikes can be indirectly deduced from fluorescence measurements (Yaksi & Friedrich, 2006). Calcium imaging of large-scale neural cell populations therefore has the potential to reveal fundamental principles of network dynamics with the help of electrophysiological methods. Calcium imaging can be achieved by using head-mounted portable mini-microscopes or using head-fixed animals and standard two-photon microscopes (Grienberger & Konnerth, 2012). Specific animal training may be required to habituate animals to head-fixing or head-mounted instrumentation before performing experiments.

In summary, TPLSM is a powerful tool in neuroscience and has advantages in dynamic brain imaging. It allows both structural and function imaging and can be performed over long periods of time (Helmchen & Denk, 2005). TPLSM is limited by its low depth penetration (about 1mm depth in the neocortex (Frostig, 2009)) despite its substantially reduced sensitivity to light scattering. The requirement of fluorescence labeling limits its human applications.

1.5 Functional Imaging During Neurostimulation

Many efforts have been made to understand the mechanisms of brain stimulation. fMRI has been used to study the effects of TMS and DBS (Stefurak et al., 2003). However, the ability of fMRI is limited since it reflects the BOLD signal change, which may not show the stimulated tissues. TMS combined with neuroimaging has shown that

TMS not only influences the stimulated brain region but also affects remote brain areas interconnected with the stimulated location. The effect of TMS also depends strongly on current neuronal excitability state (Ruff, Driver, & Bestmann, 2009), adding more uncertainty to mechanism.

DBS has shown promising results in treating Parkinson's disease, tremor, and dystonia. But there is still debate on whether it inhibits or excites neural activity, and the number of possible explanations is still expanding (Al-Fatly, 2018). It also remains unclear whether DBS causes local or system effects (Montgomery Jr & Gale, 2008).

Interest in tDCS has increased in recent years. It has been used for both neuroscience research and treatment of various neurological and psychiatric disorders. However, there are many questions around tDCS applications, such as inconsistent results found in human experiments, whether the injected current is passing through the scalp into the cortex to modulate neural activity, and how the brain anatomy influences the passage of stimulating current (Wagner et al., 2007). Moreover, it has been observed that even small differences in electrode position can cause entirely different effects (Woods et al., 2015).

Visualization of current pathways inside the brain may be of great use in understanding the mechanisms of electromagnetic brain stimulation methods.

1.6 Magnetic Resonance Electrical Impedance Tomography (MREIT)

Magnetic resonance electrical impedance tomography (MREIT) has been developed to obtain high resolution conductivity images of biological tissue. The basic idea of MREIT is combining MRI with current injections. Pair of orthogonal electric

currents are typically applied through surface electrodes, using a low amplitude (mA) and a short duration (ms) to minimize side effects on biological tissue. The current injection directions should be perpendicular to the main magnetic field (B_0) of MR machine. The externally applied current produces a magnetic field as well as electric field and induces a magnetic flux density (B_z) along the B_0 direction, which can be measured with the MRI scanner. MREIT is derived from magnetic resonance current density imaging (MRCDI), which requires all three components of induced magnetic flux density to be gathered (B_x, B_y, B_z). The current density can be directly calculated using Ampere's law. The defect of this method is that it requires sample rotations, which is unrealistic for clinical MRI.

The drawback was overcome with the introduction of reconstructions based on B_z data alone allows obtaining conductivity image without subject rotation and boosted the development of MR-based approaches to measuring current density and conductivity.

MREIT conductivity image can be reconstructed by using several methods, including the harmonic B_z algorithm (S. H. Oh et al., 2003) or the J-substitution algorithm (Khang et al., 2002).

The relation between the injected current density and the B_z is

$$-\sigma\nabla u = J = \frac{1}{\mu_0}\nabla \times B, \tag{1.20}$$

where μ_0 is the magnetic permeability of the free space, σ is the tissue conductivity distribution, and u is the current induced voltage distribution.

In a spin-echo-based MREIT pulse sequence, current injection is synchronized with the MR pulse sequence, injected before and after the 180^o RF pulse, with the

directions reversed to prevent cancellation. A candidate pulse sequence is shown in figure 1.21. The signal received from the receiver coil is expressed in equation 1.21.

$$S^{\pm}(k_x, k_y) = \iint_{-\infty}^{\infty} M(x,y) e^{i\delta(x,y)} e^{\pm i\gamma B_z(x,y)T_c} e^{-i2\pi(k_x x + k_y y)} dxdy, \quad (1.21)$$

where $S^{\pm}$ represents k-space data obtained using positive current first in each TR or negative current first in each TR, respectively, M is the magnitude image, δ is a systematic phase background, and B_z is the current induced magnetic flux density. After applying a 2-D inverse Fourier transform, the complex image data is obtained as:

$$I^{\pm}(x,y) = M(x,y) e^{i\delta(x,y)} e^{\pm i\gamma B_z(x,y)T_c}. \quad (1.22)$$

The current-induced phase change can be obtained by complex dividing the positive-first injected data with the negative-first injected data:

$$\emptyset(x,y) = \arg\left(\frac{I^{+}(x,y)}{I^{-}(x,y)}\right) = 2\gamma B_z(x,y)T_c. \quad (1.23)$$

The current induced magnetic flux density (B_z) is then obtained as

$$B_z = \frac{1}{2\gamma T_c} \arg\left(\frac{I^{+}(x,y)}{I^{-}(x,y)}\right). \quad (1.24)$$

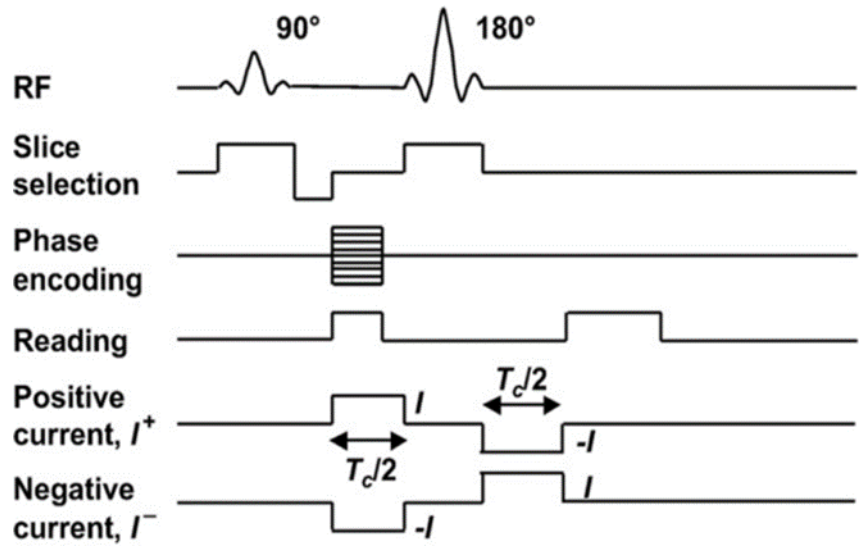

Figure 1.21 Current injection synchronized with spin echo pulse sequence.

The relation between the conductivity distribution and the Laplacian of B_z is:

$$\mu_0 \nabla \times J = \nabla \times \nabla \times B = -\nabla^2 B + \nabla(\nabla \cdot B) = -\nabla^2 B, \tag{1.25}$$

where μ_0 is the magnetic permeability of free space, assumed to be the same as that of biological tissues. Thus

$$\frac{1}{\mu_0}\nabla^2 B = -\frac{\partial J_y}{\partial x} + \frac{\partial J_x}{\partial y} = \left(\frac{\partial \sigma}{\partial x}, \frac{\partial \sigma}{\partial y}\right) \cdot \left(\frac{\partial u}{\partial y}, \frac{\partial u}{\partial x}\right). \tag{1.26}$$

After arrangement of function 1.26 the gradient of conductivity with respect to x and y directions can be written as

$$\begin{cases} \frac{\partial \sigma}{\partial x} = \frac{-\frac{\partial u^b}{\partial x}\nabla^2 B_Z^a + \frac{\partial u^a}{\partial x}\nabla^2 B_Z^b}{\mu_0\left(-\frac{\partial u^a}{\partial y}\frac{\partial u^b}{\partial x} + \frac{\partial u^a}{\partial x}\frac{\partial u^b}{\partial y}\right)} \\ \frac{\partial \sigma}{\partial y} = \frac{-\frac{\partial u^b}{\partial y}\nabla^2 B_Z^a + \frac{\partial u^a}{\partial y}\nabla^2 B_Z^b}{\mu_0\left(-\frac{\partial u^a}{\partial y}\frac{\partial u^b}{\partial x} + \frac{\partial u^a}{\partial x}\frac{\partial u^b}{\partial y}\right)} \end{cases}, \tag{1.27}$$

where a and b represent two independent current injection directions.

We can see that $\frac{\partial u^a}{\partial y}\frac{\partial u^b}{\partial x} \neq \frac{\partial u^a}{\partial x}\frac{\partial u^b}{\partial y}$, this can be achieved by setting

$$J_x^a J_y^b \neq J_y^a J_x^b, \tag{1.28}$$

which implies that two current densities cannot be collinear (Seo, Yoon, Woo, & Kwon, 2003).

1.7 Measurement of Active Tissue Conductance Changes Relating to Neural Activity Using MREIT-fMREIT.

Neural activity causes changes in membrane conductance as introduced in the Hodgkin-Huxley model. This alters the path of the externally injected current. If neural activity occurs during the MREIT experiments, the conductivity increase of voxels within

an active region should be observed in the MREIT conductivity images. Previous simulation work (R. J. Sadleir, Fu, & Chauhan, 2019; R. J. Sadleir, Grant, & Woo, 2010) has demonstrated the feasibility of imaging of small cell with high signal to noise ratio (SNR) and moderate resolutions. MREIT current injections may modulate neural activity levels, thus making it appropriate for studying electrical neuro-stimulation involved research.

1.8 Specific Aim and Significance

Specific Aim One: Demonstrate Neuronal Activity Detectability with Functional MREIT.

fMREIT will be used to detect changes in spontaneous spiking levels in the AAG. Our benchtop experiments on Aplysia abdominal ganglion (AAG) showed that the spontaneous neuronal activity can be halted by potassium chloride (KCl) administration. A region of interest (ROI) will be chosen inside the ganglion. Statistical analyses will be applied to determine phase standard deviation inside the ROI. Comparisons of control and KCl treated groups will be used to determine differences caused by the neuronal current changes.

Specific Aim Two: Synchronize Neuronal Activity with Current Injection to Improve the Neuronal Current Detectability.

Phase changes induced by neuronal activity should be enhanced if current is injected during evoked neural activity. The current used in MREIT will be synchronized with the retina ganglion neuronal activity evoked by light stimulation. Similar analysis methods to those in SA1 will be used. We hypothesize that differences between images

with and without neuronal activity should be more distinct than in AAG experiments. We will also seek to determine if different responses are evoked in different retinal regions.

2 BENCHTOP EXPERIMENTS ON THE APLYSIA ABDOMINAL GANGLION

The following work was published in Biomedical Physics & Engineering Express (Fu, Chauhan, & Sadleir, 2018).

Spontaneous activity in the abdominal ganglion of Aplysia can be used as a convenient bioelectricity source in tests of fMREIT. In these tests, it is necessary to find a consistent treatment that modulates neural activity, so that these results can be compared with control data. Effects of MREIT imaging currents combined with treatment were also of interest. Potassium chloride (KCl) was employed as a rhythm modulator. In a series of experiments, effects of adding different volumes of KCl solution were tested and compared with experiments on control groups that had artificial sea water administered. In all cases, neuronal activity was measured with microelectrode arrays. It was found that it was possible to reversibly stop spontaneous activity in ganglia by increasing the extracellular potassium chloride concentration to 89 mM. There was no effect on experimental outcomes when current was administered to the sample chamber between MEA recordings. It was concluded that KCl can be used as a reversible neural modulator for testing neural detection methods.

2.1 Introduction

In this study, different volumes of concentrated potassium chloride (KCl) solution were administered to tissue preparations to determine their effects on this tissue, and to assess if KCl could be used to consistently decrease neural activity. Previous studies have shown that show that moderate increases in extracellular potassium concentration can

change neural activity patterns and increase spiking rates (Dominguez & Fozzard, 1970). This effect was also used in a previous fMREIT study (R. J. Sadleir et al., 2017). However, the relation between KCl concentration and AAG activity has not been thoroughly investigated. We also combined KCl administration with an MREIT-like current injection to see if current combined with this treatment produced changes in spontaneous AAG activity levels. The effect of KCl on AAG samples was measured using microelectrode arrays. Because the purpose of the study was to verify the feasibility of using KCl as a neural activity modulator in the context of fMREIT experiments, our experiments tested effects of adding either of two different concentration doses of KCl into the artificial sea water (ASW) containing the preparation. We did not consider the precise patterns of neural activity in this study, since we wished only to assess changes in relative activity levels when different amounts of KCl were added, and when current injection was combined with this treatment. Matched controls were employed in all cases. Finally, we were also curious to discover if any treatment effects from KCl were reversible, therefore we tested the response of ganglia treated with KCl to the removal of the solution and reinfusion with ASW.

2.2 Method

2.2.1 Animal Handling

Thirty-six late juvenile (around 50 g) Aplysia Californica were obtained from NIH/University of Miami National Resource for *Aplysia* Facility. After delivery, animals were maintained in an aquarium tank filled with artificial sea water (ASW). The ASW was composed of deionized water and sea salt (Instant Ocean, Spectrum Brands,

Blacksburg, VA, USA). The overall salinity was adjusted to 30 ppt, and the environmental temperature was set to 16 C^{o}. The initial molarity of potassium in the ASW was 8.24 mM (Atkinson & Bingman, 1997). Prior to experiments, Aplysia were fed with dried seaweed sheets (OMEGA ONE, Omega Sea LLC, Painesville OH, USA) every three days.

2.2.2 Dissection

The Aplysia were anesthetized with $MgCl_2$ solution (77 g/L of $MgCl_2$ and 3.6 g/L of HEPES buffer). After muscles relaxed fully, the foot was cut open and the ganglion was removed. Following removal, the ganglion was stored in ASW.

2.2.3 Equipment Setup

A 3-D printed sample chamber was constructed to house the AAG (figure 2.1(b)). The cylindrical chamber had a diameter of approximately 12.5 mm. Four equally spaced holes (diameter 2 mm) were printed into one plane of the sample chamber for MREIT electrode placement. Copper sheets were used as MREIT electrodes. A Multichannel Systems (Reutlingen, Germany) Flex MEA36 microelectrode array (MEA) was inserted into the chamber base via a rectangular slot at the bottom of the chamber. The array was fixed to the chamber base with double sided tape, and the slot was sealed with Teflon tape.

A good connection between AAG and the MEA is key to achieving successful recordings. We applied a cellulose nitrate coating to the MEA (Egert & Meyer, 2005) to ensure the ganglion did not move during the experiment. Nitrocellulose stock solution was made by dissolving 25 mg (5 cm^2) nitrocellulose transfer membranes (protran®

BA83/85) in 2 ml of 100% methanol. A working solution was made by diluting the stock solution with methanol in a ratio of 1:10. Five microliters of working solution were then introduced on the surface of the MEA and allowed to dry for approximately 3 mins. The AAG was then gently pushed down onto the MEA with tweezers. The ganglion orientation used was the same for each experiment (figure 2.1(d)).

During experiments, the chamber was placed in a small grounded metal enclosure to minimize environmental electromagnetic interference. The enclosure was located on a vibration isolation table (Newport Corporation, Irvine, CA, USA) to avoid movement noise (figure 2.1(c)). Microscope (ZEISS) images were collected after each ganglion was positioned on the MEA. A current source system from Tucker-Davis Technologies (RZ5D BioAmp Processor, IZ2 Stimulator) was used for current injection.

2.2.4 Experimental Design

Three different groups of experiments were designed to investigate the behavior of the ganglia when different volumes of KCl was added, with or without current injection. The KCl solution was made by adding 0.6 g KCl to a 20-ml volume of ASW, thus the concentration of potassium in the KCl solution was 411 mM. For each experiment, the treatment (KCl) group was matched to a control (ASW) group. There were six specimens in each group. We sought to quantify the effect of these factors by counting the number of spikes generated by ganglia in the treatment groups, compared to those in control groups. All experiments commenced with the ganglion in 200 µl of ASW solution.

In the first group of experiments, the treatment consisted of 20 µl of KCl solution. Addition of the treatment increased the extracellular potassium concentration to 39 mM. The experimental procedure used was the same as proposed for fMREIT experiments, as shown in figure 2.2. There were 35-minute gaps between recordings. In fMREIT experiments, these periods would be used for imaging. The 20 µl KCl solution was added into the sample chamber with a micropipette after the third recording. The second group was the same as the first, but the volume of KCl solution added was 50 µl (final potassium concentration 89 mM). The third group used 50 µl KCl treatments, as well as interleaving MEA recordings with current injections between recordings 2 and 3, 5 and 6, and 7 and 8. Where current was used, the current produced by the current source was bipolar. Each pulse had a width of 8 ms, an amplitude of 250 µA and a frequency of 1 Hz (figure 2.3). Combination of current administration with KCl or ASW administration served to confirm that persistent changes were not caused by current administration, allowing us to confirm that changes in activity levels were likely due to ionic concentration changes alone. In actual fMREIT experiments, where variability in magnetic flux density distributions are measured (R. J. Sadleir et al., 2017; Sullivan & Feinn, 2012), changes in bulk solution conductivity should not result in changes in current density distributions. However, increases in media volume caused by control or treatment administration may cause dilution of current density and therefore a slight decrease in current densities in the neighborhood of ganglia. Conductivities of ASW and KCl-doped solutions were measured to be approximately 5.7 and 6.3 sm^{-1} respectively.

Increasing the media volume from 200 µl to 250 µl resulted in a decrease in magnetic flux densities of approximately 0.15%.

2.2.5 Recovery Observation

In the treatment group of Experiment 2, we monitored for AAG recovery activity after KCl was removed and replaced by ASW. Therefore, after recording 8, the solution in the chamber was removed and replaced with 200 µl ASW. A one-hour recording of AAG activity was obtained immediately afterwards to monitor the recovery response.

2.2.6 Data Processing

MC_Rack software (MultiChannel Systems) was used to visualize and record the neural activity and to detect and count spikes. Each recording lasted 9 mins. Neural spikes were detected using the spike sorting function built into the MC_Rack. A sample of 500 ms of background noise at the beginning of each data trace was used to calculate noise standard deviations. A spike was defined as having an amplitude 5 times the noise standard deviation (5σ).

Recorded ganglion activity levels vary widely between samples due to factors such as differences in connective tissue thickness, positions of ganglia relative to MEA electrodes, and electrode contact quality as well as individual anatomical and baseline differences between animals, thus a normalized statistical analysis was used to reveal typical behavior changes. After spike detection, all spike counts for all ganglia were normalized to an initial value of 100. The normalized spike count data from all 32 flexMEA channels was computed over each 10 min recording. Normalized recordings from all 6 specimens in each control or treatment group were used to calculate the mean

and standard deviation in spike rates at each time point. Treatment and control group data were compared using Welch's t-tests. Significance was set at $\alpha = 0.05$. We used Cohen's d value to quantify effect sizes (Sullivan & Feinn, 2012), that is

$$d = \frac{M_1 - M_2}{SD_{pooled}}, \tag{2.1}$$

such that

$$SD_{pooled} = \sqrt{\frac{{SD_1}^2 + {SD_2}^2}{2}}, \tag{2.2}$$

where M_1 and SD_1 were the mean and standard deviation of the initial measurement in each experiment respectively (recording 1, $M_1 = 100$, $SD_1 = 0$), and M_2 and SD_2 were the mean and standard deviation of the subsequent recording data (recordings 2-8) in each experiment.

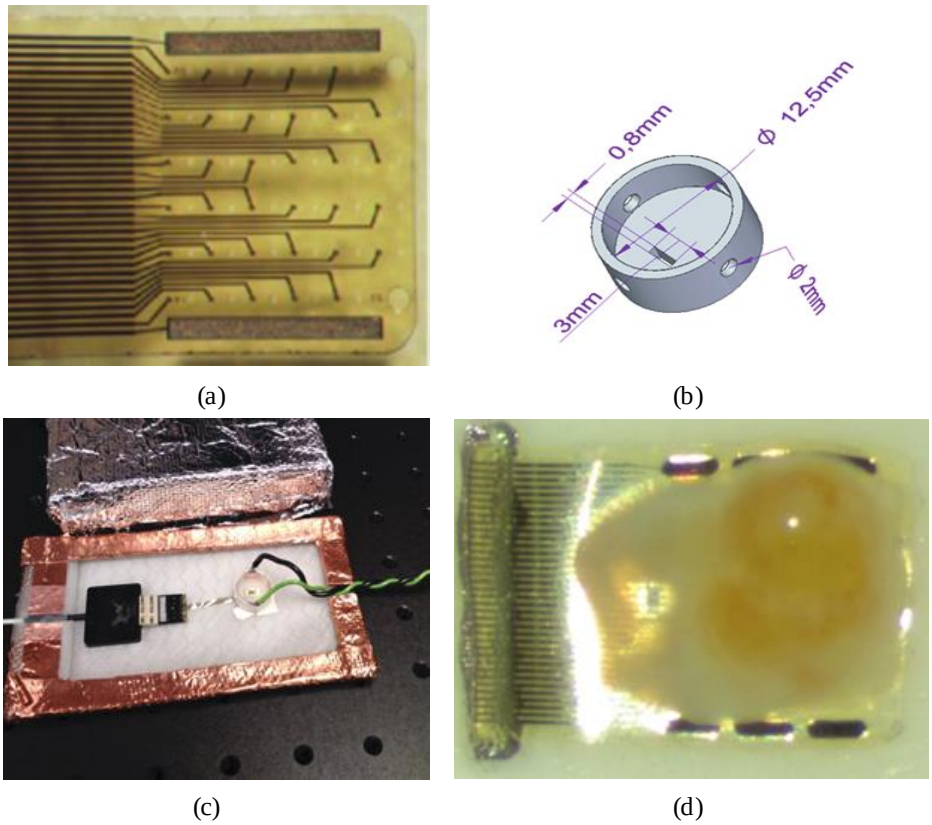

(a) (b)

(c) (d)

Figure 2.1 Pictures of MEA and sample chamber showing (a) 32-channel flexible multi electrode array (flexMEA) (Multichannel Systems, Reutlingen, Germany). (b) Sample chamber schematic, with dimensions. There were four ports in the perimeter for current introduction. A slot at the bottom was used to introduce the flexMEA. Part (c) shows a close up of the experiment setup. The metal enclosure was used to shield environmental electromagnetic fields. Part (d) shows a ganglion placed on an MEA.

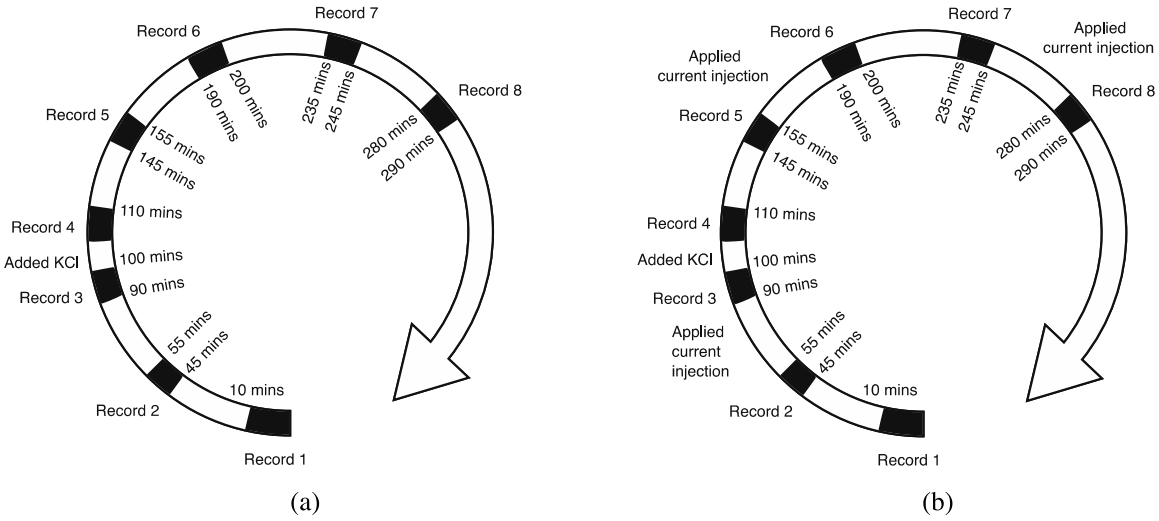

Figure 2.2 Experimental schedule. Part (a) shows the procedure for the first and second experimental groups. Part (b) shows the procedure used for groups in the third experiment involving current injection.

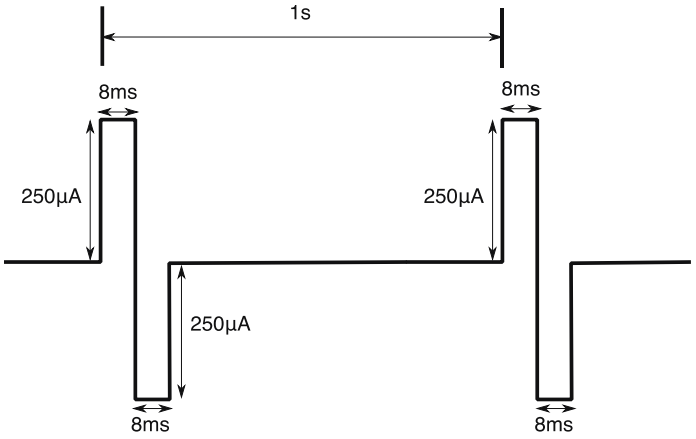

Figure 2.3 Current patterns used in Experiment 3 protocol.

2.3 Results

2.3.1 Effects of K^+ Concentration and Current Administration

Figure 2.4 shows the results of the three initial experiments. We found that normalized spike rates decreased continuously in the 200 mins after administration of 20 µl of KCl solution (figure 2.4(a)). By comparison, normalized spike rates in the control (ASW) group stayed relatively constant over the same period, with the smallest mean normalized spiking rate in this group post ASW administration being 73% of original rates. Five minutes after administration of 50 µl KCl to the treatment group of Experiment 2, ganglion activity ceased in all cases (no spikes detected, figure 2.4(b)). This was also found in Experiment 3, where 50 µl administration was combined with current injection (figure 2.4(c)).

2.3.2 Effect Sizes and Statistical Comparisons

Welch's t-tests assume unequal variance and are similar to one-tailed unpaired t-tests. Table 2.1 shows effect sizes (compared to initial spike rates) and Welch's t-test results comparing control and treatment groups for each experiment. Tests were performed comparing groups at each experimental time point, except Recording 1, which was used to normalize data. Significant differences were found between treatment and controls for 50 µl groups in all instances of recordings 5-8 (post media addition). There were no significant differences found between control and treatment groups in Experiment 1 until 240 mins after media administration (at Record 7). Effect sizes in Experiments 2 and 3 were very large in all post-administration recordings, with typical values in recordings 5-8 being over 100.

Table 2.1

Effect sizes and p values in experimental comparisons for Experiments 1, 2 and 3. Effect sizes compare initial control (C) and treatment (T) measurements (Record 1) with subsequent measurements. Welch's t-test p values are also shown comparing normalized control and treatment spike data at each time point. Effect sizes (C or T) or p values are indicated by the measure (M) column. Recording 1 (R1) results are not shown because they were used to normalize data. Significance was set at $\alpha = 0.05$. Significant differences are denoted in red text, effect sizes > 10 are highlighted with green text.

Exp	M	R1	R2	R3		R4	R5	R6	R7	R8
(1) 20µl	C	-	1.1	-0.15	Solution Added	1.58	1.00	-0.07	0.036	0.145
	T	-	-0.27	-0.253		1.64	3.64	7.80	14.22	28.03
	p	-	0.7989	0.6114		0.0722	0.0121	0.0506	0.035	0.0168
(2) 50µl	C	-	-0.33	-0.44		1.08	1.09	0.91	1.12	0.67
	T	-	-0.11	-0.03		3.53	756	513	857	641
	p	-	0.5294	0.3677		0.0127	0.0019	0.0053	0.0043	0.0059
50µl (3) + Current	C	-	-1.2	-1.4		-0.38	-0.47	0.19	0.04	0.52
	T	-	-0.01	-0.37		7.9	100	219	199	176
	p	-	0.1232	0.4528		0.0096	0.0018	0.0163	0.0207	0.0299

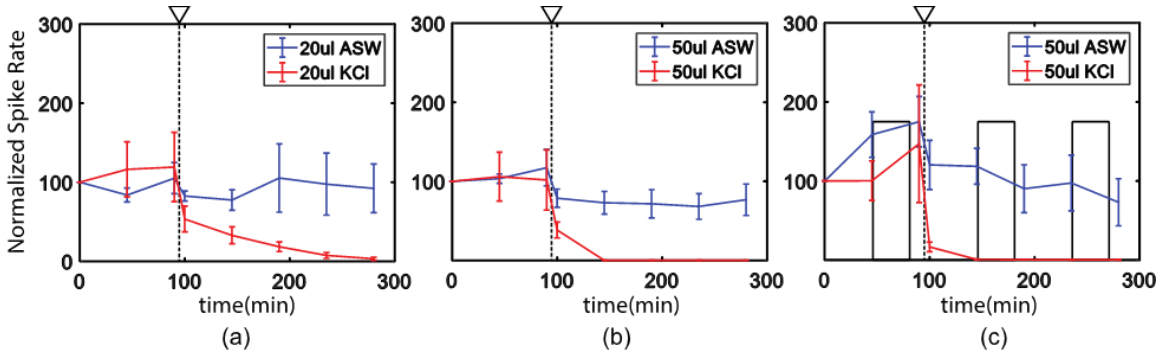

Figure 2.4 Averaged normalized ganglion activity in each experiment. Comparison of pooled control and treatment groups for (a) 20 µl KCl, (b) 50 µl KCl and (c) 50 µl KCl combined with current administration experiments. Error bars indicate standard errors. Dotted lines in each plot indicate media administration time points. Black rectangles in (c) represent current injection periods between monitoring periods.

2.3.3 Observation of Recovery

In Experiments 2 and 3, we observed that ganglion activity ceased consistently after 50 µl of KCl treatment solution was added. This behavior was observed in the initial data obtained for the 6 animals used in the recovery experiment. These animals were the treatment group for Experiment 2. Normalized data for each of the six animals monitored in this test are shown in figure 2.5. It is clearly from figure 2.5 that all ganglia recommenced spiking after the solution was changed to ASW, with all animals producing spikes at 40 mins after treatment solution was replaced with 200 µl of control media.

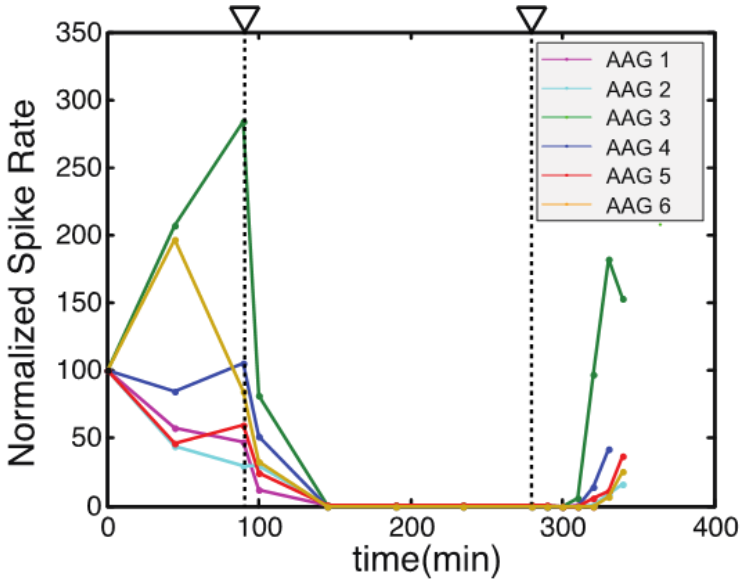

Figure 2.5 Normalized data from animals in the 50 µl KCl treatment recovery experiment. AAG 1-6 were the treatment group from Experiment 2. Dotted lines indicate times at which the KCl solution was added, and when ASW solution was restored to the ganglion.

Figure 2.6 shows raw neural activity recordings from one ganglion in the recovery group (AAG 5). Five sets of recordings are shown, at two different timescales. The left side of figure 2.6(a) shows short-term recordings on a scale of 1 second, whereas the right side (b) shows the recording over a 10-minute time period. Each sub-image shows signals from each electrode of the 32-channel array shown in figure 2.6(a). For this AAG, the spiking rate was on average 1 spike/second at the beginning at the experiment. The AAG became more active (a maximum of 3 spikes/second) in the first minute after KCl treatment, but activity was not detected after 3 mins. After the original solution was replaced by ASW, activity did not recover immediately. However, spiking recommenced

40 mins post-ASW replacement, as shown in the last recording in figure 2.6(b). At this point the maximum spiking rate in some channels was 3 spikes/s, but overall spiking was depressed, leading to a lower average spike rate. Similar behavior time courses were observed in other samples.

2.4 Discussion

In our experiments, we found out that increasing the potassium ion concentration from 8.24 mM to 88.72 mM caused activity in the AAG to cease. Interleaving MEA monitoring with 250 μA current injection did not change this result, which indicates that these external currents did not persistently affect activity levels.

Increases in extracellular potassium concentration should raise resting membrane potentials. This is because intracellular potassium concentrations are typically much higher than extracellular ones and increases in extracellular potassium concentrations should reduce potassium Nernst potentials, depolarizing cell membranes, and possibly making them more excitable. Neural membrane potential was found to be linearly related to the log of extracellular potassium concentration in a range that depends on the tissue species (Huxley & Stämpfli, 1951; Nicoll, 1979), at higher concentrations. However, membrane depolarization does not always lead to greater excitability (Malenka, Kocsis, Ransom, & Waxman, 1981). Extended depolarizations have been found to result in reduced sodium inactivation, ultimately leading to conduction failure (Allan L Hodgkin & Andrew F Huxley, 1952). For example, Hablitz and Lundervold (Hablitz & Lundervold, 1981) found that when the concentration of extracellular K+ was higher than 15.25 mM, evoked activity in guinea pig hippocampal slices terminated. This behavior

was reversible in most cases, with spiking resuming when the tissue was returned to a 3.25 mM potassium environment. Hablitz and Lundervold's study was not able to follow the time course of the activity cessation, but it is possible that activity in their tissue followed a similar time course to that found in our study, that is, that activity increased for a short period of time following administration of the high concentration KCl solution, after which time it stopped.

Studies of osmotic stress and ion stress also point out a potential mechanism for neuron behavior during these manipulations. Addition of high-concentration potassium to extracellular space may have resulted in cell shrinkage, which is likely to be reversible, whereas use of smaller concentrations of potassium may have resulted in cell swelling. In Pichon and Treherne's study on M. squinado (Pichon & Treherne, 1976), it was reported that a hyperpolarization of the axon and decline in the amplitude of action potentials occurred after salinity in the external medium was reduced. It was supposed that osmotic swelling increased potassium permeability of the axonal membrane and led to a net potassium efflux. It is also possible that a reverse mechanism may manifest, that is, that osmotic shrinking decreases potassium permeability and overall activity.

We note two limitations in this experiment. Firstly, we set a 5σ threshold for spike detection. Thus, for Experiments 2 and 3, we cannot say that that AAG activity stopped completely after KCl addition. It is possible that spike amplitudes decreased and were too low to be detected, while spiking rates stayed the same. Second, in our analysis we summed all channel data to obtain an average number representing each recording, which means that there was no spatial discrimination in our experiment. A more detailed

experiment would investigate effects on individual channels or structures within the ganglion. However, on average, it was clear that KCl solution inhibited all neural activity after the 50 µl of the 411 mM KCl solution was added. Finally, MEA recordings were not synchronized with current injection, since spike detection was complicated by the presence of external current injection waveforms. Therefore, differential spike rates during current injection could not be directly measured. However, the result of the third experiment showed that the external current injection did not persistently modulate the neuronal activity. This is important because if baseline activity was changed by current administration alone this may confound treatment effects relative to controls.

Our results indicate that this treatment should be useful for MREIT experimental models, as it affected the ganglia in a rapid, consistent and reversible way. This reversibility may be an advantage compared to other treatments such as TTX. Further experiments should be performed to investigate the relationship between KCl concentration and activity level changes in more detail.

2.5 Conclusion

It was found that increasing extracellular potassium concentration to approximately 90 mM can be used to rapidly inhibit AAG activity. The current injection protocol used in our experiment did not appear to affect activity levels. The effect of KCl administration could be reversed by rinsing the preparation in ASW, which may be useful in experimental settings where repeated images are gathered on the same animal. We conclude from these observations that hypertonic KCl can be used to reliably manipulate neural activity levels in functional neuroimaging experiments.

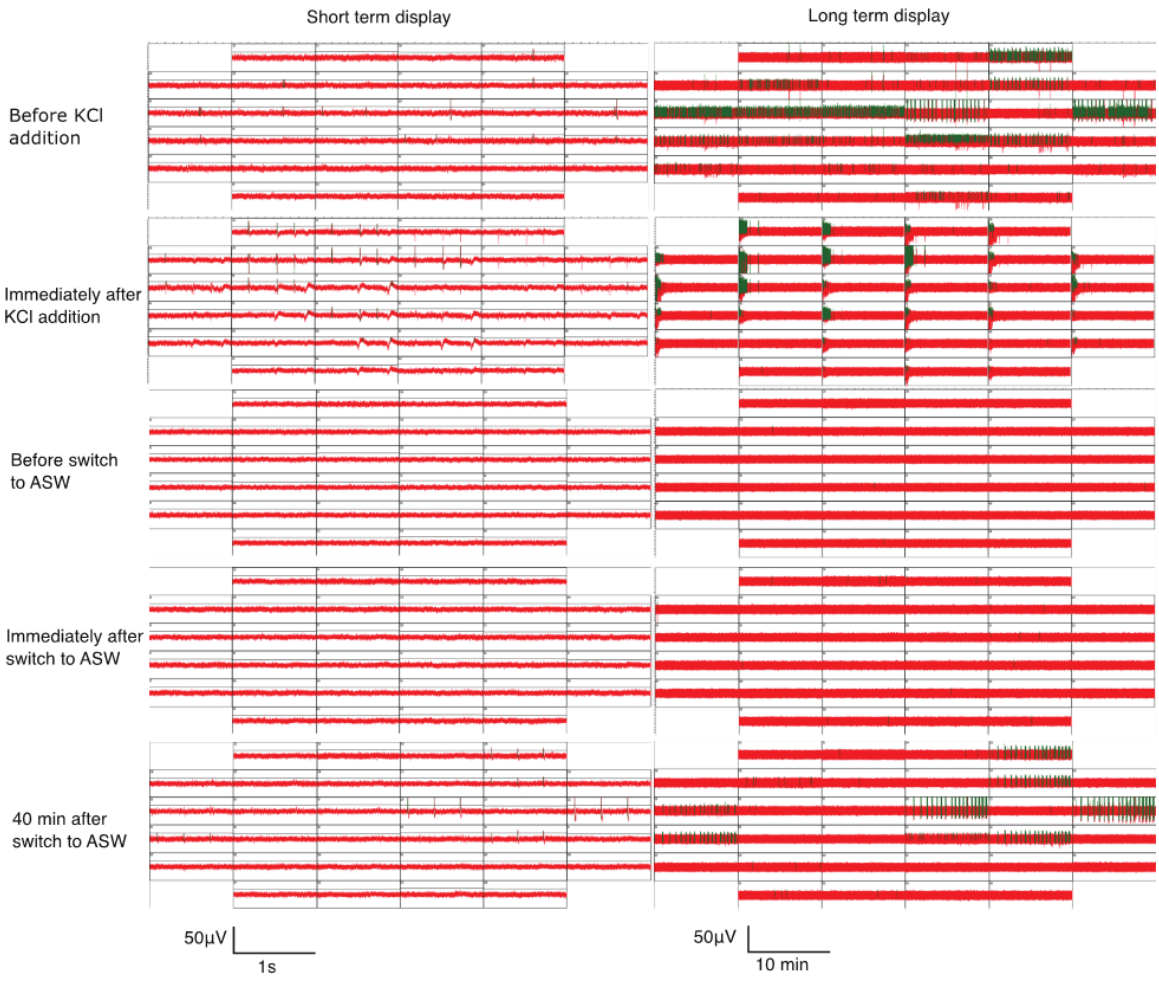

Figure 2.6 Recordings from AAG 5 in treatment recovery group (treatment AAGs from Experiment 2), showing typical responses before and after each manipulation stage. Part (a) plots show 1 s of recording from all 32 channels, and (b) show 10-minute recordings for all channels. Detected spikes are indicated with green lines.

3 FUNCTIONAL MREIT SIMULATION

The following work was published in *Magnetic Resonance in Medicine* (R. J. Sadleir et al., 2019).

3.1 Introduction

It has been reported that MREIT has the potential to detect membrane conductivity changes during neural activity (R. J. Sadleir et al., 2010). Later, the existence of this contrast was demonstrated in the AAG using an 11.75 T MR machine (R. J. Sadleir et al., 2017). In this chapter, a bidomain model combined with Hodgkin-Huxley equations was used to extend the simulation of MREIT imaging in Sadleir et al. (R. J. Sadleir et al., 2010) to further demonstrate the ability of MREIT to detect neural activity. This model can be used to estimate the signal sizes of the AAG MREIT experiments. The bidomain model predicts the average electrical properties over a group of cells (Henriquez, 1993). This time-dependent, active membrane model is more advanced than Sadleir et al. (R. J. Sadleir et al., 2010). Thus, it provided improved estimates of fMREIT signal magnitudes. The geometry of the model was chosen to be on the same scale as real AAG fMREIT experiments.

The simulated fMREIT images were calculated at a resolution similar to those found in real experiment, and activity related changes in these images were compared with typical high field MR noise levels. Three external current amplitudes and four internal source strengths were applied. Laplacians of conductivity difference images of

the bidomain model were computed using the Harmonic B_z MREIT reconstruction method (Seo et al., 2003) described in chapter 1.

3.2 Methods

3.2.1 Bidomain Model

The bidomain model (Henriquez, 1993; Tung, 1978) is an approximation of the average electrical properties of active tissue. The intracellular and extracellular spaces, coupled with a passive or active membrane, constitute the bidomain model. The two spaces share current density J_i and J_e, respectively (i for intracellular and e for extracellular). This can be expressed as

$$\nabla \cdot J_i = -\nabla \cdot J_e = i_m, \tag{3.1}$$

where i_m is the transmembrane current per unit volume, measured in Am^{-3}. The current densities J_i and J_e are defined as

$$J_i = -\nabla V_i,$$

$$J_e = -D_e \nabla V_e, \tag{3.2}$$

where D_i and D_e are the conductivity tensors, which are the multiples of the identity matrix, because it was assumed that the tissue was isotropic. The transmembrane voltage V_m is defined as

$$V_m = V_i - V_e, \tag{3.3}$$

where V_i and V_e are the intracellular and extracellular potential distributions, respectively. The Hodgkin-Huxley model was used to define the transmembrane current as described in chapter 1. The function is repeated as below. The membrane current is described by:

$$I_m = \beta(C_m \frac{dV_m}{dt} + (V_m - V_{Na})G_{Na} + (V_m - V_K)G_K + (V_m - V_L)G_L), \quad (1.6)$$

and the conductance of potassium and sodium channels are described by:

$$G_K = G_{K\,max} n^4, \quad (1.2)$$

$$G_{Na} = G_{Na\,max} m^3 h, \quad (1.3)$$

where

$$\frac{\partial n}{\partial t} = \frac{1}{\tau_n}(n_\infty - n),$$

$$\frac{\partial m}{\partial t} = \frac{1}{\tau_m}(m_\infty - m),$$

$$\frac{\partial h}{\partial t} = \frac{1}{\tau_h}(h_\infty - h). \quad (3.4)$$

Equation 3.4 is equivalent to equation 1.4. The parameters τ_k and k_∞ (k = n, m, h) will be given later. The bath potential V_o is described by the equation:

$$\nabla \cdot (\sigma_o \nabla V_o) = 0, \quad (3.5)$$

subject to

$$\int_{\partial\Omega_0} I_0 = 0 \text{ and } \frac{\sigma_0 \partial V_0}{\partial n} = J_0 \text{ on } \partial\Omega_0, \quad (3.6)$$

where $\partial\Omega_0$ is the surface of the medium containing the active tissue, I_o is the current passing through the bath boundary, **n** is the unit vector normal to its surface, and J_o is the current density normal to electrode surfaces. Equation $V_o = V_e$ was specified at the boundary between the active tissue and the bath.

The equations describing the relation of transmembrane and extracellular voltages is described below (Vigmond, Dos Santos, Prassl, Deo, & Plank, 2008):

$$\nabla \cdot (\sigma_i \nabla V_m) + \nabla \cdot (\sigma_i \nabla V_e) = i_m \pm i_{source},$$

$$\nabla \cdot ((\sigma_i + \sigma_e)\nabla V_m) + \nabla \cdot (\sigma_i \nabla V_m) = 0, \quad (3.7)$$

where i_{source} is an internal source. The boundary equations for V_m and V_e are

$-n \cdot (\sigma_i \nabla V_m + \sigma_e \nabla V_e) = 0$ and

$$V_e = V_o. \tag{3.8}$$

The V_m and V_e equations describe the electromagnetic behavior in the intracellular and extracellular space averaged over the active tissue.

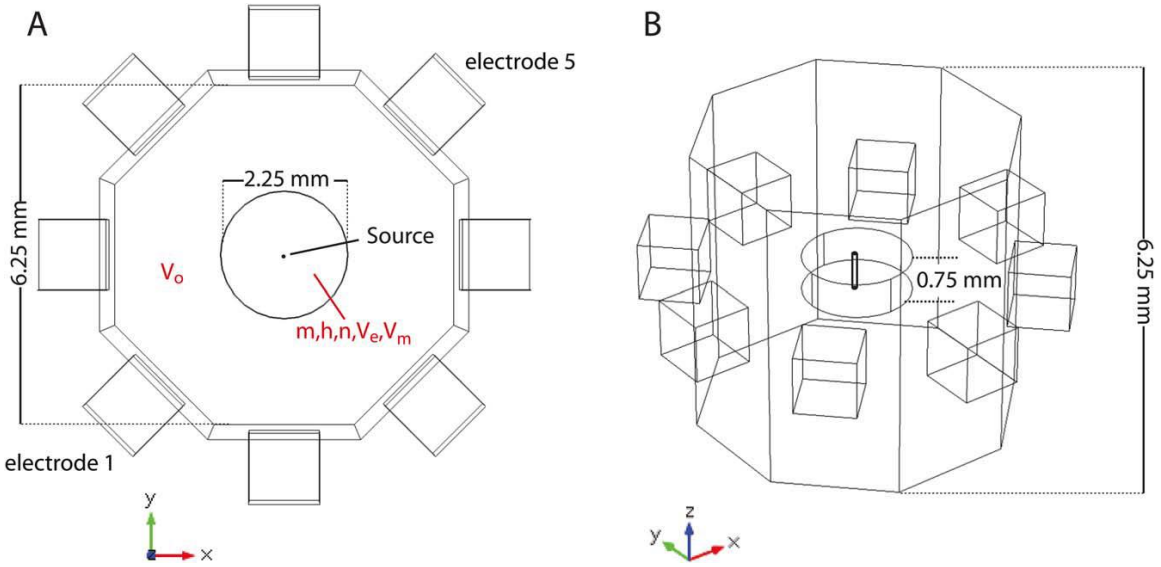

Figure 3.1 Cross-sectional (A) and oblique (B) views of the model geometry. The current injection was applied through electrode 1 and 5 as shown in (A). The center column represented the tissue domain with a 2.25 mm diameter and a 0.75 mm thickness. The sample chamber was a 6.25 mm high and 6.25 mm wide octagon with eight 1.25 mm cube electrodes attached to the wall. Variables V_e, V_m, m, h, and n were solved in the tissue region. V_o was used to solve the voltages in the sample chamber and current injection ports. The internal current source was a column at the center of the model with a 70 µm diameter and a 0.75 mm height, is shown in both panels. This figure is from Sadleir et al.(R. J. Sadleir et al., 2019).

3.2.2 Finite Element Model Description

The model used in simulations is shown in figure 3.1. The AAG was represented by the small disc in the center. It had a diameter of 2.25 mm and a thickness of 0.75 mm. The bath was filled with saline and had eight current injection ports attached. The model was formulated in COMSOL (Comsol Inc, Burlington, MA) and included three ordinary differential equations (3.4) and three partial differential equations (3.7) and (3.8). The tissue conductivity and electric properties of the membrane were taken from Sadleir et al. (R. J. Sadleir et al., 2010). The intracellular conductivity (σ_i), surface to volume ratio (β), tissue channel conductance (g_k^{max}), and membrane capacitances (C_m) were taken from Foster et al. (Foster, Bidinger, & Carpenter, 1976) and Malmivuo et al. (Malmivuo & Plonsey, 1995). The extracellular and bath conductivity (σ_e and σ_o) were equivalent to the ASW conductivity (5.8 S/m) (R. J. Sadleir et al., 2017). The axoplasm conductivity (σ_i) equaled rASW/1.4 (3.63 S/m), as suggested in Foster et al. (Foster et al., 1976). All the parameters and variable names are specified in tables 3.1, 3.2, and 3.3.

Table 3.1

Hodgkin Huxley model constants.

Parameter	Value[unit]
β	20000 m^{-1}
g_{Na}^{max}	240 S/m^2
g_K^{max}	30 S/m^2
g_{leak}	2.5 S/m^2
E_{Na}	55 mV
E_K	-90 mV
E_{leak}	-70 mV
θ_h, ζ_h	-53 mV, -7 mV
θ_{ht}, ζ_{ht}	-40.5 mV, -6 mV
θ_m, ζ_m	-30 mV, 9.5 mV
θ_{mt}, ζ_{mt}	-27 mV, -15 mV
θ_n, ζ_n	-30 mV, 10 mV
θ_{nt}, ζ_{nt}	-27 mV, -15 mV
C_m	0.01 F/m^2
V_r	-69.965 mV

Table 3.2

Hodgkin Huxley parameter expressions.

Variable	Definition
i_m	$i_m = \beta(C_m \frac{\partial V_m}{\partial t} + I_{Na} + I_k + I_{leak})$
I_{Na}	$I_{Na} = g_{Na}^{max} m^3 h (V_m - E_{Na})$
I_K	$I_K = g_K^{max} n^4 (V_m - E_n)$
I_{leak}	$I_{leak} = g_{leak}(V_m - E_{leak})$
h_∞	$h_\infty = S(V_m, \theta_h, \zeta_h)$
m_∞	$m_\infty = S(V_m, \theta_m, \zeta_m)$
n_∞	$n_\infty = S(V_m, \theta_n, \zeta_n)$
τ_h	$\tau_h = 0.37 \times 10^{-3} + 2.78 \times 10^{-3} S(V_m, \theta_{ht}, \zeta_{ht})$
τ_m	$\tau_m = 0.37 \times 10^{-3} + 1.85 \times 10^{-3} S(V_m, \theta_{mt}, \zeta_{mt})$
τ_n	$\tau_n = 0.37 \times 10^{-3} + 1.85 \times 10^{-3} S(V_m, \theta_{nt}, \zeta_{nt})$
h_∞^0	$h_\infty^0 = S(V_r, \theta_h, \zeta_h)$
m_∞^0	$h_\infty^0 = S(V_r, \theta_m, \zeta_n)$
n_∞^0	$h_\infty^0 = S(V_r, \theta_n, \zeta_n)$
$S(\cdot)$	$S(V, \theta, \zeta) = \frac{1}{1 + e^{-(V-\theta/\zeta)}}$

Table 3.3

Variables used in COMSOL bidomain model with corresponding equations, boundary conditions, initial values and parameters:

Variable	Equation	Boundary Conditions	Initial Value	Parameter Values
V_0	$\nabla \cdot (\sigma_o \nabla V_o) = 0$	$V_o = V_e$ $on\ \partial\Omega_e$	$V_o = 0$	$\sigma_o = 5.8 S/m$
V_m	$\nabla \cdot (\sigma_i \nabla V_m) + \nabla \cdot (\sigma_i \nabla V_e) = i_m \pm i_{source}$	$-\mathrm{n} \cdot (\sigma_i \nabla V_m + \sigma_e \nabla V_e)$	$V_m = V_r$	$\sigma_e = 5.8 S/m$ $\sigma_i = 3.63 S/m$ i_m: $Table$ 3.2 i_{source}: $Figure$ 3.2
V_e	$\nabla \cdot \left((\sigma_i + \sigma_e)\nabla V_m\right) + \nabla \cdot (\sigma_i \nabla V_m) = 0$	$V_e = V_o$ $on\ \partial\Omega_e$	$V_e = 0$	
h	$\frac{\partial h}{\partial t} = \frac{1}{\tau_h}(h_\infty - h)$	insulation	$h_{initial} = h_\infty^0$	τ_h: $Table$ 3.2 h_∞^0: $Table$ 3.2
m	$\frac{\partial m}{\partial t} = \frac{1}{\tau_m}(m_\infty - m)$	insulation	$m_{initial} = m_\infty^0$	τ_m: $Table$ 3.2 m_∞^0: $Table$ 3.2
n	$\frac{\partial n}{\partial t} = \frac{1}{\tau_n}(n_\infty - n)$	insulation	$n_{initial} = n_\infty^0$	τ_n: $Table$ 3.2 n_∞^0: $Table$ 3.2

3.2.3 Internal and MREIT Current Sources

The model was stimulated by an MREIT-like current sequence, which was applied to pairs of injection ports. Only two electrodes were used (electrodes 1 and 5) for the current injection since the model was symmetric. The current waveform is shown in figure 3.2. It consisted of two Gaussian pulses (A and B) separated by 6.34 ms and each had a FWHM of 1.6 ms. Gaussian waveforms were used to improve the finite element model convergence speeds. The internal source i_{source} was specified as:

$$i_{source}(r,t) = W(r)i_{spike}(t), \text{ such that } W(r)i_{spike} = \begin{cases} 1 & r < 35\mu m \\ 0 & r > 35\mu m \end{cases}, \quad (3.8)$$

where $i_{spike}(t)$ was the time course of the internal source, which had a Gaussian form with a FWHM of 1.9 ms. The internal source was at the center of the model and propagated throughout the tissue. The membrane conductivity and voltages inside the source are shown in figure 3.2. A different external current amplitude and current density distribution in active tissue may have a different effect on tissue spiking.

A typical spin-echo-based MREIT pulse sequence is shown in figure 3.3. The total pulses delivered to the sample in one scan were calculated as Number of Slices (NS) x Number of Average (NAV) x Phase Encoding (PE). Pulses A/A' and B/B' in figure 3.3 corresponded to pulses A and B in figure 3.2. The two Gaussian pulses in the internal source were applied before and after the MR 180^o RF pulse, respectively. The difference between A, B and A', B' was the direction of the current injection. In both cases, the current injection reversed after the 180^o RF pulse in order to eliminate the system noise and double the current induced signal as mentioned in chapter 1, since phase data are accumulated during actual MREIT. The simulated B_z values were integrated and then

divided by TE = 18.3 ms, which was used in real MREIT experiment (R. J. Sadleir et al., 2017).

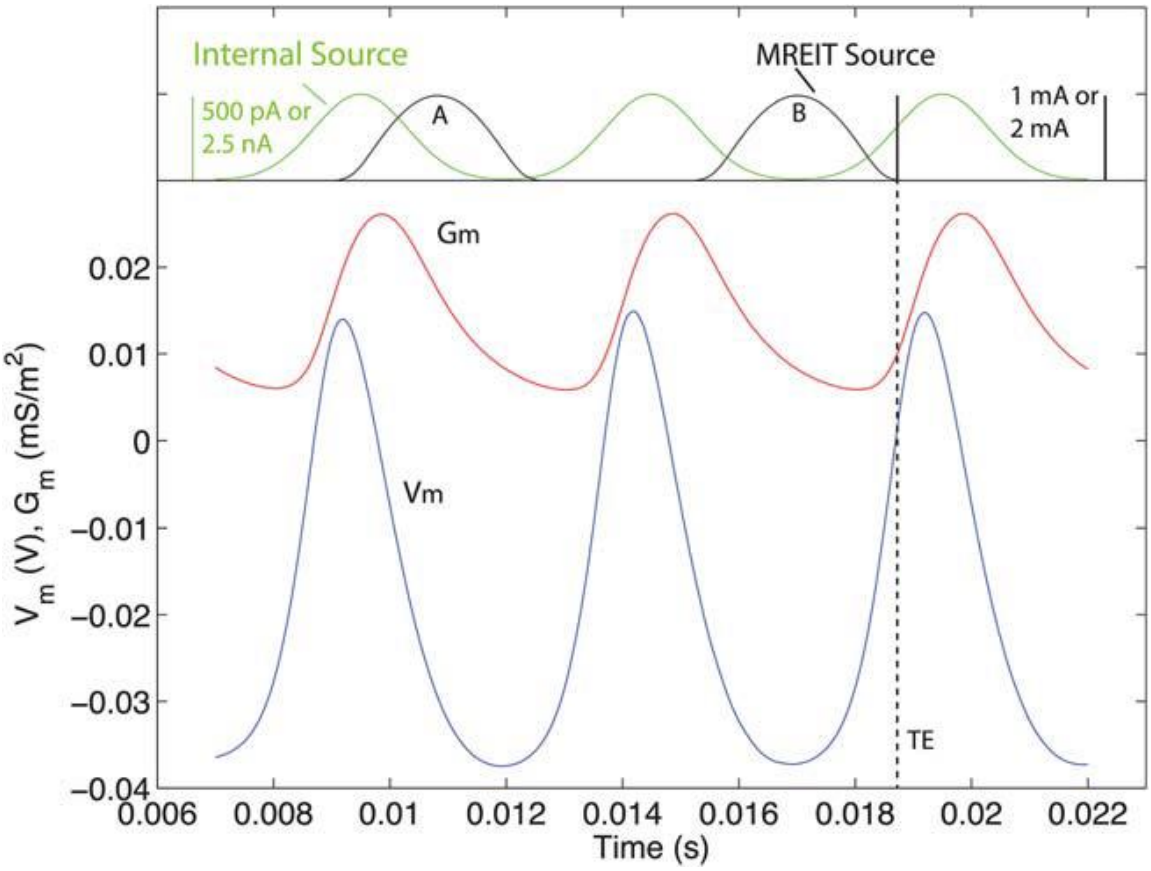

Figure 3.2 External current injection waveform (black), internal source waveform (green), membrane conductivity (red) and membrane voltage (blue) at the center of the source are shown here. The scale for the current source is shown at the top, and the scale for conductivity and voltage is shown on the left. TE was marked by the black dotted line. This figure is from Sadleir et al. (R. J. Sadleir et al., 2019).

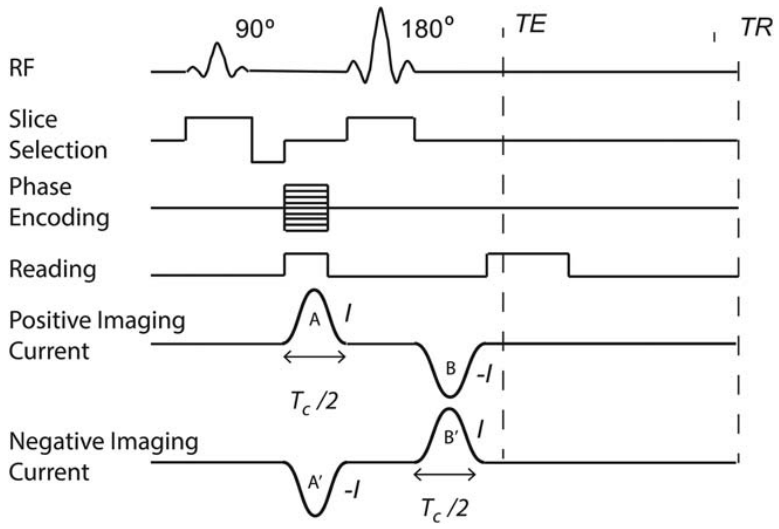

Figure 3.3 Spin-echo-based MREIT pulse sequence. The external current injections were applied before and after the 180° RF pulse with reversed injection direction. The TE and TR were marked with dotted lines. Typical MREIT images require two scans with reversed current injection directions as indicated by "Positive Imaging Current" and "Negative Imaging Current". This figure is from Sadleir et al. (R. J. Sadleir et al., 2019).

3.2.4 Meshing and Solution of Finite Element Models

The finite element mesh contained 268,256-tetrahedral elements, with a dense distribution in the AAG. All the differential equations were fully coupled and solved simultaneously as a function of time. The voltage distribution inside the chamber had a time step of 0.1ms and a time period between 0 and 28.6 ms. The Backward Differentiation Formula (BDF) time-dependent solver with a multi-frontal massively parallel sparse direct solver (MUMPS) was used to solve the problem. COMSOL LiveLink for MATLAB (MathWorks, Natick, MA) was used for extracting voltage and current density data over the entire domain at each time point. A Fourier transform

formulation of the Biot-Savart Law (Minhas et al., 2011) was used to compute the B_z values within the model. Each solution took about 50 mins.

3.2.5 Conversion of Model Current Density Data to MR Phase Images

The model was covered by a stencil with the same dimensions. The resolution of the stencil was 128 x 128, and the voxel size was 70 x 70 x 500 μm. Three slices were created and centered on the electrode plane. The J_x and J_y values were extracted from the model and put in the stencil with the COMSOL command "mphinterp". Each voxel had 1331 points (11 x 11 x 11 grid). B_z data were converted from J_x and J_y, then averaged over each voxel to generate the MR B_z image.

3.2.6 Model Settings

Nineteen simulations were solved by using the following conditions:

Table 3.4

Simulation conditions.

Model properties	External current (mA)	Internal current (pA)
PASSIVE	1, 2, 5	None
FULL	1, 2, 5	500, 1000, 1500, 2500
NOMREIT	None	500, 1000, 1500, 2500

The PASSIVE B_z data were subtracted from the FULL B_z data in order to obtain the differential B_z data (ΔB_z). The NOMREIT B_z data were compared with the ΔB_z data for the purpose of observing the signals caused by the current injection.

3.2.7 Reconstruction of Laplacian of ΔB_z

Laplacians of ΔB_z data (FULL-PASSIVE) were computed from the noise treated individual B_z data (Noise with an SD of 0.1 pT), in order to highlight the contribution of the noise to the image reconstruction.

3.3 Results

3.3.1 Demonstration of MREIT Contrast Mechanism

No current

When no external current was applied, there was still a phase accumulation caused by the internal source (Cassarà et al., 2008; Hagberg, Bianciardi, Brainovich, Cassarà, & Maraviglia, 2008; Hagberg, Bianciardi, & Maraviglia, 2006; Luo & Gao, 2010; Luo et al., 2011). The maximum accumulated B_z values over the nominal TE were around 21 pT/0.004^o for 500-pA internal source amplitude. Figure 3.4A shows the B_z distributions in a central slice (500-μm thick). The maximal B_z values increased to 107 pT/0.025^o when increased source strength 5 times (Figure 3.4D). The histograms of B_z values within the tissue for the internal source of 500 pA with the external current injection of 2.5 nA are shown in figure 3.5A, D, respectively.

Effect of Increasing Internal Source Strength

The maximal (absolute) ΔB_z values for the 500 pA internal source with 1-mA external current injection were about 0.12 nT/ 0.03^o. Due to current conservation requirements and counterflows in the bath surrounding the tissue region, the current paths deviated both inside and outside the tissue (Hagberg et al., 2006; Konn et al., 2003). The histograms of ΔB_z data are shown in figure 3.5. We can see that the maximal ΔB_z values

slightly increased to 0.14 nT/0.032^{o} when internal source increased five times with 1-mA external current injection.

Effect of Increasing External Current

Accumulated phase and ΔB_z almost doubled when the external current increased to 2 mA, as shown in figure 3.4 C and F and figure 3.5C and F. The maximal ΔB_z value increased from 0.12 nT to 0.27 nT/0.06^{o} for the 500-pA internal source and 2-mA external current injection. The non-linear increment was due to the additional conductivity changes throughout the active tissue, which was caused by the large external current. The maximal ΔB_z values for 2.5-pA internal source and 2-mA external current injection was around 0.37 nT/0.08^{o}.

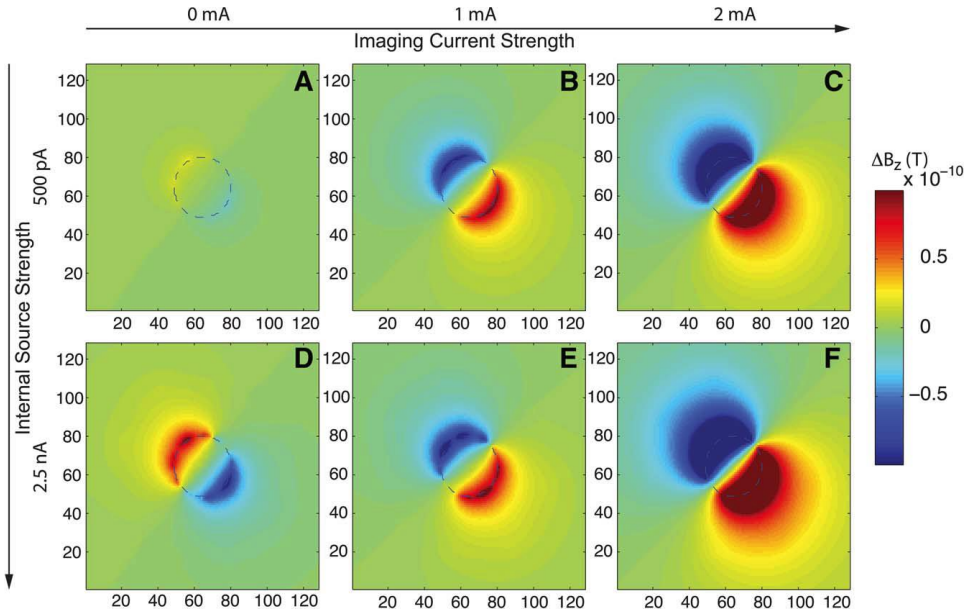

Figure 3.4 The ΔB_z distributions in the center slice of the electrode plane. It includes the results for two internal sources (500 pA and 2.5 nA) and three external sources (0, 1 and 2 mA). The figure presents the ΔB_z distribution for A, 500-pA internal source with no external current, B, 500-pA internal source with 1-mA external current. C, 500-pA internal source with 2-mA external current. D, 2.5-nA internal source with no external current. E, 2.5-nA internal source with 1-mA external source. F, 2.5-nA internal source with 2-mA external source. This figure is from Sadleir et al. (R. J. Sadleir et al., 2019).

3.3.2 Comparison with Candidate Noise Levels

The histograms of ΔB_z values in the active tissue within all 3 slices centered on the electrode plane is shown in figure 3.5. These was summarized from the date shown in figure 3.4, for 500 pA and 2.5 nA internal source with 1 mA and 2 mA external current injection. The edges of each plot are the largest detectable ΔB_z values. Three different voxel sizes were used to estimate the Nosie levels, as indicated by blue vertical lines in

figure 3.5. They were calculated using typical SNR of comparable experiments with the usage of 800-MHz MRI scanner at the Magnetic Resonance Research Center (MRRC) at ASU. Since magnitude of SNR affects phase noise (R. Sadleir et al., 2005), TR and TE values can change the noise levels. The histogram bins exceeding the blue noise lines are the detectable ΔB_z values. The numbers above each line are the average numbers (NAV) needed to achieve the 0.1 nT noise level using the same scan parameters and voxels of 70 x 70 x 500 μm^3 (black), 140 x 140 x 500 μm^3 (red), and 280 x 280 x 500 μm^3 (green). For the 2-mA external current injection and 8 averages, the ΔB_z distributions should be detectable at the 70 x 70 x 500 μm^3 resolution if the two simulated spikes are coherent.

3.3.3 Laplacians of the ΔB_z Data

Figure 3.6 shows the Laplacians of the ΔB_z data using the data shown in Figure 3.5 with noise addition. Laplacian data show changes at the boundaries of the tissue (conductivity discontinuity) and changes around the internal source.

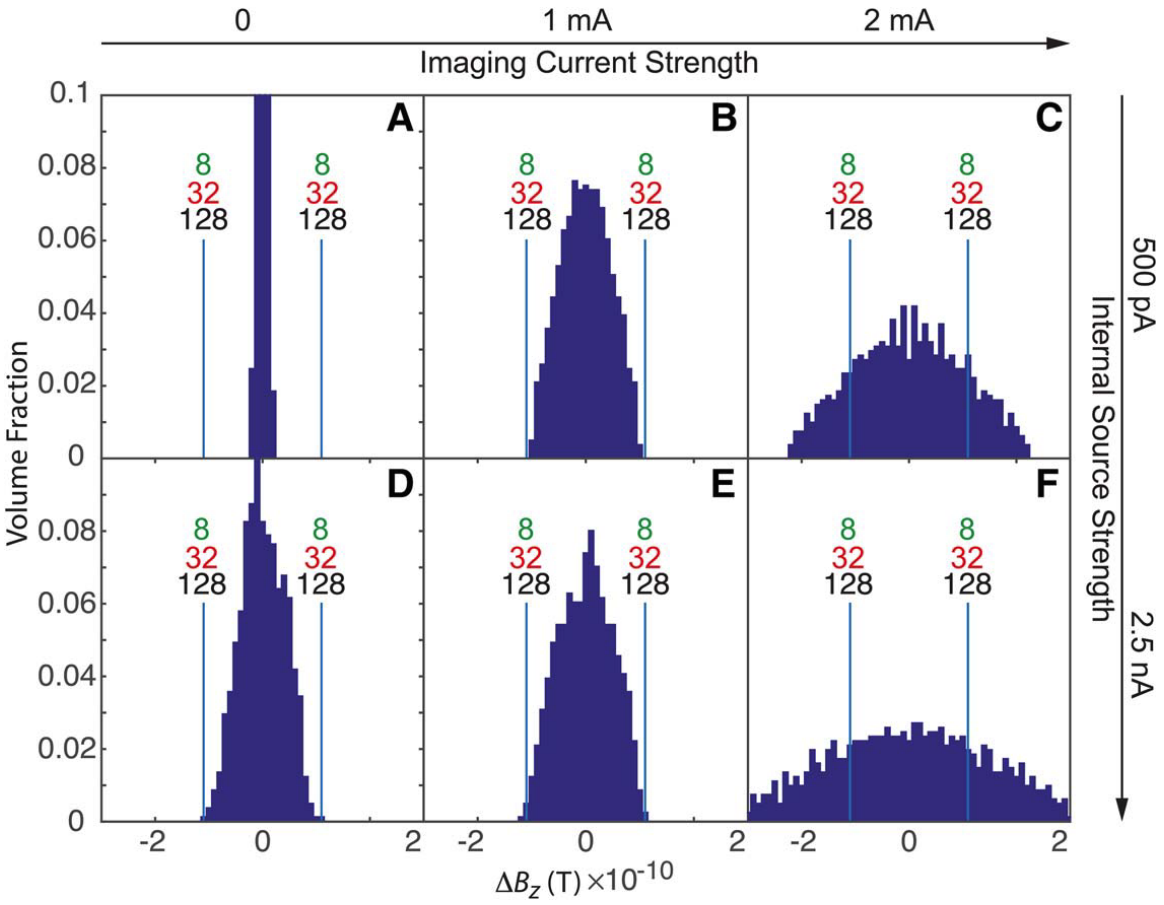

Figure 3.5 Histograms of ΔB_z distributions in tissue domain. All three modeled slices were used to obtain the data. The ratios of the values to the total active tissue volume are plotted. Blue lines indicate the baseline noise level of about 0.1 nT. The numbers above the lines are the averages required to reach this noise level with voxel size of 70 x 70 x 500 μm^3 (black), 140 x 140 x 500 μm^3 (red), and 280 x 280 x 500 μm^3 (green). This figure is from Sadleir et al. (R. J. Sadleir et al., 2019).

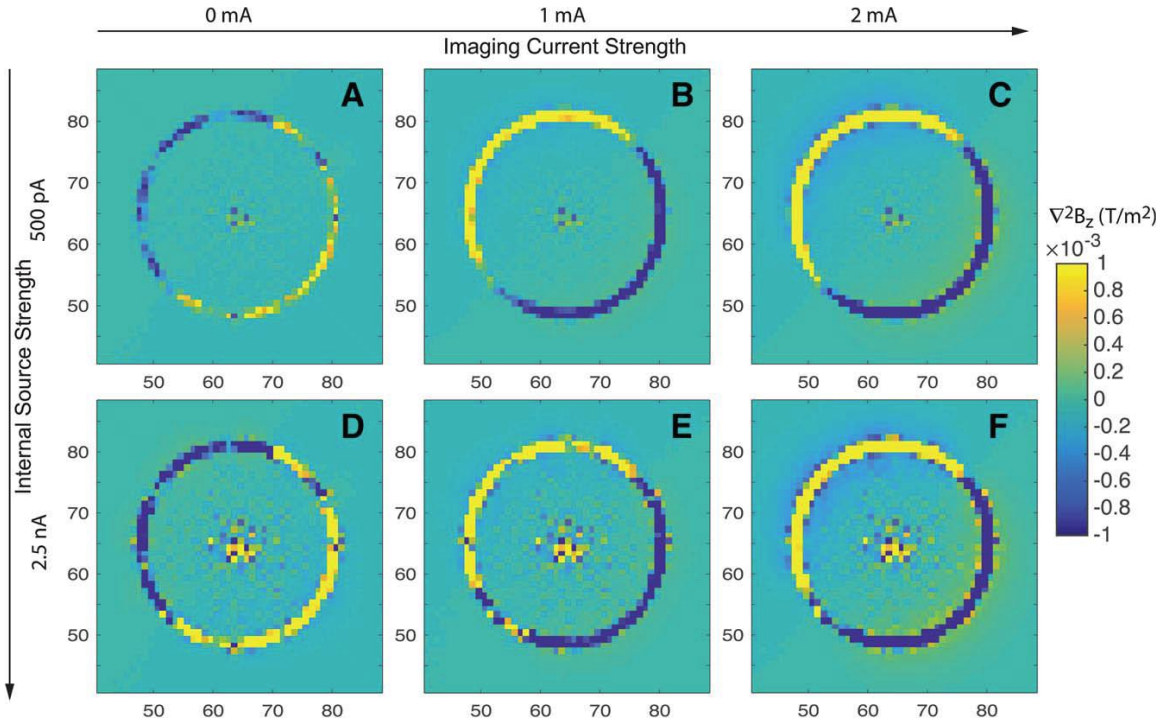

Figure 3.6 The Laplacians of the ΔB_z data in figure 3.5. Only the data from the active tissue are highlighted. This figure is from Sadleir et al. (R. J. Sadleir et al., 2019).

3.4 Discussion

3.4.1 Capability of MREIT for Neural Imaging

The results demonstrate that the external current injection can amplify the phase changes caused by neural activity, which makes MREIT a potential technique for neural imaging. Large ΔB_z values were observed when an external current was injected to the models with an internal source, because the intrinsic neural activity changes the membrane conductance and thus influence the externally applied current paths. The larger the external current used, the greater the effect generated. The internal source amplitude produced a tiny effect on ΔB_z values. The maximal ΔB_z values only increased

by about 16% when the internal source strength increased from 500 to 2500 pA with 1-mA external current. Increasing the external current injection clearly increased the ΔB_z values. The ΔB_z values increased by about 40% when using 2-mA external current injection with internal source strength of 2500-pA. The difference saturated at around 1500 pA. The explanation is that MREIT is sensitive to membrane conductivity changes instead of the intrinsic current flow effects. Conductivity contrast is a more robust method than neural current along as it is a scalar. MREIT has the potential to image bigger structures such as the brain, since the signal size is affected by the external current amplitude. High field MRI could also benefit the MREIT, as a better SNR and a smaller voxel size can be obtained (Chauhan, Vidya Shankar, Ashok Kumar, Kodibagkar, & Sadleir, 2018; R. J. Sadleir et al., 2017).

3.4.2 Inspiration for fMREIT Experimental Analysis

Calculation of the Laplacian of B_z or phase has a less diffuse signature than B_z or phase alone. It clarifies activity locations and separates them from B_z information. Thus, statistical analysis on Laplacian of B_z or phase images may provide a better method of analyzing fMREIT experiments.

The feasibility of fMREIT could be underrated in this study because a single internal source was applied. Multiple internal sources exist in most tissues, which causes more conductivity difference. Thus, more phase changes are expected in the experiment. The results of the paper indicate that it should be possible to detect effects of membrane conductance changes using resolutions and current intensities similar to those used in the model.

3.5 Conclusions

The feasibility of fMREIT was evaluated with an active bidomain model plus Hodgkin-Huxley equations. The internal source has the amplitudes similar to the intrinsic spontaneous neural activity found in neural current MRI models. It was demonstrated that the external current injection over 1 mA made the neural activity detectable at moderate MR image resolution. Future tests of this technique in models and experiments are needed to better illuminate the potential for direct detection of neural activity during neural stimulation with fMREIT.

4 EVALUATION OF MAGNETOHYDRODYNAMIC (MHD) EFFECTS IN MREIT

The following work was published in Magnetic Resonance in Medicine (Minhas, Chauhan, Fu, & Sadleir, 2018)

4.1 Introduction

As introduced in the previous chapters, MREIT can be used to map tissue conductivity at low frequency. MREIT has been developed using phantom studies, animal models of disease (Jeon et al., 2009; Kim et al., 2008; Kwon, Woo, Yoon, & Seo, 2002; Minhas et al., 2008; Muftuler, Hamamura, Birgul, & Nalcioglu, 2006; C. Park, Lee, Kwon, & Woo, 2006; R. Sadleir et al., 2005), in the human lower leg and knee (Kim et al., 2009), and finally to current flow and conductivity in the human brain (Chauhan, Indahlastari, et al., 2018; Kasinadhuni et al., 2017). Studies aimed at clinical application were primarily performed using 3 T MRI machines. Meanwhile, fMREIT has been demonstrated with AAG by using an 11.75 T MR system (R. J. Sadleir et al., 2017).

In initial MREIT experiments using an 800 MHz system, clear phase distortion were found during tests on a saline-filled sample chamber. The initial hypothesis was that Lorentz forces caused fluid motion during current injection since all materials in the chamber were at rest. This phenomenon has been observed to image contrasts in other contexts (Balasubramanian, Mulkern, Wells, Sundaram, & Orbach, 2015). Four phantoms with different material viscosities were made to study the possible magnetohydrodynamic (MHD) phenomenon. Studies performed using these phantoms were compared to simulated MHD effects calculated using finite element models. This

work may also be useful in helping to investigate the artifacts and safety in ultrahigh field clinical scanners (Frauenrath et al., 2012).

4.2 Methods

The four cylindrical phantoms used for the experiment are shown in figure 4.3A. all of them are 7.2 mm diameter and 10 mm height, labeled as I-IV. Phantom I was filled with gelatin (3 g/L NaCl and 20 g/L agarose), Phantom II was filled with ASW (artificial sea water). Phantom III contained two materials, with ASW in the center of the chamber, surrounded with gelatin. Phantom IV had the same geometry as phantom III, but it had gelatin in the center, surrounded by ASW. Four 2-mm-diameter surface electrodes (HUREV, South Korea) were attached on the wall of each phantom to inject current. The conductivities of the ASW and gel were 4 and 1 S/m at 100 Hz, measured with an impedance analyzer (HP4192ALF, Hewlett Packard [Agilent], Palo Alto, CA).

The experiments were performed using an 800 MHz Varian vertical bore magnet at the MRRC at ASU. A customized MR imaging probe (12 mm internal bore; Doty Scientific, Columbia, SC) was used for all image acquisitions. The experimental setup is shown in figure 4.1B. A spin-echo-based MREIT pulse sequence was used for imaging. The current injections were synchronized with the MR pulse sequence, injected before and after the 180^{o} RF pulse with opposite polarities injected in each segment to prevent cancelation. Imaging currents were injected either 'horizontally' (x-direction) or 'vertically' (y-direction) in the transverse plane. A TDT constant current source (IZ2H - 16, Tucker Davis Technologies, Alachua, FL) was used for current injection, at ±500 μA amplitudes ($I^{\pm}$) and a total 18 ms injection time (T_c). The durations of the positive and

negative polarity currents were 8.175 ms (A) and 7.886 ms (B), respectively. Magnetic flux density (B_z) data were calculated by complex dividing the positive-first current injection data with negative current injection data. The imaging parameters used were TR/TE = 1000/20 ms, FOV = 12 mm^2, slice thickness = 1 mm (no gap), averages = 4, matrix size = 128 × 128, number of slices = 1, and scan duration = 512 s.

To study the effect of readout and phase encoding direction on phase images, we obtained images with different combinations of current injection directions and phase encoding directions.

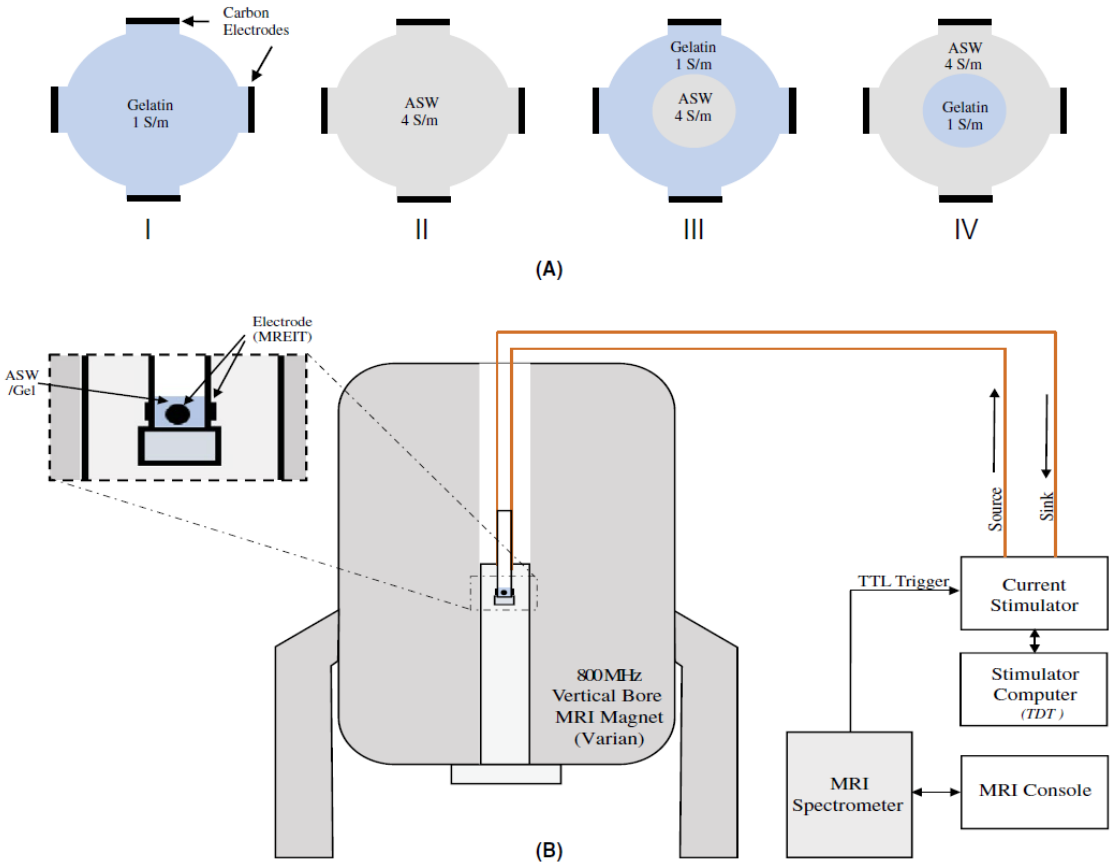

Figure 4.1 MREIT experiment setup. (A) Axial views of the 4 phantoms used in experiments. I: gelatin. II: ASW. III: ASW in the center and gelatin surrounded. IV: Gelatin in the center and ASW surrounded. (B) Schematic diagram of the MREIT experiment. Imaging was performed at 18.8T (800 MHz).

4.3 Results

Experimental phase images obtained with vertical and horizontal current injections at 18.8 T are shown in figure 4.2. Row 1 to 4 correspond to results for phantoms I to IV. Phase encoding gradients were applied along the x-direction and readout gradients were applied along the y-direction. Experimental results (column (A) in

figure 4.2) in the gel phantom showed the expected MREIT phase images for both horizontal and vertical current injection conditions. However, the experimental phase image for ASW case had higher phase amplitudes, and apparently switched polarity at the bottom for vertical current injection condition case. For horizontal current injection conditions, the experimental phase image for ASW was almost uniformly distributed and has a large positive phase accumulation. For phantom III (ASW at the center with surrounding gel), the phase was split in the ASW region and appeared normal in gel regions. Case IV images presented similar results: normal phase in the center cylinder (gel) and split phase in the outer annulus (ASW).

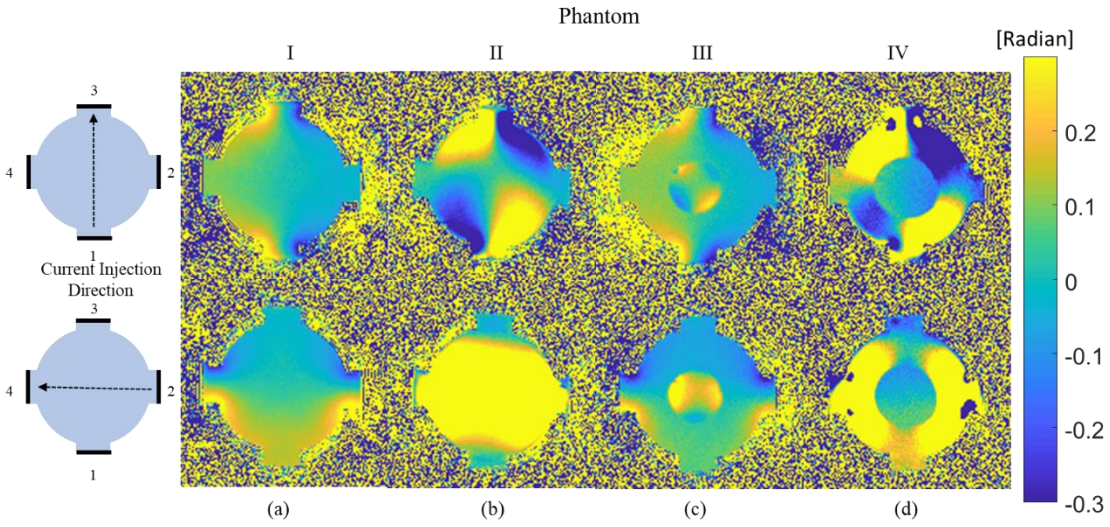

Figure 4.2 MREIT phase images for four phantoms at 18.8 T. Images in the top row were applied with vertical current injection, meanwhile, images in the bottom row were applied with horizontal current injection. (a) Phase images for phantom I, (b) phantom II, (c) phantom III, and (d) phantom IV.

The phase images obtained with different phase encoding directions and current injection directions are shown in figure 4.3 for phantom II (ASW only). The same characteristic patterns were obtained, as long as the relationship between current flow direction relative to phase encoding direction was maintained. These images clearly show that the effect is related to the combination of high magnetic field, electrical current flow, and the presence of gradient fields.

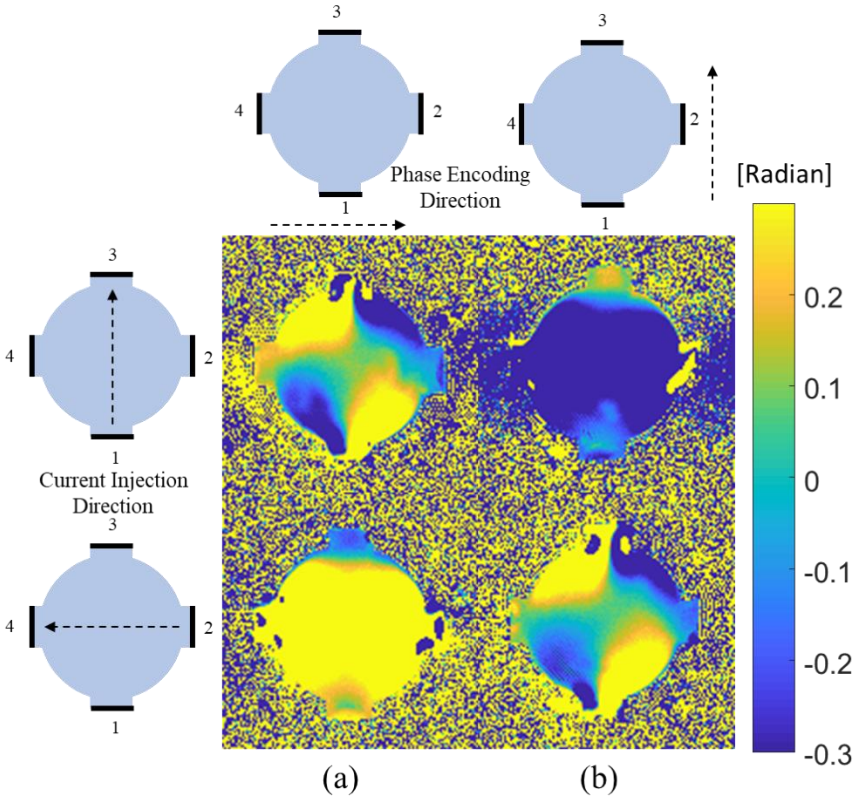

Figure 4.3 MREIT phase images found in phantom II (ASW) using vertical (top row) or horizontal (bottom row) current injections, as phase encoding direction was changed from (a) horizontal to (b) vertical.

4.4 Discussion and Conclusions

These studies demonstrate that motions in materials with viscosities close to ASW can be caused by current injection using high field MREIT. The motion is dependent on the main magnetic field strength, the shape of the external current waveform, and the shape, size, and viscosity distribution in the medium. MREIT phase images can be distorted by this motion, and this motion induced phase dominated MREIT phase under high field conditions. The directions of phase and readout gradient relative to the current injection directions also affected the spatial distribution of the distorted phase. This was clearly observed from the difference between vertical and horizontal current injection induced phase distribution.

These experimental results were compared with the simulation results in Minhas et al. (Minhas et al., 2018). These comparisons are shown in figure 4.4 and 4.5. The simulation results present only velocity induced phase images and do not reflect the current flow related portions. Experimental images shown in figures 4.4(A) and 4.5(A) were closest to the simulated results shown in figure 4.4(C) and 4.5(C). The velocity induced phase changes found in the model were smaller in gelatin than in ASW, as expected.

No MHD effects had been reported from previous successful MREIT studies (T. I. Oh et al., 2011; R. J. Sadleir et al., 2017). This could have been because the phantom size was larger, and the magnetic field strength was smaller than in the experiment reported in our study. However, in recent MREIT experiments performed in a preclinical 7 T scanner (Bruker Biospin, Barrow Neurological Institute, Phoenix, AZ) using a

similar-sized phantom filled with ASW, motion induced phase patterns were also observed. More studies are needed to explore the MHD effects in MREIT. The correlations between phantom size and magnetic field strength are of interest. These studies will be useful in deciding optimal imaging parameters and pulse sequence designs in MREIT experiments. This work could be used to minimize MHD effects in fMREIT studies performed at ultrahigh field and illustrates that MHD effects may be mitigated by increasing the viscosity of the solution.

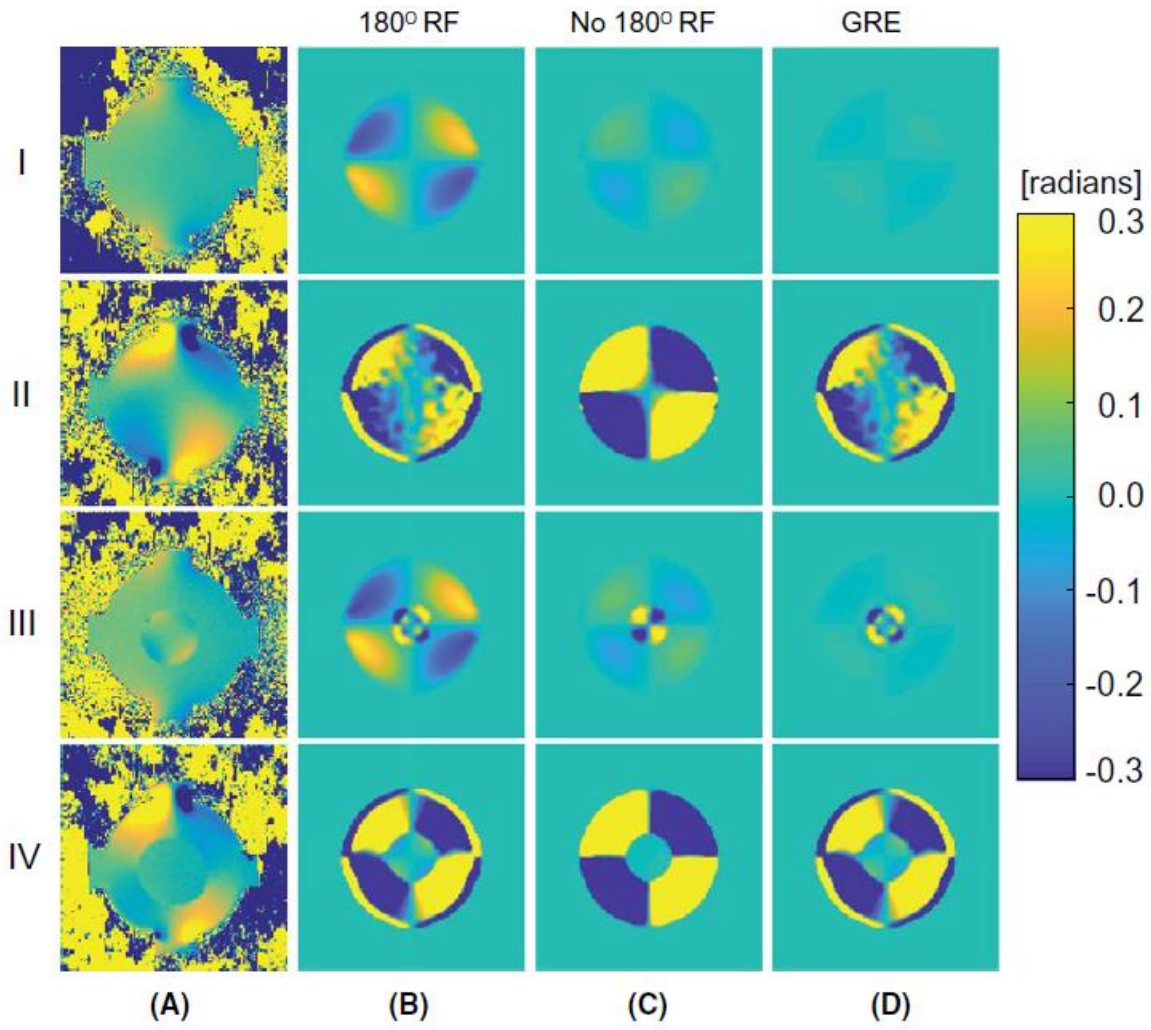

Figure 4.4 Comparison between simulated and experimental MREIT phase images with vertical current injection at 18.8 T. (A) MREIT experimental results. (B) Simulated results for spin echo pulse sequence with and (C) without a 180° RF pulse effect. (D) Simulated results for GRE sequence. Row I-IV are corresponded to model or phantom I-IV. This figure is from Minhas et al. (Minhas et al., 2018).

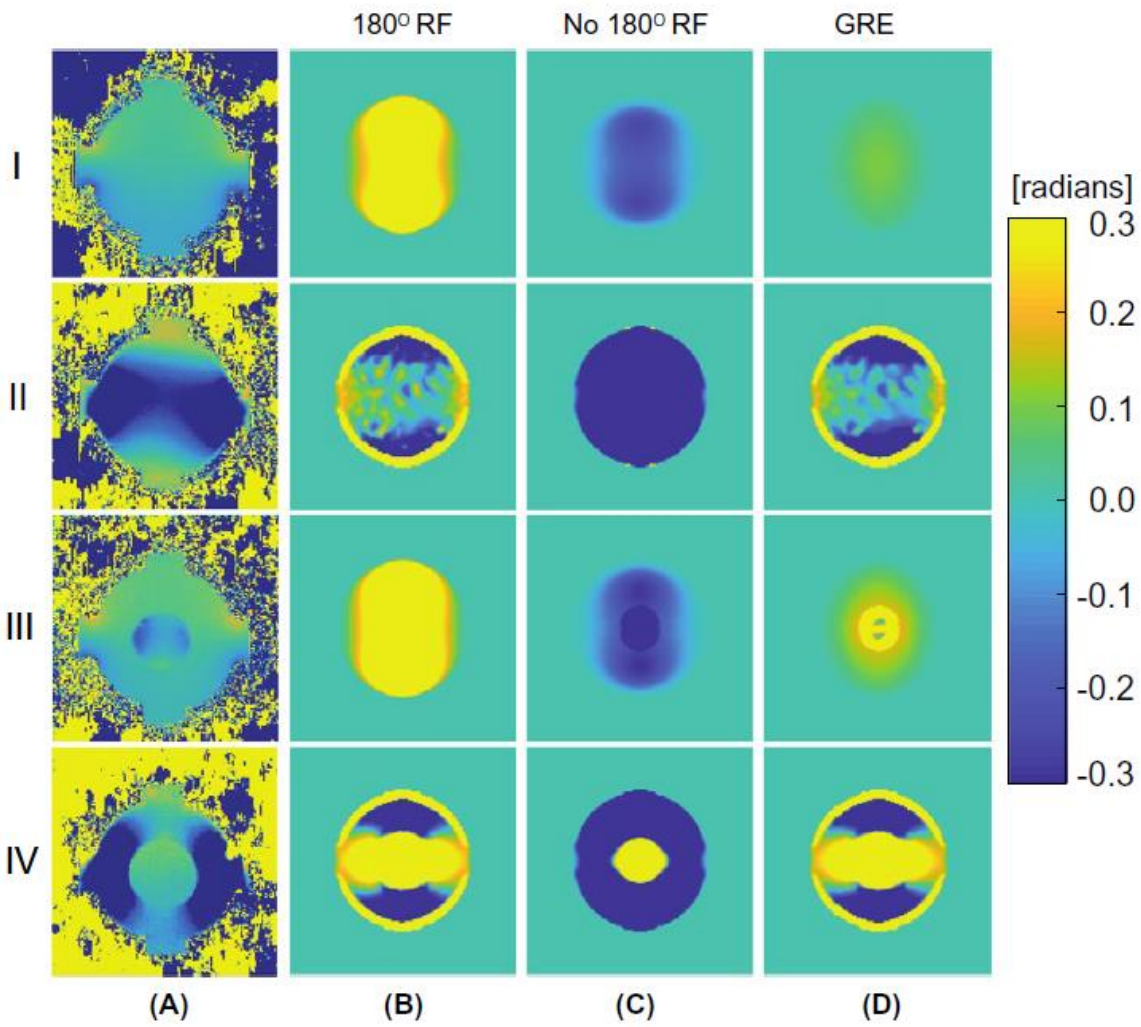

Figure 4.5 Comparison between simulated and experimental MREIT phase images with horizontal current injection at 18.8 T. (A) MREIT experimental results. (B) Simulated results for spin echo pulse sequence with and (C) without a 180° RF pulse effect. (D) Simulated results for GRE sequence. Row I-IV are corresponded to model or phantom I-IV. This figure is from Minhas et al. (Minhas et al., 2018).

5 FUNCTIONAL MREIT EXPERIMENT FOR AAG

5.1 Introduction

In this experiment, fMREIT was used to detect changes in the neural activity states of the AAG. During neural spiking, conductivities of active neural tissue membranes change, affecting the passage of imaging current paths near this tissue, principally affecting MR phase images. Neural activity may, therefore, be detected directly in fMREIT by evaluating regions of increased phase variability (R. J. Sadleir et al., 2017). Early testing in fMREIT has involved in vitro monitoring of changes in isolated neural preparations (R. J. Sadleir et al., 2017). Using tissue from invertebrate and well-characterized animals provides a convenient way to test fMREIT validity.

The ganglia used in the study were divided into control and treatment groups, and treated with ASW or KCl solutions respectively to modulate their neural activity. MR phase data were gathered and compared between the two groups and MEA recordings were used to monitor the neural activity in each sample during the experiment. Statistical analysis of the images were then used to examine if there were significant differences between control and treatment groups.

5.2 Methods

5.2.1 Test Chamber

The main part of the test chamber was a polylactic acid (PLA) cylinder that had an external diameter of 11.5 mm (internal diameter 7.6 mm) and a length of 120 mm (figure 5.1). There were four 2 mm diameter ports spaced at 90° intervals in a single

plane near the base of the chamber. Carbon fiber electrodes (Hurev Co. Ltd, Republic of Korea) were used to cover the holes. The bottom part of the chamber had a Microelectrode array (MEA) mounted inside, as shown in figure 5.1.

5.2.2 Animal Preparation

Small juvenile (<100 g) Aplysia were ordered from the NIH/University of Miami National Resource for Aplysia Facility. The $MgCl_2$ solution (77 g/L of $MgCl_2$ and 3.6 g/L of HEPES buffer) was used for anesthetizing the animals. The abdominal ganglion was then removed after the body was fully relaxed and placed into the artificial seawater (ASW) for storing.

5.2.3 Control and Treatment Solution

The ASW solution used as a control solution in experiments, was the native medium of the animals. It was composed of deionized water and sea salt (Instant Ocean, Spectrum Brands, Blacksburg, VA, USA). The overall salinity was adjusted to 30 ppt, and the environmental temperature was set to 16 C^o. The initial molarity of the potassium in the ASW was 8.24 mM (Atkinson & Bingman, 1997). A high-concentration KCl solution was used for the treatment group. It was made by adding 90 g KCl to a 400-ml volume of ASW, thus the concentration of the potassium in the KCl solution was about 3 M. The KCl solution was used as a treatment to stop the neural activity in the treatment group, as reported by Fu et al. (Fu et al., 2018). To reduce the magnetohydrodynamic effect as reported by Minhas et al. (Minhas et al., 2018), 0.2 g of Methylcellulose powder (SIGMA) was added into a 20 ml ASW solution to increase viscosity of media within the sample chamber. One milliliter of Gadoteridol (Gd, Prohance, Bracco Diagnostics Inc.,

Monroe Township, NJ) was added into each 200 ml of ASW solution used in imaging to increase the SNR. The final Gd concentration in ASW was 2.5 mM.

5.2.4 Microelectrode Array (MEA) Recording

A Multichannel Systems (Reutlingen, Germany) Flex MEA36 microelectrode array (MEA) was used to record the ganglion neural activity. The MEA was fixed to the chamber base with a double-sided tape, and the slot was sealed with silicone sealant. Cellulose nitrate coating was applied to the surface of the MEA to ensure a good contact between AAG and MEA (Egert & Meyer, 2005). Nitrocellulose stock solution was made by dissolving a 25 mg (5 cm^2) nitrocellulose transfer membrane (protran® BA83/85) in 2 ml of 100% methanol. A working solution was made by diluting the stock solution with methanol in a ratio of 1:10. Five microliters of the working solution was dropped on the MEA surface and allowed to dry for approximately 3 mins. The AAG was then gently pushed down onto the MEA with tweezers. The setup was similar to those mentioned in chapter 2, and is shown in figure 2.1. The tail of the MEA36 array was connected to a custom Multichannel Systems preamplifier placed in the base of the custom imaging probe. A cable then carried the preamplified signals from the MEA to the Multichannel Systems amplifier and digitizer. MC_Rack software (MultiChannel Systems) was used to display and record the neural activity and to detect and count spikes. Each recording lasted 9 mins. Neural spikes were detected using the spike sorting function built into the MC_Rack software. A 500 ms sample of the background noise at the beginning of each data trace was used to calculate the noise standard deviation. A spike was defined as having an amplitude five times higher than the noise standard deviation (5σ). For each

animal, spike counts obtained from all channels over 1 min were summed and represented as the spike number at each time point.

Since the recorded ganglion activity levels were affected by the connective tissue thickness differences, positions of the ganglia relative to the MEA electrodes, electrode contact quality, and individual anatomical and baseline differences between the animals as mentioned in chapter 2, spike numbers were normalized to reveal the typical behavior changes. Spike counts for all ganglia were normalized to an initial value of 100. The normalized spike count data from all recordable flexMEA channels was computed over each 1 min recording. The mean and SD of the normalized spike count data at each time point for all the ganglia in each group were calculated.

5.2.5 Imaging Specifications and Settings

All experiments were conducted using a VNMRS 800 MHz spectrometer (Varian) with a 12 mm MRI probe (Doty Scientific, Columbia, SC) at the MRRC, ASU. A spin-echo-based sequence was used in the fMREIT experiments. The imaging parameters used in all experiments were TR/TE = 350/20 ms, FOV = 14 × 14 mm^2, slice thickness = 1 mm, number of averages NEX = 12, matrix size = 256 × 256, and number of slices = 1. The total scan time for obtaining one image was 750 s. External currents I_1 and I_2 were injected in the vertical direction before and after the 180^o RF pulse as shown in figure 5.2. The temperature inside the cryogenically cooled magnet bore was 20 °C.

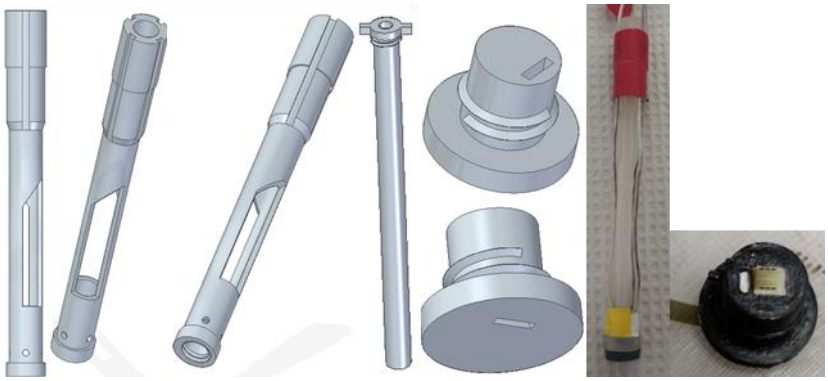

Figure 5.1 Schematic diagram of PLA sample chamber.

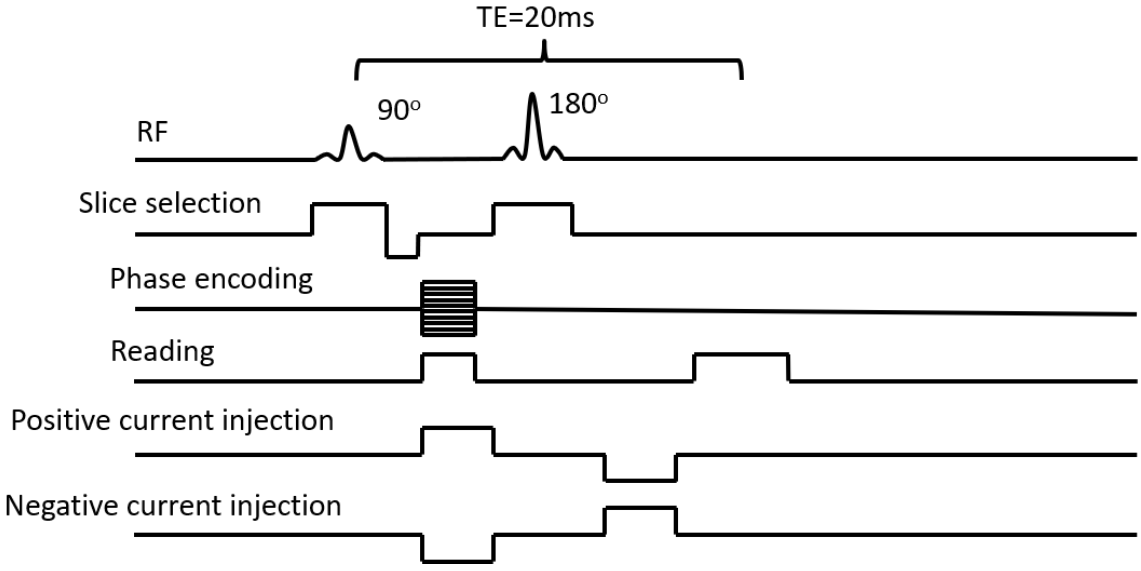

Figure 5.2 Spin-echo-based fMREIT pulse sequences, showing current injections synchronized with sequence.

5.2.6 MREIT Current Application

A current source system from Tucker-Davis Technologies (RZ5D BioAmp Processor, IZ2 Stimulator) was used for fMREIT current injections. The current amplitude used was 1 mA, and the total current injection time (Tc) was 16ms. After

acquiring the first magnetic flux density data (Φ^+) using the positive current injection (I^+), a negative current (I^-), was injected using the same amplitude and pulse width to obtain a second phase image (Φ^-) through the same pair of electrodes.

5.2.7 MREIT Experimental Sequence

The fMREIT imaging was interleaved with 5-minute long MEA recordings. Eleven Aplysia were used in each treatment or control group. For each animal, a total of 10 scans were acquired. Five of them were obtained before control or treatment solution administration, and five after. Scans started with no current injection (NC) imaging, followed by four scans with two pairs of vertical current injections (from top to bottom, bottom to top, then repeated). The same procedure was repeated after the solution administration and wait time. The current injection directions of the four sequential scans were reversed each time (top to bottom and then bottom to top), and two phase images (Φ_1, Φ_2) were generated based on the subtracted image pair data. The schematic description is shown in figure 5.3. The sample chamber was filled with 400 µl ASW solution at the beginning of the experiment. A 20 µl ASW/KCl solution was added as a control/treatment solution after the sixth scan via the delivery system. The KCl solution took effect after about two minutes. After the KCl addition, the KCl concentration in the chamber increased to 158 mM. In the interval between solution administration and acquisition of the second set of five images, several additional scans were obtained to check the liquid level in the chamber after the solution addition, as well as to check the position of the ganglion. If no movement was observed, the experiment was paused for 30 mins to allow the added solution to fully mix with the original ASW solution, then the

experiment entered the second half. The whole sequence of obtaining phase images for one animal was: Φ_1^{NC}, Φ_1^+, Φ_1^-, Φ_2^+, Φ_2^-, Φ_2^{NC}, Φ_3^+, Φ_3^-, Φ_4^+, Φ_4^-. The corresponding magnitude images were M_1^{NC}, M_1^+, M_1^-, M_2^+, M_2^-, M_2^{NC}, M_3^+, M_3^-, M_4^+, M_4^-.

5.2.8 Experiment Staging

The schematic diagram of the overall experimental setup is shown in figure 5.4. The custom-built MultiChannel Systems MEA pre-amplifier was inserted in the probe first, with its cabling emerging through a 2.5 mm hole at the bottom of the probe. Next, the main sample chamber was dropped down into the magnet bore from its top. The bottom part of the sample chamber, containing the ganglion, was then screwed onto the main chamber. The assembled chamber was then filled with 300 µl ASW. The MEA was connected to the preamp after the chamber had been checking and any bubbles had been removed. The delivery tube was then filled with the control or treatment solution (ASW/KCl) and inserted into the chamber. A MR-safe syringe pump (Harvard Apparatus, Holliston MA) was used to deliver the solution, and this was placed on the gantry near the top of the magnet. Finally, the probe was inserted into the magnet and scanning commenced.

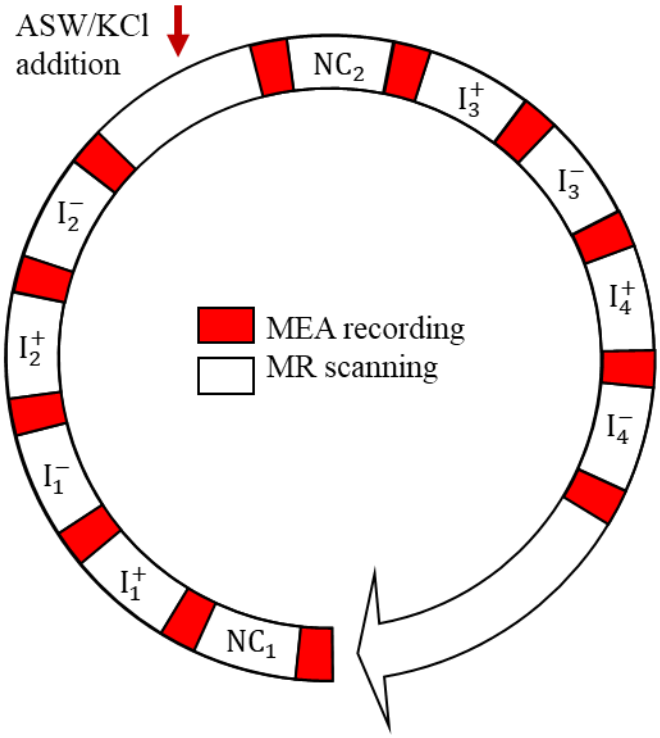

Figure 5.3 Experimental protocol. Red blocks represent MEA recordings and white blocks represent MR scans. NC = no current, I^+ = positive current injection, I^- = negative current injection. The ASW/KCl addition is indicated with the red arrow.

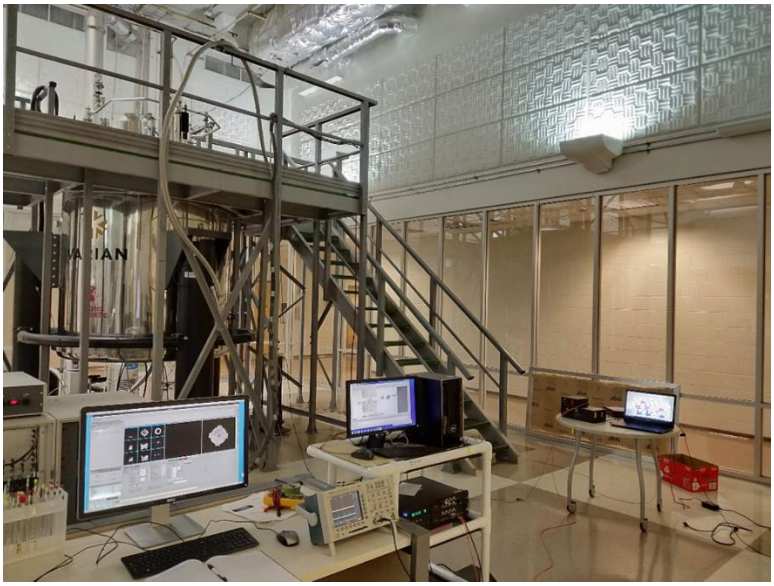

(a)

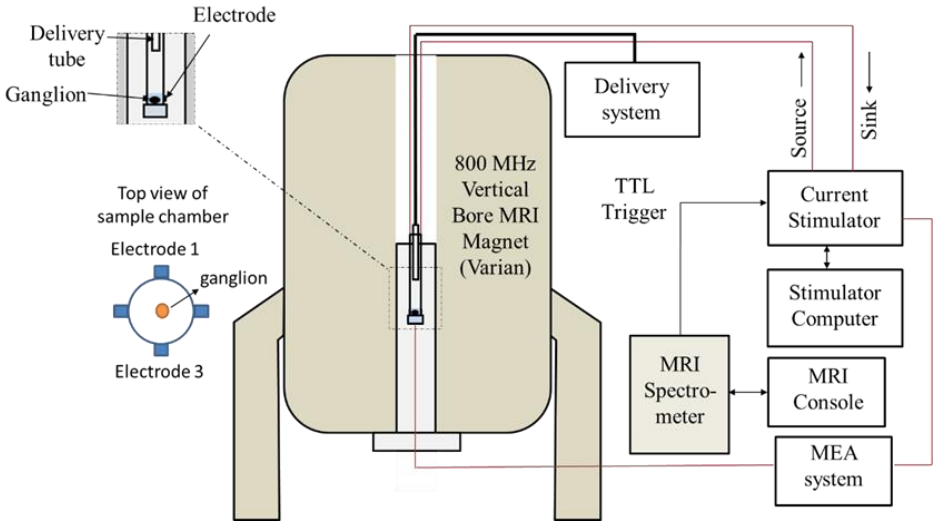

(b)

Figure 5.4 Photo and schematic diagram of experimental setup. (a) Photo of the experiment setup. The MR console, current source, delivery system and MEA system are shown in the figure. (b) Schematic diagram of experimental setup. A cross-sectional schematic view of the sample chamber is shown at bottom left.

5.2.9 MREIT Data Preprocessing

Images were reconstructed using MATLAB (Natick, MA, USA) from raw data. Three kinds of images were reconstructed: no current images (NC), MREIT images, and average (AVG) images.

NC phase image were directly reconstructed from raw data to produce Φ^{NC}. MREIT phase images (Φ^{Bz}) were obtained by complex dividing (subtracting) positive current injected images (I^{+}) by the negative current injected images (I^{-}) (results were divided by two). AVG phase images (Φ^{AVG}) were obtained by adding the positive current injected image (I^{+}) and negative current injected images (I^{-}) (AVG images were also divided by two). All MREIT images were not scaled to produce Bz data, as is normally done in MREIT data processing, to facilitate comparisons with NC data.

5.2.10 Region of Interest Segmentation

The voxels corresponding to the ganglion (AAG) or background (BK) ROIs were segmented manually from the M_1^+ images obtained for each ganglion. There were about 1000 voxels in each ROI. In all cases, the BK ROI was chosen to be to the right of the ganglion within the chamber. Examples of ROIs are shown in figure 5.7.

5.2.11 Expected MREIT and NC Baseline Phase Noise Levels

All measurements were affected by instrument noise. Instrumental noise levels were evaluated using the methods introduced in Sadleir et al. (R. Sadleir et al., 2005). The first method used to evaluate the baseline phase noise in MREIT images is to calculate the standard deviation (SD) in the measured phase data. This is expressed as:

$$\sigma_{\Phi^{Bz}} = \frac{\sqrt{2}}{\Upsilon}, \quad (5.1)$$

where Υ is the signal to noise ratio (SNR) in magnitude images. The SNR was calculated by dividing the mean of the ROI chosen inside the chamber with the SD of the ROI chosen outside the chamber. The result was then multiplied by a factor of 0.655 to compensate the noise distribution differences between areas inside and outside the chamber (R. Sadleir et al., 2005). The baseline noise for NC images was:

$$\sigma_{\Phi^{NC}} = \frac{1}{\Upsilon}, \quad (5.2)$$

because NC noise statistics did not involve subtraction effects.

5.2.12 Data Analysis

The means (μ) and standard deviations (SDs) (σ) of in phase images (Φ) and Laplacians of the phase images ($\nabla^2\Phi$) were calculated in each ROI. Results for the ASW and KCl groups were plotted together. There were four MREIT phase images (Φ^{Bz}) for each ganglion, Φ_1^{Bz}, Φ_2^{Bz}, Φ_3^{Bz}, Φ_4^{Bz}, where Φ_1^{Bz} and Φ_2^{Bz} represent images before the solution administration, and $\Phi^{Bz}{}_3$ and $\Phi^{Bz}{}_4$ represent images after solution administration. Differential images were also obtained by subtracting sequential MREIT phase images (i.e. $\Phi_2^{Bz} - \Phi_1^{Bz}$, $\Phi_3^{Bz} - \Phi_2^{Bz}$, $\Phi_4^{Bz} - \Phi_3^{Bz}$). Treatment and control group data were compared using two-tailed Student's t-tests. In all comparisons, significance level was set at $\alpha = 0.05$.

As an alternative analysis, histograms of data within each ROI in phase or Laplacian images were plotted and fitted to normal distributions using the Matlab function ‘fitdist (r,'Normal')’. The means and SDs of these distributions were also plotted and compared with two-tailed Student's t-tests. All variables used for analysis are listed

in appendix A. Cohen's d value was used to quantify effect sizes as described in chapter 2. The ratios for $\mu_{\sigma_{\Delta\Phi}}$, $\mu_{\sigma_{\Delta\nabla^2\Phi^{Bz}}}$, $\mu_{\sigma^{norm}_{\Delta\Phi^{Bz}}}$, and $\mu_{\sigma^{norm}_{\Delta\nabla^2\Phi^{Bz}}}$ between ASW and KCl group were also calculated.

5.3 Results

5.3.1 MEA Results

The spike numbers for 20 of the animals are shown in figure 5.5, nine from the ASW group and eleven from the KCl group. Half of the 32 channels were working for all MEA recordings. Spike signals were not recovered from the MEA recordings for ASW ganglion 1&3.

The means and SDs of the normalized spike numbers of each group are plotted in figure 5.6. It is clear that the spike rates were stable for the ASW group and that activity in the KCl group stopped after KCl administration. The average spike rate at the beginning of the experiment was 1 Hz. Immediately after the KCl treatment, the spiking rate typically burst to 3/s for about one min after which the activity ceased. The ASW administration had no effect on eventual spiking rates. This result matches well with Fu et al. (Fu et al., 2018). However, there was a typically a transient variation in spike rate (less than one min) that occurred immediately after the ASW addition.

5.3.2 Magnitude Image Data Analysis

Examples of magnitude images for ASW ganglion 1 and KCl ganglion 1, with and without current injections are shown in figure 5.7. The ROIs for the ganglion (AAG) and background (BK) are indicated in each image. μ_{μ_M} and σ_{μ_M} are the means and SDs

of the means of the ROIs in the magnitude images, respectively. These values are listed in table 5.1 and 5.2. The two values were calculated as:

$$\mu_{\mu_M} = (\sum_{i=1}^{11} \mu_{M_{(i)}})/11,$$

$$\sigma_{\mu_M} = \sqrt{\frac{\sum_{i=1}^{11}(\mu_{M_{(i)}} - \mu_{\mu_M})}{10}}, \quad (5.3)$$

where i = 1…11 included all 11 ganglia in each group. Table 5.1 indicates that the mean values dropped about 0.12 after the KCl administration for both the AAG and BK ROIs, whereas there was a 0.05 increase after the ASW addition for the AAG ROIs. In table 5.2, SDs increased about 0.04 for the BK ROIs in the ASW group and decreased about 0.04 for the AAG ROIs in the KCl group.

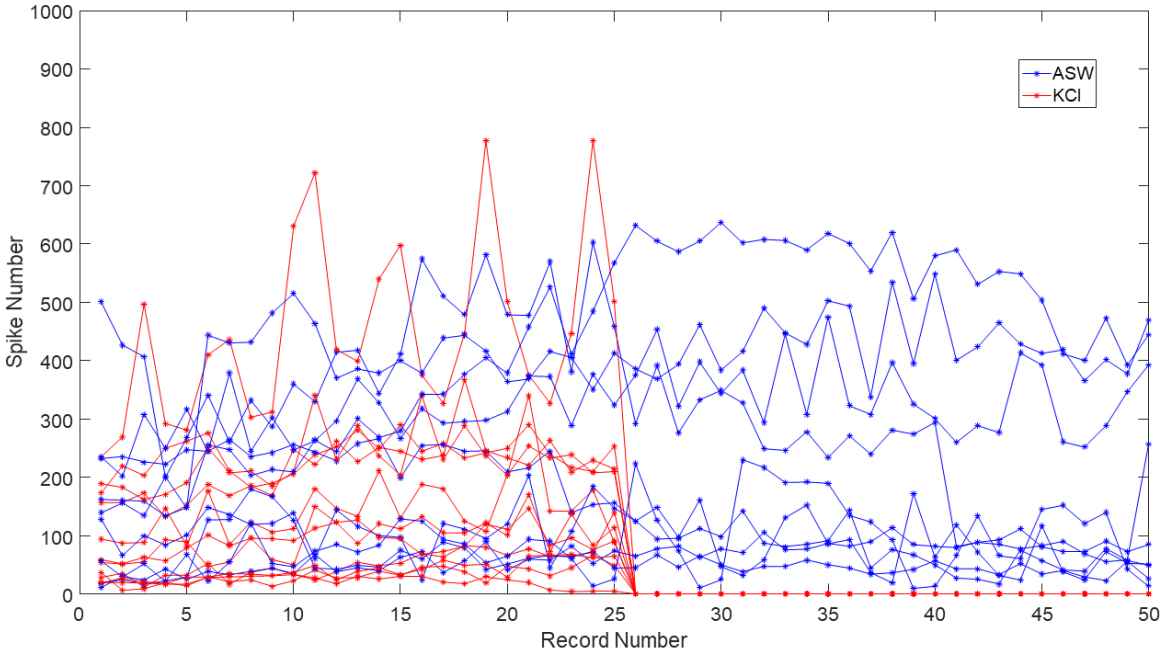

Figure 5.5 Spike numbers plotted against the recording time points for all ganglia. Each dot represents summed spike numbers recorded over one minute from all recordable channels. Blue plots show data from the ASW group and red plots represent data from the KCl group.

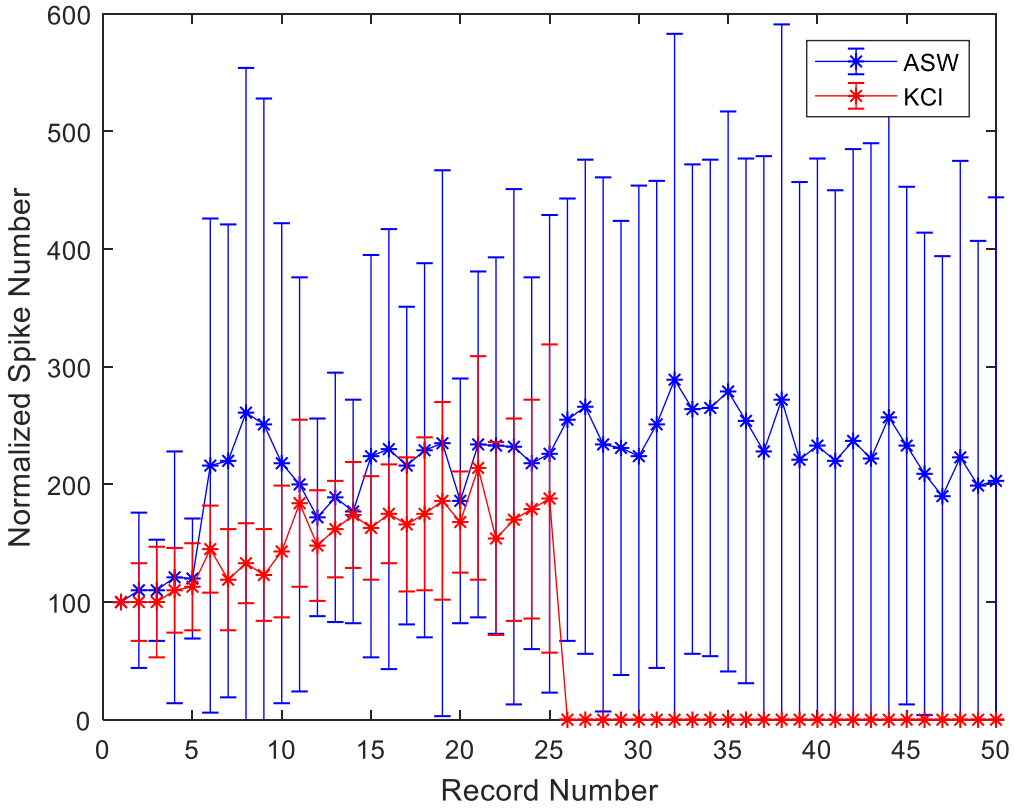

Figure 5.6 Means and SDs of normalized spike numbers for ASW and KCl groups. Each bar represents the mean and SD of the normalized spike number for ASW and KCl groups. The blue plots show the ASW group data and red plots show KCl group data.

Table 5.1

Averaged means within ROI regions of magnitude images (μ_{μ_M}).

μ_{μ_M}	M_1^{NC}	M_1^+	M_1^-	M_2^+	M_2^-	Solution addition	M_2^{NC}	M_3^+	M_3^-	M_4^+	M_4^-
ASW, AAG	1.13	1.15	1.15	1.16	1.16		1.22	1.21	1.21	1.21	1.19
ASW, BK	2.38	2.39	2.4	2.4	2.4		2.4	2.41	2.41	2.4	2.37
KCl, AAG	1.02	1.03	1.04	1.04	1.05		0.88	0.86	0.84	0.83	0.82
KCl, BK	2.3	2.31	2.3	2.31	2.31		2.18	2.18	2.18	2.18	2.19

Table 5.2

SDs of the means of within ROI regions of magnitude images (σ_{μ_M}).

σ_{μ_M}	M_1^{NC}	M_1^+	M_1^-	M_2^+	M_2^-	Solution addition	M_2^{NC}	M_3^+	M_3^-	M_4^+	M_4^-
ASW, AAG	0.18	0.2	0.2	0.2	0.2		0.19	0.19	0.19	0.19	0.19
ASW, BK	0.07	0.06	0.07	0.06	0.06		0.09	0.1	0.1	0.1	0.12
KCl, AAG	0.21	0.21	0.2	0.2	0.2		0.17	0.16	0.16	0.16	0.16
KCl, BK	0.07	0.07	0.06	0.05	0.06		0.06	0.06	0.07	0.06	0.07

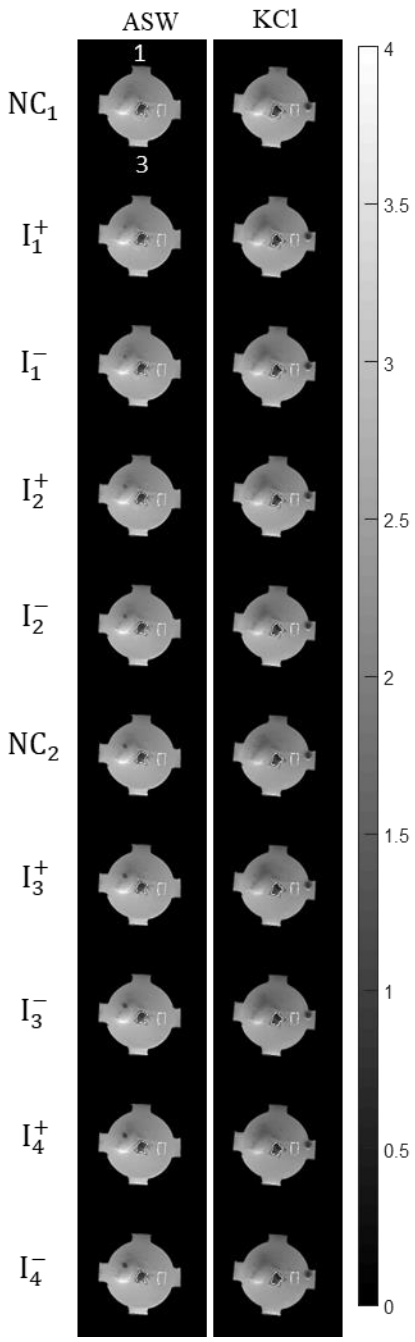

Figure 5.7 Magnitude images (M) for ASW ganglion 1 (left) and KCl ganglion 1 (right). The AAG and BK ROIs chosen for each animal are overlaid on the images. NC means no current injection, I^+ represents image with current injected from top to bottom, and I^- represents image with current injected from bottom to top.

5.3.3 MREIT Phase Image Data

Examples of MREIT phase images (Φ^{Bz}) for ASW 2 and KCl 2 ganglion are shown in figure 5.8. ROIs, segmented from magnitude images, are overlaid on the phase images. The means and SDs of the ROIs in the phase images are plotted in figure 5.9 with the outliers (KCl 7 & 8) removed. Averages of the mean and SDs of phase images within ROIs ($\mu_{\mu_{\Phi^{Bz}}}$ and $\mu_{\sigma_{\Phi^{Bz}}}$) were then calculated. The results are shown in table 5.3 ($\mu_{\mu_{\Phi^{Bz}}}$) and 5.4 ($\mu_{\sigma_{\Phi^{Bz}}}$). Student's T-tests were performed comparing these values between the two groups, with p values are noted on the plots shown in figure 5.9.

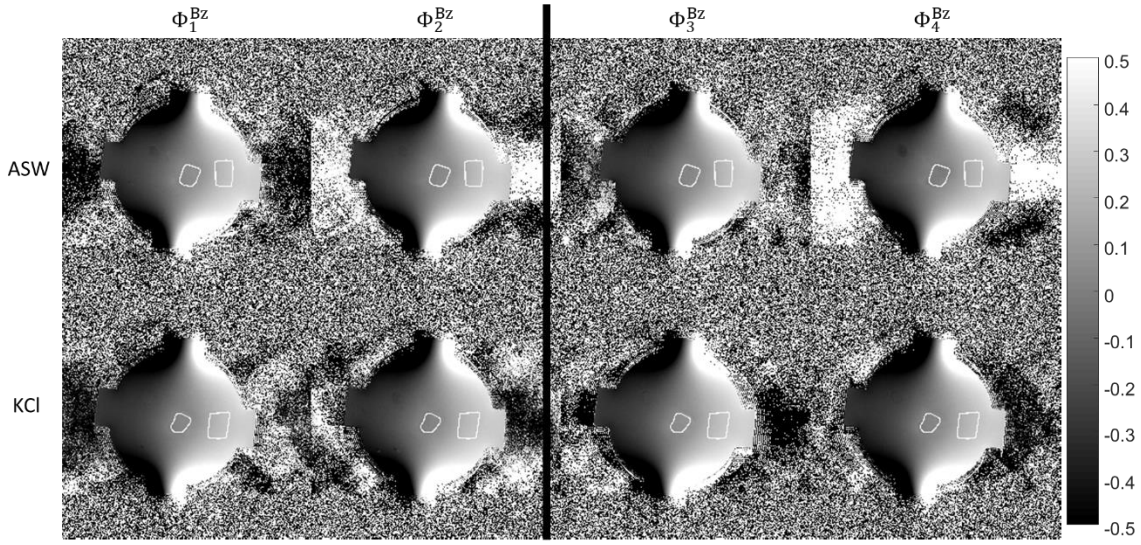

Figure 5.8 MREIT phase images (Φ^{Bz}) for ASW ganglion 2 (top row) and KCl ganglion 2 (bottom row). The AAG and BK ROIs are outlined in white.

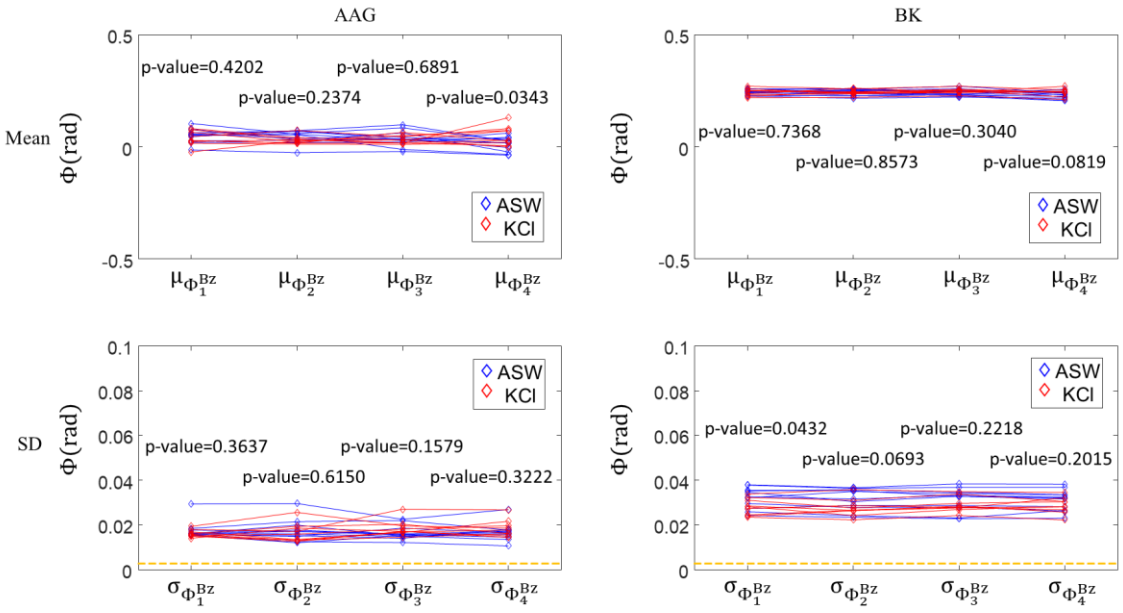

Figure 5.9 Means (top row) and SDs (bottom row) of the phase data in AAG (left) and BK (right) ROIs. Noise baselines calculated from magnitude images are shown on standard deviation plots. T-test p-values comparing treatment and control group values are overlaid on image points.

Table 5.3

Average means within ROIs in MREIT phase images ($\mu_{\mu_{\Phi Bz}}$).

$\mu_{\mu_{\Phi Bz}}$	$\mu_{\mu_{\Phi_1^{Bz}}}$	$\mu_{\mu_{\Phi_2^{Bz}}}$	Solution addition	$\mu_{\mu_{\Phi_3^{Bz}}}$	$\mu_{\mu_{\Phi_4^{Bz}}}$
ASW, AAG	4.90E-02	4.34E-02		3.67E-02	1.17E-02
KCl, AAG	3.78E-02	3.03E-02		3.16E-02	4.83E-02
ASW, BK	2.46E-01	2.42E-01		2.42E-01	2.30E-01
KCl, BK	2.44E-01	2.43E-01		2.48E-01	2.43E-01

Table 5.4

Average SDs within ROIs for MREIT phase images ($\mu_{\sigma_{\Phi^{Bz}}}$).

$\mu_{\sigma_{\Phi^{Bz}}}$	$\mu_{\sigma_{\Phi_1^{Bz}}}$	$\mu_{\sigma_{\Phi_2^{Bz}}}$	Solution addition	$\mu_{\sigma_{\Phi_3^{Bz}}}$	$\mu_{\sigma_{\Phi_4^{Bz}}}$
ASW, AAG	1.75E-02	1.76E-02		1.65E-02	1.68E-02
KCl, AAG	1.91E-02	1.78E-02		2.21E-02	1.98E-02
ASW, BK	3.21E-02	3.14E-02		3.14E-02	3.11E-02
KCl, BK	2.80E-02	2.79E-02		2.92E-02	2.87E-02

5.3.4 Laplacians of MREIT Phase Image Data

Examples of the Laplacians of the MREIT phase images ($\nabla^2\Phi^{Bz}$) for ASW ganglion 2 and KCl ganglion 2 are shown in figure 5.10. Outlines of ROIs segmented from the magnitude images are overlaid on the images. The means and SDs of the ROIs in the Laplacians of the phase images ($\mu_{\nabla^2\Phi^{Bz}}$ and $\sigma_{\nabla^2\Phi^{Bz}}$) are plotted in figure 5.11. The means for them ($\mu_{\mu_{\nabla^2\Phi^{Bz}}}$ and $\mu_{\sigma_{\nabla^2\Phi^{Bz}}}$) are listed in table 5.5 and 5.6. Student's T-tests were performed and noted in the plots (figure 5.11).

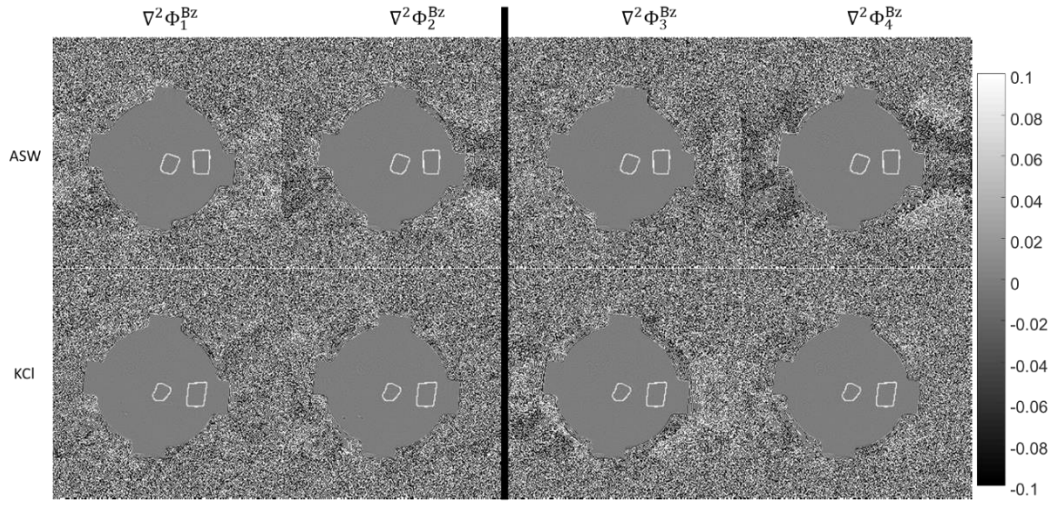

Figure 5.10 Laplacians of the MREIT phase images ($\nabla^2\Phi^{Bz}$) for ASW ganglion 1 (top row) and KCl ganglion 2 (bottom row). The AAG and BK ROIs are outlined in white. lines.

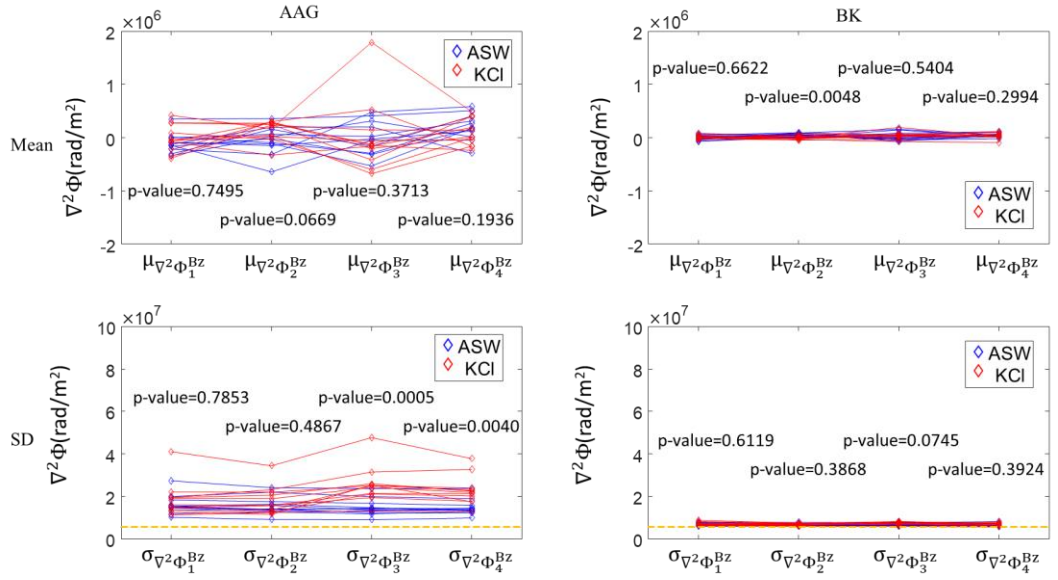

Figure 5.11 Means (top row) and SDs (bottom row) of Laplacian phase data in the AAG (left) and BK (right) ROIs ($\mu_{\nabla^2\Phi}$ and $\sigma_{\nabla^2\Phi}$). The ASW group is indicated by blue plots and the KCl group is indicated with red plots.

Table 5.5

Average means within ROIs in the MREIT Laplacian phase images ($\mu_{\mu_{\nabla^2\Phi^{Bz}}}$).

$\mu_{\mu_{\nabla^2\Phi^{Bz}}}$	$\mu_{\mu_{\nabla^2\Phi_1^{Bz}}}$	$\mu_{\mu_{\nabla^2\Phi_2^{Bz}}}$	Solution addition	$\mu_{\mu_{\nabla^2\Phi_3^{Bz}}}$	$\mu_{\mu_{\nabla^2\Phi_4^{Bz}}}$
ASW, AAG	-1.01E+05	-4.87E+04		4.95E+03	2.04E+05
KCl, AAG	-1.26E+04	1.39E+05		6.82E+03	9.52E+04
ASW, BK	-5.45E+02	5.25E+04		2.50E+04	4.74E+04
KCl, BK	4.89E+03	5.78E+02		3.88E+04	3.47E+04

Table 5.6

Average SDs within ROIs in the MREIT Laplacian phase images ($\mu_{\sigma_{\nabla^2\Phi^{Bz}}}$).

$\mu_{\sigma_{\nabla^2\Phi^{Bz}}}$	$\mu_{\sigma_{\nabla^2\Phi_1^{Bz}}}$	$\mu_{\sigma_{\nabla^2\Phi_2^{Bz}}}$	Solution addition	$\mu_{\sigma_{\nabla^2\Phi_3^{Bz}}}$	$\mu_{\sigma_{\nabla^2\Phi_4^{Bz}}}$
ASW, AAG	1.60E+07	1.56E+07		1.48E+07	1.48E+07
KCl, AAG	1.86E+07	1.82E+07		2.54E+07	2.28E+07
ASW, BK	6.78E+06	6.48E+06		6.74E+06	6.56E+06
KCl, BK	7.01E+06	6.73E+06		7.25E+06	6.88E+06

5.3.5 MREIT Baseline Noise Levels

The means and SDs of the SNRs for all images are listed in table 5.7. This established the MREIT experiment noise floor. The noise estimations found using $\mathrm{sd}(\Phi) = \frac{\sqrt{2}}{\gamma}$ were in the agreement with an alternative calculation (Sadleir et al. 2005) using $s_\Phi = \frac{1}{\sqrt{\frac{20}{\Delta^4}+\frac{6}{\Delta_z^4}}} s_{\nabla^2\Phi}$ as shown in table 5.8 and 5.9, where $s_{\nabla^2\Phi}$ is the standard deviation of the Gaussian random noise in $\nabla^2\Phi$. The agreement between the derived noise standard deviations suggests that the MREIT experiments were consistent.

Table 5.7

The SNRs (γ) of the MREIT experiments.

SNR	M_1^+	M_2^+	Solution addition	M_3^+	M_4^+
$\mu_{\gamma_{M_{ASW}^+}}$	393.84	393.23		393.19	393.73
$\sigma_{\gamma_{M_{ASW}^+}}$	7.80	7.61		6.54	10.09
$\mu_{\gamma_{M_{KCl}^+}}$	382.22	382.38		381.94	381.66
$\sigma_{\gamma_{M_{KCl}^+}}$	7.73	6.78		6.30	7.72

Table 5.8

Mean noise level estimations for MREIT experiments ($\mu_{\Phi^{Bz}}$).

$\mu_{\Phi^{Bz}}$	Φ_1^{Bz}		Φ_2^{Bz}		Solution addition	Φ_3^{Bz}		Φ_4^{Bz}	
	sd(Φ)	s_Φ	sd(Φ)	s_Φ		sd(Φ)	s_Φ	sd(Φ)	s_Φ
ASW	3.59E-03	3.88E-03	3.60E-03	4.01E-03		3.60E-03	4.23E-03	3.59E-03	3.79E-03
KCl	3.70E-03	4.19E-03	3.70E-03	4.00E-03		3.70E-03	4.61E-03	3.71E-03	4.41E-03

Table 5.9

SD in noise level estimations for MREIT experiments ($\sigma_{\Phi^{Bz}}$).

$\sigma_{\Phi^{Bz}}$	Φ_1^{Bz}		Φ_2^{Bz}		Solution addition	Φ_3^{Bz}		Φ_4^{Bz}	
	sd(Φ)	s_Φ	sd(Φ)	s_Φ		sd(Φ)	s_Φ	sd(Φ)	s_Φ
ASW	7.12E-05	4.95E-04	6.90E-05	5.06E-04		5.90E-05	5.31E-04	9.26E-05	4.59E-04
KCl	7.48E-05	6.79E-04	6.53E-05	3.28E-04		6.12E-05	9.11E-04	7.40E-05	5.75E-04

5.3.6 Comparisons of Φ^{NC} and Φ^{AVG} Data

To check the consistency of MREIT measurements, Φ^{NC} images were compared with Φ^{AVG} data. This is because averaged MREIT data constructed by adding I_x^- and I_x^+ images should be the same as NC data. An example of this comparison (from ASW ganglion 10 data) is shown in figure 5.12. The slope of the line was 0.99, with an offset of 0.007. This result agreed well with the assumption that $\Phi^{NC} = \Phi^{AVG}$.

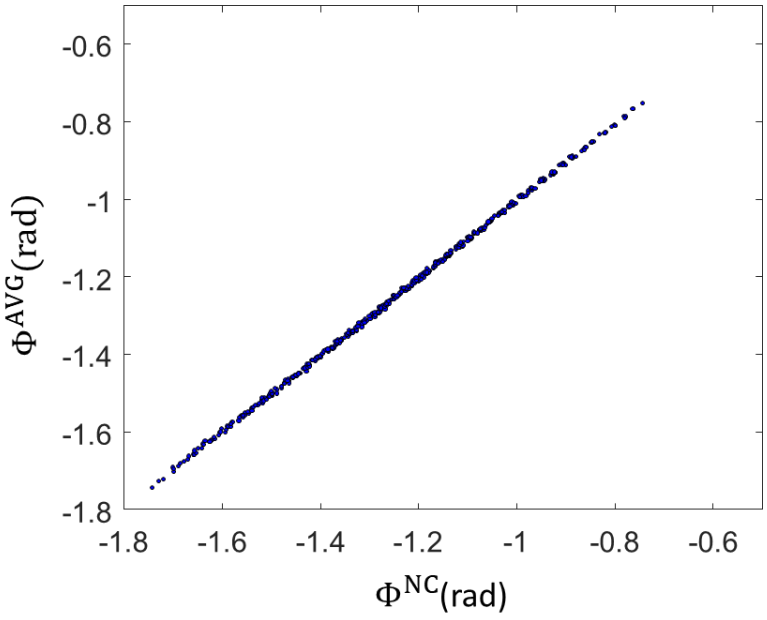

Figure 5.12 Scatterplot of Φ^{NC} against Φ^{AVG} for ASW ganglion 10 in the BK ROI.

5.3.7 NC Data Analysis

Examples comparing of NC phase and the Laplacians of phase images are shown in figure 5.13 and 5.16, respectively for ASW ganglion 2 and KCl ganglion 2. The SDs of the ROIs in the phase and Laplacians of the phase images are plotted in figure 5.14 and 5.17, respectively.

The means and SDs of the ROIs in the differential phases and differential Laplacians of NC phase images are plotted in figure 5.15 and 5.18, respectively. Student's t-tests were performed and p-values are noted above the plots.

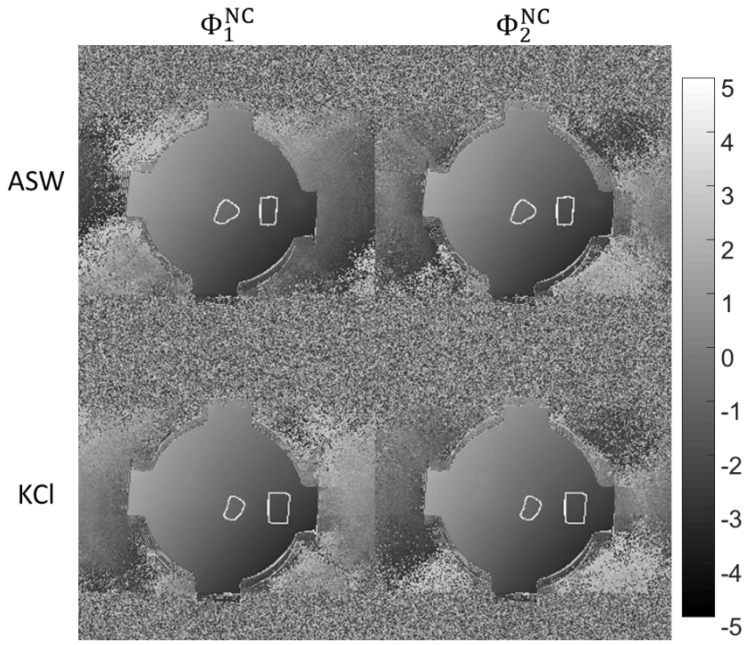

Figure 5.13 NC phase images for ASW ganglion 2 (top row) and KCl ganglion 2 (bottom row).

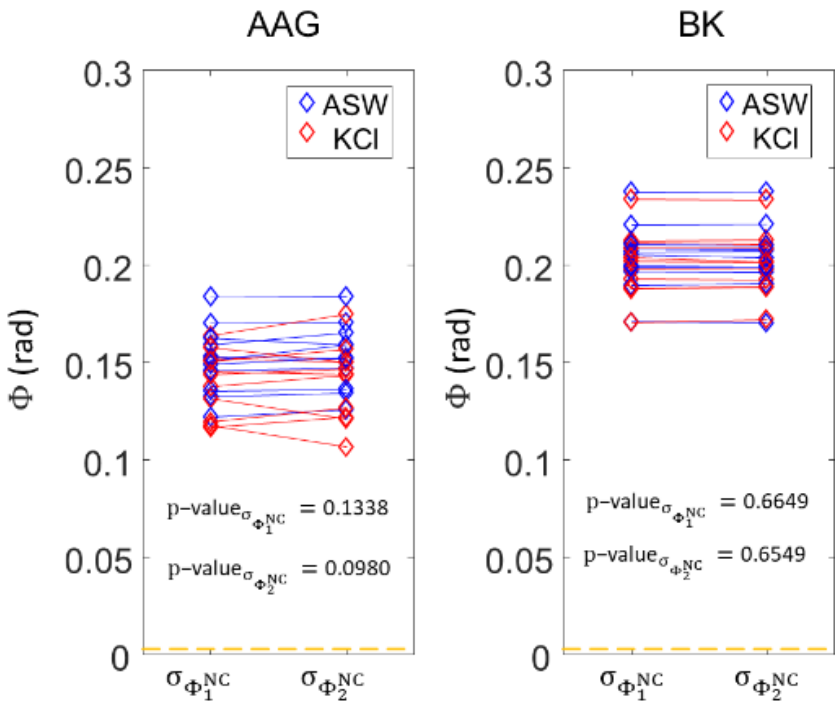

Figure 5.14 SDs within AAG and BK ROIs of NC phase images. The blue and red diamonds indicate data for ASW and KCl groups, respectively. The baseline noise level is marked by the yellow dotted line.

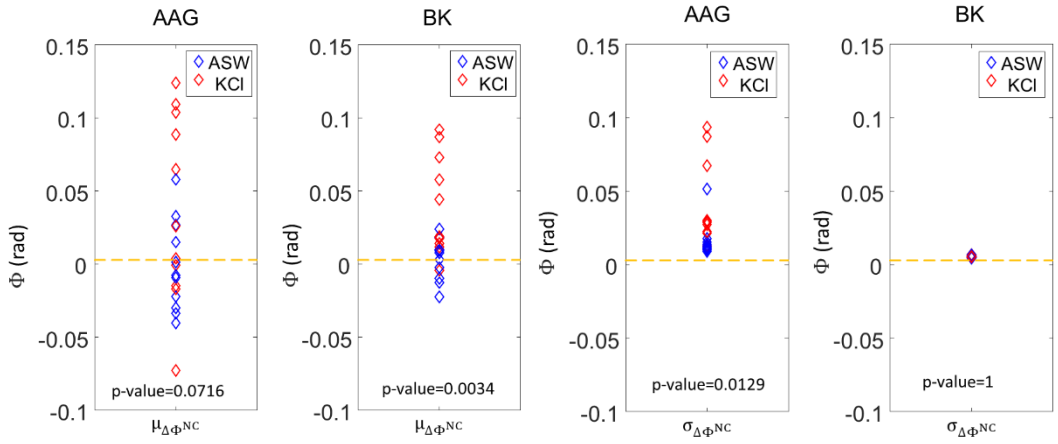

Figure 5.15 Means (left) and SDs (right) within the ROIs of differential NC phase images.

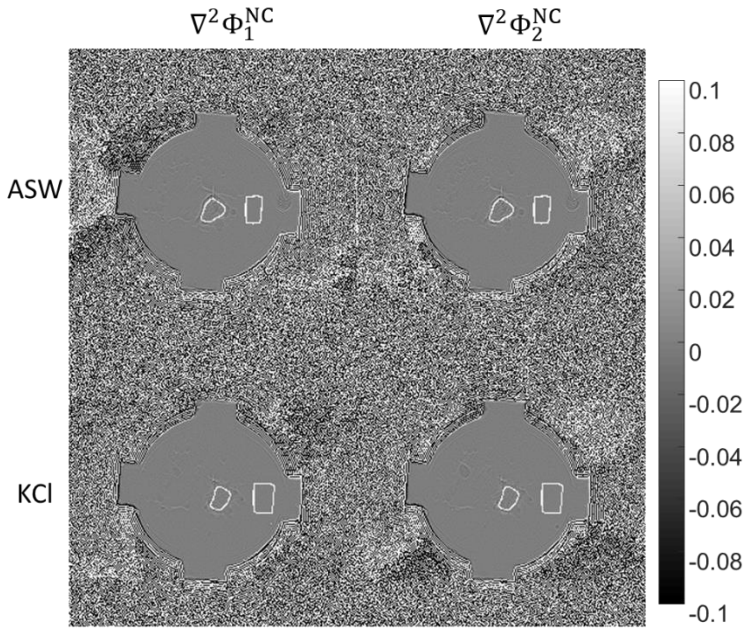

Figure 5.16 The NC Laplacians of the phase images for ASW ganglion 2 (top row) and KCl ganglion 2 (bottom row).

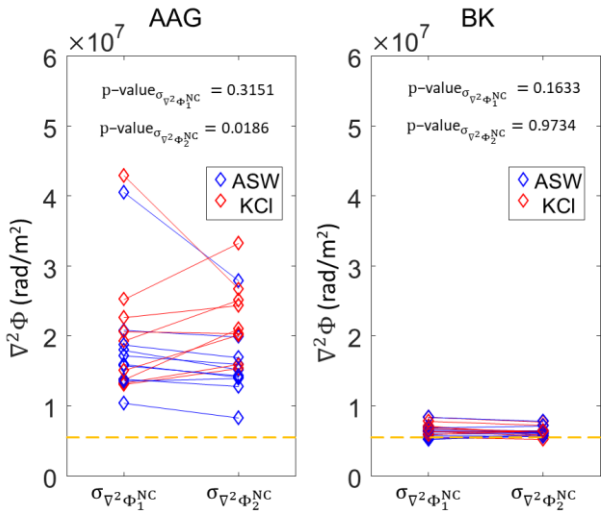

Figure 5.17 SDs within ROIs of NC Laplacian phase images. The blue and red diamonds indicate data for the ASW and KCl groups, respectively. Baseline noise levels are indicated by dotted yellow lines.

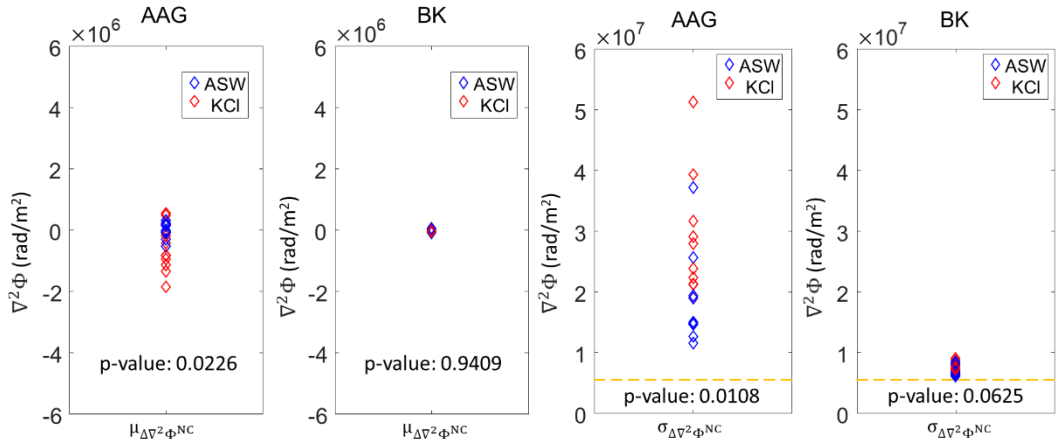

Figure 5.18 Means and SDs within ROIs of NC differential Laplacian phase images. Baseline noise levels are indicated by the dotted yellow line.

5.3.8 MREIT Differential Phase Images Analysis

Examples of differential phase images (ASW ganglion 2 and KCl ganglion 2) are shown in figure 5.19, and means and SDs calculated within ROIs are presented in figure 5.20. Data for AAG and BK ROIs were plotted separately. KCl ganglia 7 and 8 were not included in the plots as they produced data inconsistent with other observations. Student's t-tests were performed for all the above data combinations and were noted in figure 5.20. The means of the SDs within ROIs for differential phase images ($\mu_{\sigma_{\Delta\Phi}}$) are listed in table 5.10. The effect sizes and ratios of the ASW and KCl group were also calculated (table 5.10).

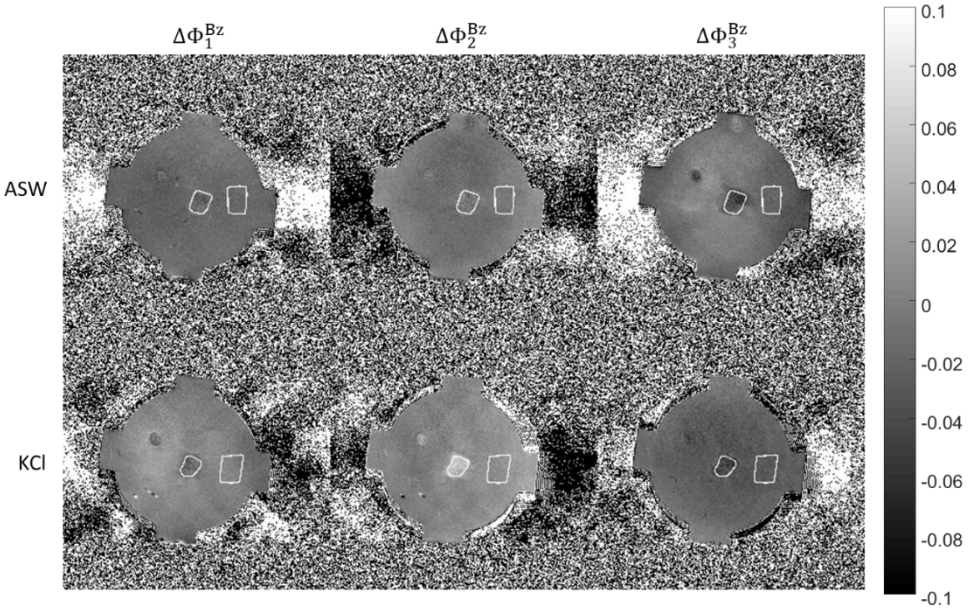

Figure 5.19 Differential phase images for ASW ganglion 2 (top row) and KCl ganglion 2 (bottom row). AAG and BK ROIs are outlined in white.

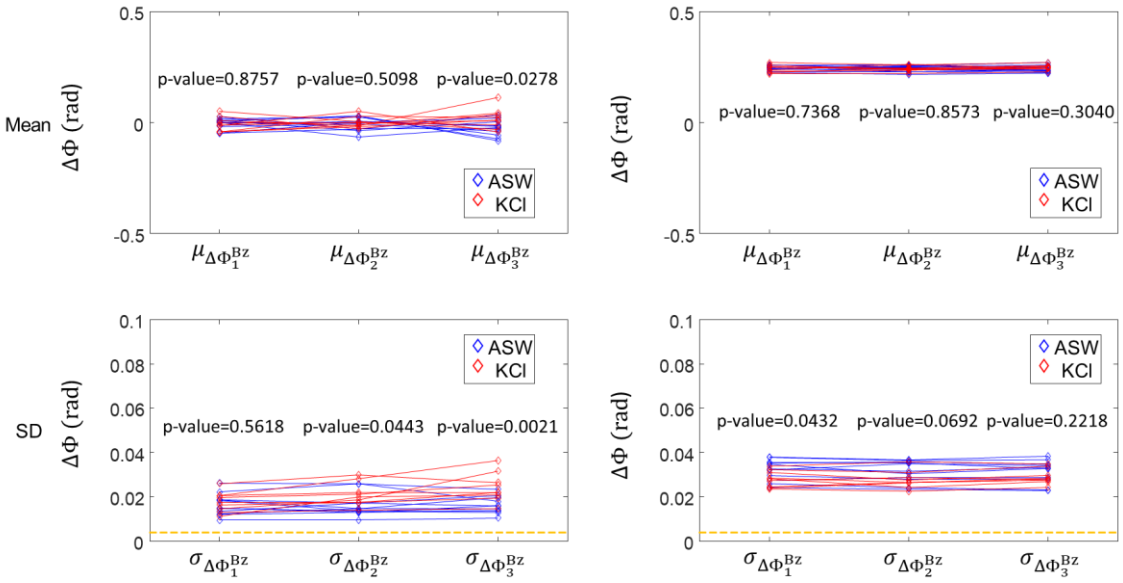

Figure 5.20 Means (top row) and SDs (bottom row) within AAG (left) and BK (right) ROIs of differential phase images. The p-values of t-test results comparing the two groups are overlaid at each comparison stage. Experimental noise floors are indicated by the yellow dotted line.

Table 5.10

Means of SDs within ROIs for differential phase images ($\mu_{\sigma_{\Delta\Phi}}$).

	$\mu_{\sigma_{\Delta\Phi_1^{Bz}}}$	Effect size	Ratio	$\mu_{\sigma_{\Delta\Phi_2^{Bz}}}$	Effect size	Ratio	$\mu_{\sigma_{\Delta\Phi_3^{Bz}}}$	Effect size	Ratio
ASW, BK	3.21E-02	0.9921	0.8754	3.14E-02	0.8794	0.8822	3.14E-02	0.5818	0.9236
KCl, BK	2.81E-02			2.77E-02			2.90E-02		
ASW, AAG	1.65E-02	0.2670	1.0727	1.62E-02	0.9735	1.2963	1.63E-02	1.5688	1.4908
KCl, AAG	1.77E-02			2.10E-02			2.43E-02		

5.3.9 MREIT Differential Laplacian of Phase Analysis

Examples of differential Laplacian phase images are shown in figure 5.21 (ASW ganglion 2 and KCl ganglion 2). Means and SDs within ROIs for differential Laplacians of the ASW and KCl group are plotted in figure 5.22. The AAG and BK ROIs are shown

separately. The blue plots represent the ASW group and the red plots represent ganglia in the KCl group. KCl ganglia 7 and 8 were not included in the plots as they were inconsistent with other observations. Student's t-tests comparing data from each group were performed for all the above analysis, and p-values are noted in figure 5.22. The means of SDs within ROIs in the differential Laplacian phase images ($\mu_{\sigma_{\Delta\nabla^2\Phi}}$) are listed in table 5.11. The effect sizes and the ratios of the ASW and KCl group were calculated (table 5.11).

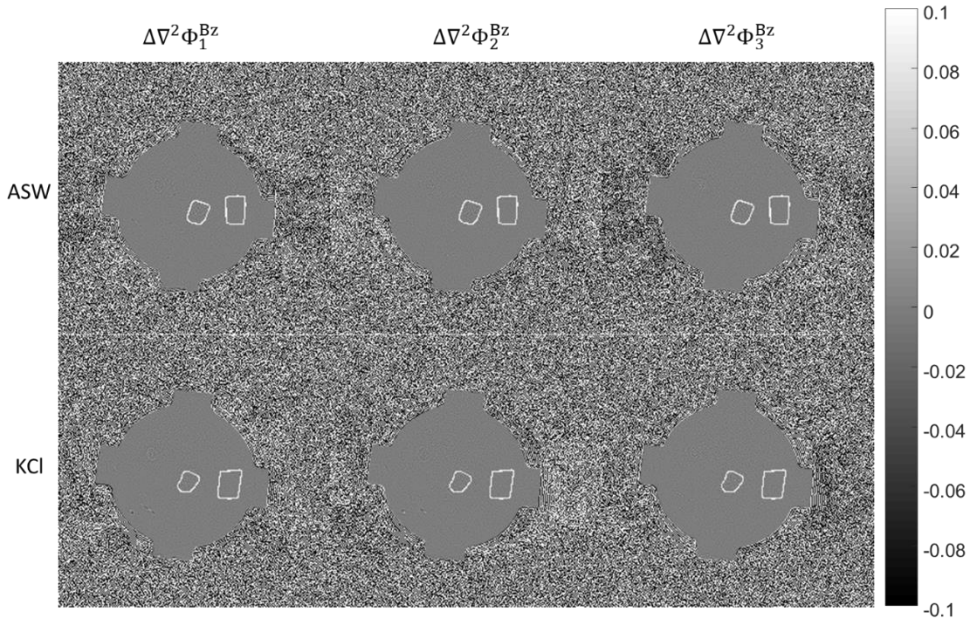

Figure 5.21 Differential Laplacians of MREIT phase images for ASW ganglion 2 (top row) and KCl ganglion 2 (bottom row). AAG and BK ROIs are outlined in white.

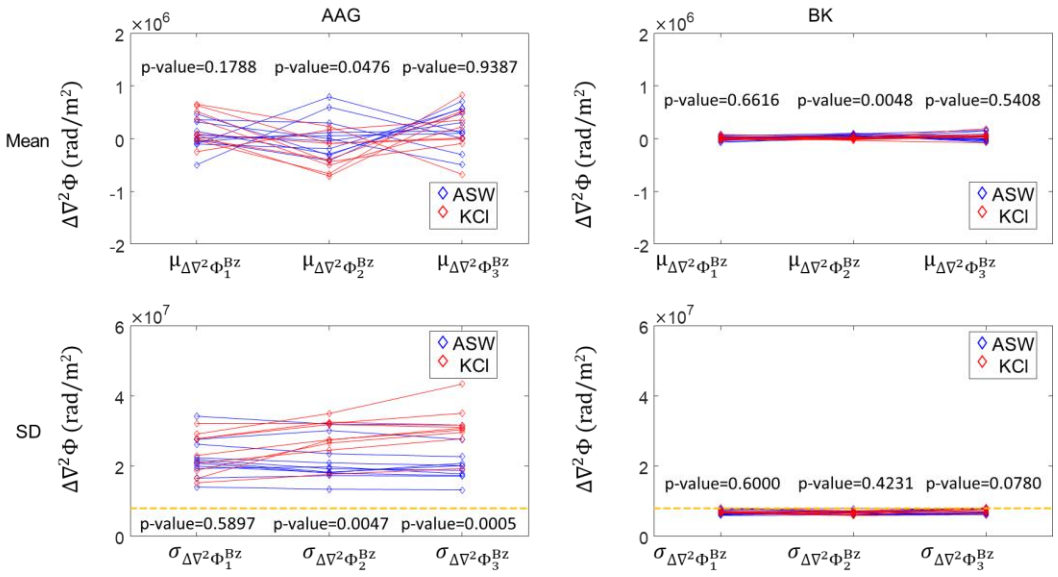

Figure 5.22 Means (top row) and SDs (bottom row) within AAG (left) and BK (right) ROIs for Laplacian phase images.

Table 5.11

Mean values of the SDs within ROIs in differential Laplacian phase images ($\mu_{\sigma_{\Delta\nabla^2\Phi^{Bz}}}$).

	$\mu_{\sigma_{\Delta\nabla^2\Phi_1^{Bz}}}$	Effect size	Ratio	$\mu_{\sigma_{\Delta\nabla^2\Phi_2^{Bz}}}$	Effect size	Ratio	$\mu_{\sigma_{\Delta\nabla^2\Phi_3^{Bz}}}$	Effect size	Ratio
ASW, BK	6.78E+06	0.2423	1.0199	6.48E+06	0.3715	1.0300	6.74E+06	0.8409	1.0820
KCl, BK	6.91E+06			6.69E+06			7.30E+06		
ASW, AAG	2.22E+07	0.2457	1.0608	2.10E+07	1.4548	1.3571	2.07E+07	1.8864	1.5000
KCl, AAG	2.34E+07			2.84E+07			3.10E+07		

5.3.10 Histogram Phase Image Analysis

Examples of the histograms of the ROIs in the phase images are shown in figure 5.23 (ASW 2 and KCl 2 ganglion). Gaussian Fittings were performed for all the histograms. The means (μ) and SDs (σ) of the normal distributions are displayed in figure 5.24. KCl 7, and 8 were not included in the plots as they were distant from the other

observations. Student's t-tests were performed for all the above analyses and p-values are noted in figure 5.24.

5.3.11 Histogram Laplacian Phase Analysis

Example histograms of Laplacian phase image data within ROIs are shown in figure 5.25 (ASW ganglion 2 and KCl ganglion 2). Gaussian fitting was performed for all histograms. The means (μ) and SDs (σ) of the normal distributions are shown in figure 5.26. KCl ganglia 7 and 8 were not included in the analysis as they produced inconsistent results. Student's t-tests were performed for all the above analyses and p-values are noted in figure 5.26.

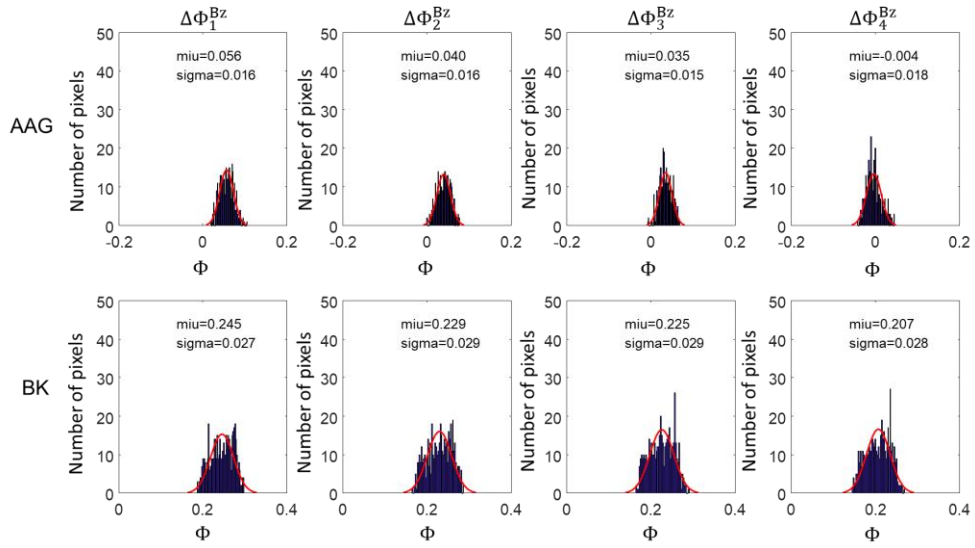

(a)

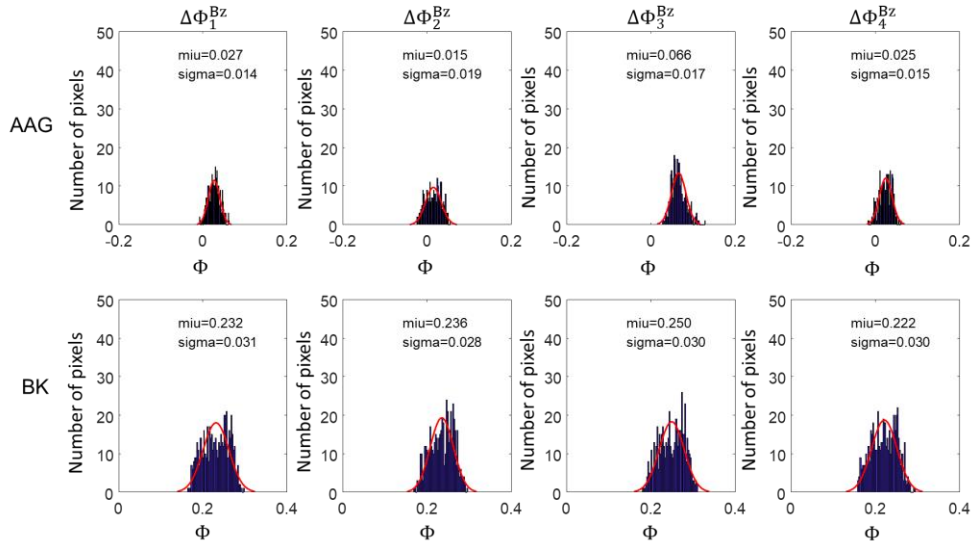

(b)

Figure 5.23 Histograms of data within AAG (top row) and BK (bottom row) ROIs in phase images of ASW ganglion 2 (a) and KCl ganglion 2 (b). Red curves indicate Gaussian fits.

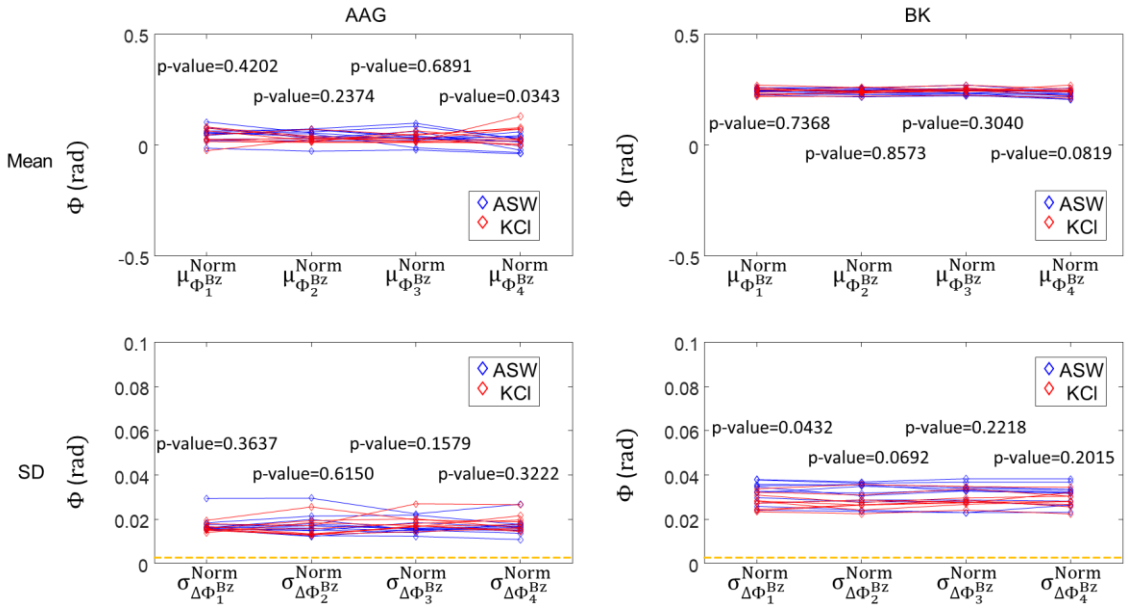

Figure 5.24 Means (μ^{norm}) (top row) and SDs (σ^{norm}) (bottom row) of fitted normal distributions found for data within AAG (left) and BK (right) ROIs for phase images.

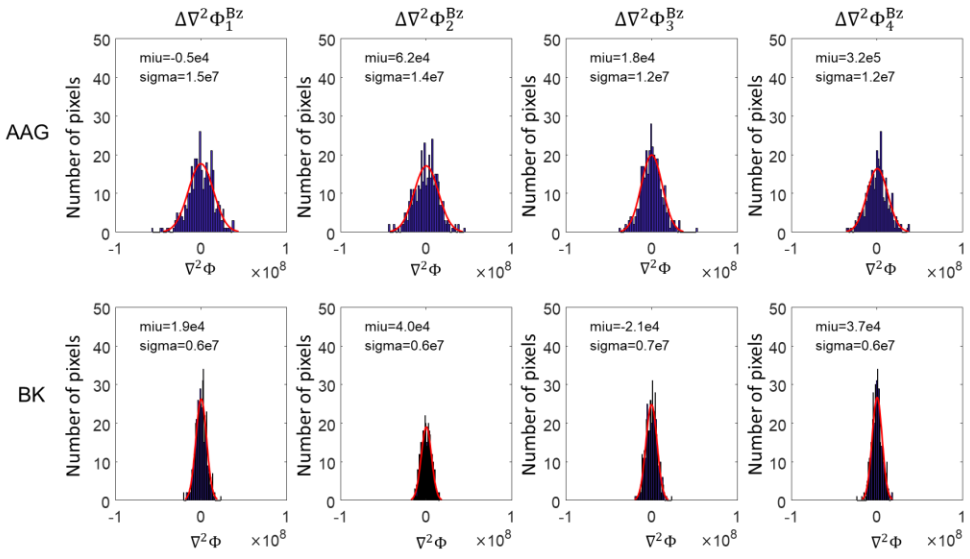

(a)

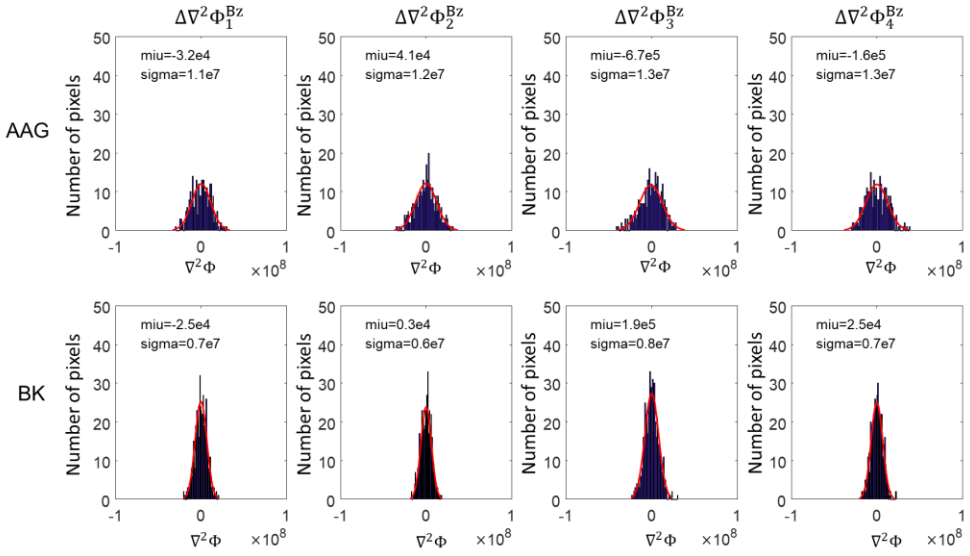

(b)

Figure 5.25 Histograms of Laplacian phase images within AAG and BK ROIs for ASW ganglion 2 (a) and KCl ganglion 2 (b). Red curves represent Gaussian fits.

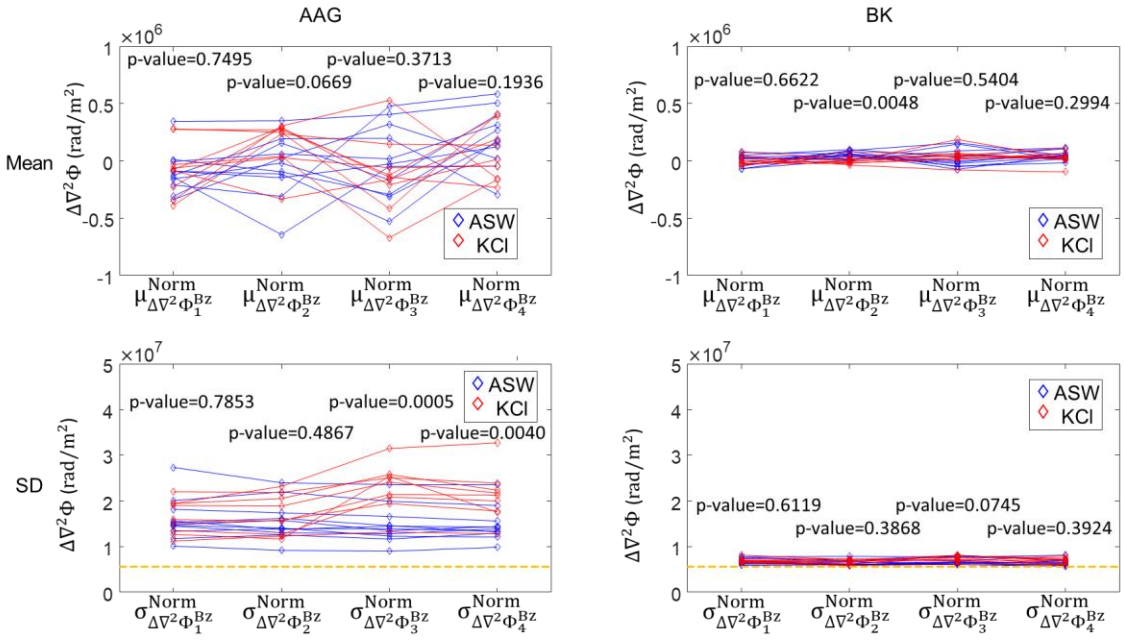

Figure 5.26 Means (μ^{norm}) (top row) and SDs (σ^{norm}) (bottom row) of the fitted normal distributions to data within the AAG (left) and BK (right) ROIs for Laplacian phase images.

5.3.12 Histogram Differential Phase Image Analysis

Example histograms of data within ROIs of differential phase images are shown in figure 5.27 (ASW ganglion 2 and KCl ganglion 2). Gaussian fits were performed for all histograms. The means (μ) and SDs (σ) of the normal distributions are shown in figure 5.28. KCl ganglia 1, 7, and 8 were not included in the plots as they were inconsistent with other observations. Student's t-tests were performed for all analysis and p-values are noted in figure 5.28. Effect sizes and the ratios of the ASW and KCl group were calculated and listed in table 5.12.

5.3.13 Histogram Differential Laplacian of Phase Analysis

Examples histograms of data within ROIs in differential Laplacian phase images are shown in figure 5.29 (ASW ganglion 2 and KCl ganglion 2). Gaussian fits were performed to all histograms. Means (μ) and SDs (σ) of the normal distributions are tabulated in figure 5.30. KCl 7 and 8 were not included in the plot as they were outliers. Student's t-tests were performed for all the above analysis and were noted in figure 5.30. The effect sizes and ratios of the ASW and KCl group were calculated and are listed in table 5.13.

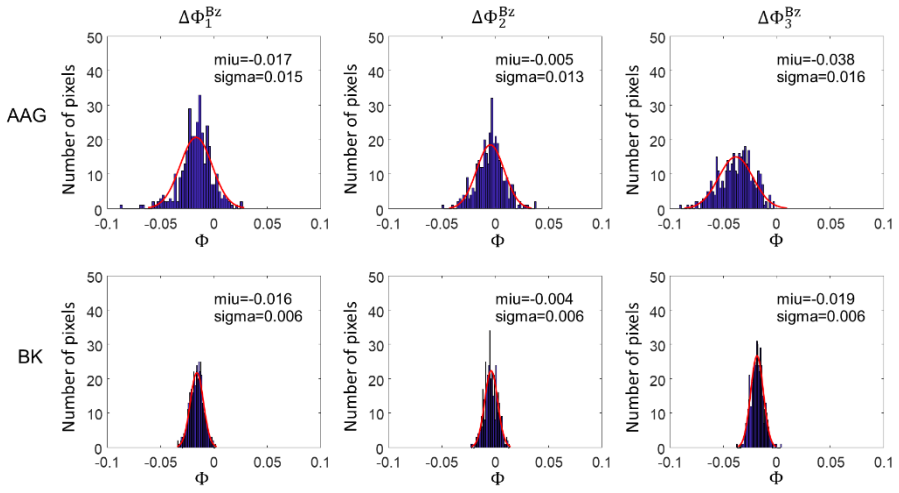

(a)

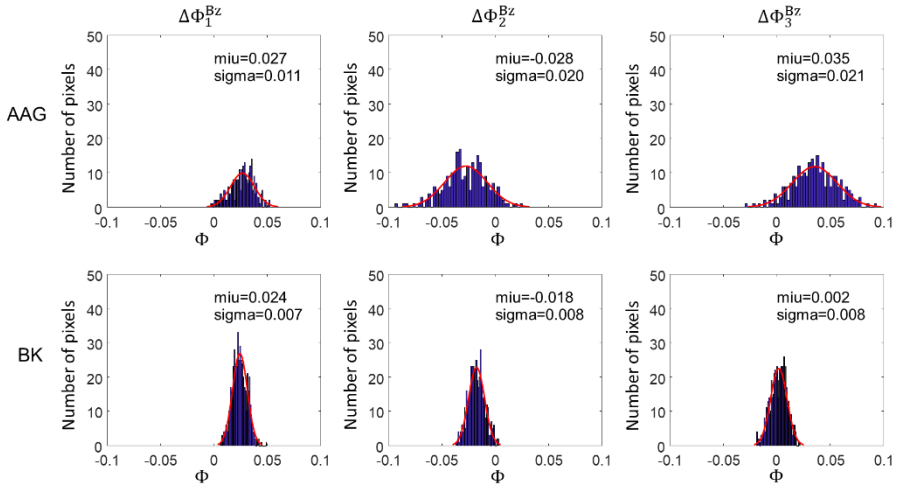

(b)

Figure 5.27 Histograms of data within AAG (top row) and BK (bottom row) ROIs in the differential phase images of ASW ganglion 2 (a) and KCl ganglion 2 (b). Red curves represent normal distribution fits.

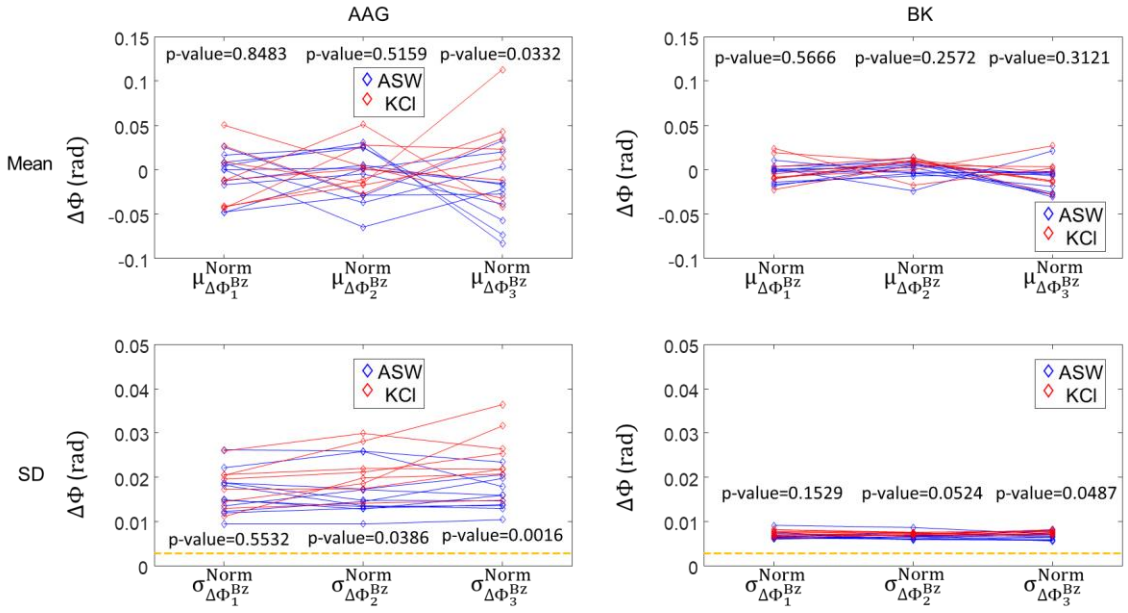

Figure 5.28 Means (μ^{norm}) (top row) and SDs (σ^{norm}) (bottom row) in fitted normal distributions of data within AAG (left) and BK (right) ROIs for differential phase images.

Table 5.12

Means of SDs of normal distributions ($\mu_{\sigma^{norm}_{\Delta\Phi^{Bz}}}$), and effect sizes and ratios of SDs of fitted normal distributions ($\sigma^{norm}_{\Delta\Phi^{Bz}}$) between the ASW and KCl group.

	$\mu_{\sigma^{norm}_{\Delta\Phi^{Bz}_1}}$	Effect size	Ratio	$\mu_{\sigma^{norm}_{\Delta\Phi^{Bz}_2}}$	Effect size	Ratio	$\mu_{\sigma^{norm}_{\Delta\Phi^{Bz}_3}}$	Effect size	Ratio
ASW, BK	6.82E-03	0.7123	1.079	6.67E-03	1.0328	1.088	6.78E-03	1.0373	1.100
KCl, BK	7.36E-03			7.26E-03			7.46E-03		
ASW, AAG	1.65E-02	0.2820	1.079	1.62E-02	1.0421	1.321	1.63E-02	1.6645	1.528
KCl, AAG	1.78E-02			2.14E-02			2.49E-02		

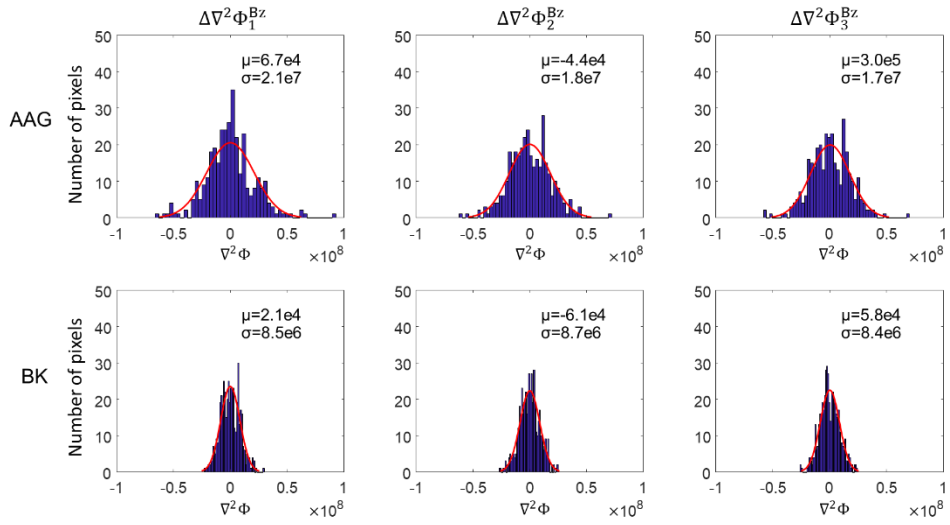

(a)

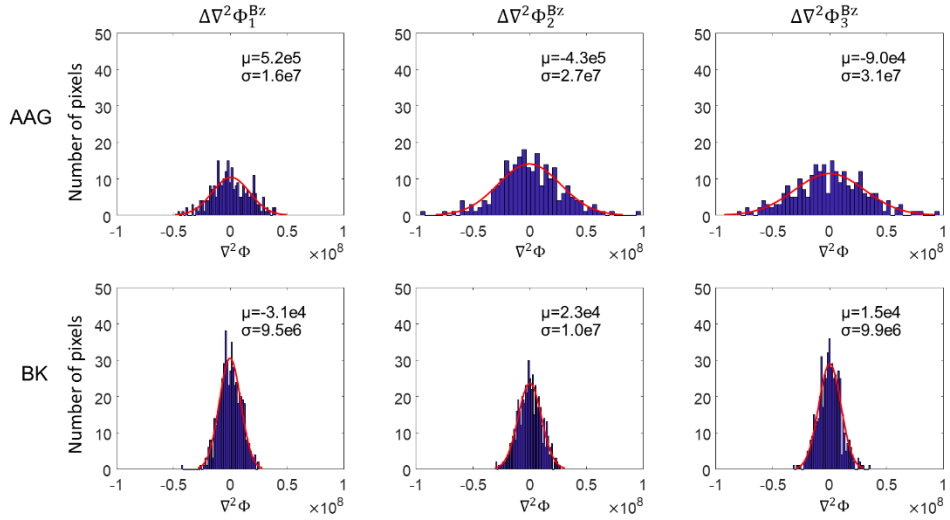

(b)

Figure 5.29 Histograms of differential Laplacian phase images within the AAG and BK ROIs for ASW ganglion 2 (a) and KCl ganglion 2 (b). Red curves represent normal distribution fits.

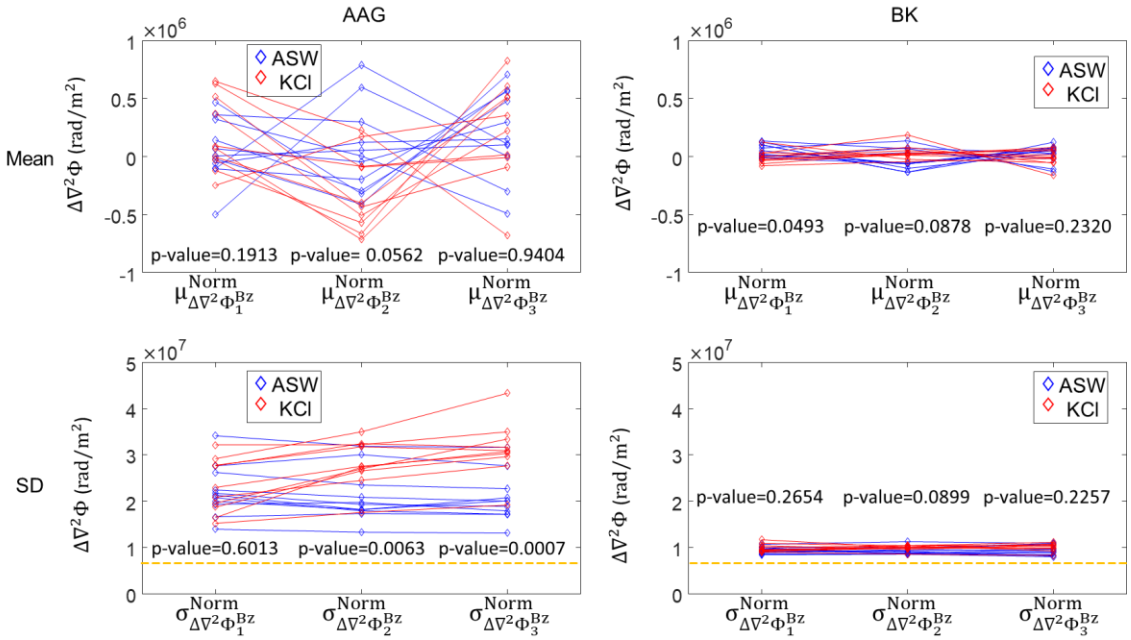

Figure 5.30 Means (μ^{norm}) (top row) and SDs (σ^{norm}) (bottom row) of fitted normal distributions within AAG (left) and BK (right) ROIs for differential Laplacian phase images.

Table 5.13

Means of SDs of the fitted normal distributions ($\mu_{\sigma^{norm}_{\Delta\nabla^2\Phi^{Bz}}}$) and effect sizes and ratios of SDs of fitted normal distributions ($\sigma^{norm}_{\Delta\nabla^2\Phi_2^{Bz}}$) comparing ASW and KCl groups.

	$\mu_{\sigma^{norm}_{\Delta\nabla^2\Phi_1^{Bz}}}$	Effect size	Ratio	$\mu_{\sigma^{norm}_{\Delta\nabla^2\Phi_2^{Bz}}}$	Effect size	Ratio	$\mu_{\sigma^{norm}_{\Delta\nabla^2\Phi_3^{Bz}}}$	Effect size	Ratio
ASW, BK	9.32E+06	0.5417	1.0385	9.33E+06	0.8608	1.0641	9.40E+06	0.5968	1.0572
KCl, BK	9.68E+06			9.93E+06			9.95E+06		
ASW, AAG	2.22E+07	0.2457	1.0608	2.10E+07	1.4548	1.3571	2.07E+07	1.8864	1.5000
KCl, AAG	2.61E+07			3.11E+07			3.42E+07		

5.4 Discussion

5.4.1 Anticipated Findings

The experimental design used in this study was similar to that used in Sadleir et al. (R. J. Sadleir et al., 2017), except that the KCl treatment here caused cessation of action potentials, whereas in Sadleir et al. (2017) the KCl concentration persistently increased activity levels. Therefore, we expected that the SD of phase images within AAG ROIs for the KCl group would be lower than for the ASW group, as it was anticipated that fewer action potentials would correspond to less overall membrane conductivity change, and thus smaller phase variation.

5.4.2 Baseline Noise Levels in MREIT Images

The baseline phase noise levels in the experiment were calculated to be around 0.0036 rad. These levels were found to be similar for both the ASW and KCl group, before and after the treatment.

5.4.3 NC Data Analysis

The AVG images were similar to the NC images in the BK ROIs. This is expected because averaging of MREIT data should cancel any external-current induced effects.

Significant differences were found between the ASW and KCl group in both the differential phase images and differential Laplacians of NC phase images. For the differential phase images, differences were found in BK, which was unexpected. The reason could be that the added solution was not intensively mixed with ASW gel when the second NC scan started. The time between the NC scan and the solution addition was

about 15 mins. A longer time interval could be used in the future experiment to investigate this result.

For differential Laplacian phase images, the BK between two groups matched well with each other. Meanwhile, significant differences were found for the AAG ROIs as shown in figure 5.18. The Laplacian of an image emphasizes the regions of rapid phase change, thus, the differences in BK ROIs were not significant and neural activity could be the reason for the differences for the AAG ROIs. This could indicate that the experiment was able to detect differences in membrane conductance variability even without current administration.

5.4.4 Changes in BK-Expectations and Findings

Statistical measures computed within BKs ROIs were consistent between the two groups for both phase and Laplacian phase analysis. The p-values were smaller than 0.05 in some cases, but all effect sizes and ratios were smaller than in AAG ROIs. These results were as expected and increased our confidence in the AAG findings.

5.4.5 Changes in AAG-Expectations and Findings

The SDs of the AAG in the differential phase images and Laplacians of the phase images showed significant differences between the ASW and KCl groups after the solution addition, but the KCl group showed higher SDs than the ASW group after which was conflict with expectations. Observation of larger SDs in the Laplacian phase images post KCl administration indicated there were more conductivity variations and not less. It is possible that the KCl administration caused more conductivity changes even if action potentials had ceased. Future experiments should be performed using alternative

treatments or patch clamping should be performed to determine if this may have been the case.

5.4.6 Experimental Limitations

In this experiment, the spontaneous AAG activity was not synchronized with the MREIT current injections and thus potentially decreased the signals detected by the MREIT. Furthermore, the KCl treatment could cause cell shrinkage and confuse the relationship between the membrane conductivity and neural activity.

6 SUMMARY AND FUTURE DIRECTIONS

6.1.1 Summary

The main purpose of this dissertation was to design a comprehensive experiment to demonstrate the feasibility of the fMREIT method. Chapter 2-5 described the stages of preparation for fMREIT experiments from treatment characterization, effect-size simulation and experimental testing to the final experiment.

Chapter 2 demonstrated that a high concentration KCl solution can be used to stop AAG action potentials, and this effect is reversible. It also supports that the one milliamp external current injection had no persistent effect on the spiking rates during the experiment.

In Chapter 3, a finite element simulation was performed using a bidomain model coupled using a Hodgkin-Huxley membrane model. It was found that the external current injection may affect the internal neural activity levels, and that increases in both internal and external current amplitudes caused non-linear effects on maximum signal levels. It was also demonstrated that fMREIT may have the potential to detect membrane conductance changes using the MRI protocols used in the simulation and with one milliamp external current injection.

In Chapter 4, the MHD effect observed in the fMREIT experiment was discussed. It was concluded that the MHD effect was influenced by the sample chamber dimension, background material viscosity, and the main magnetic field strength. Therefore, in final

experiments, the viscosity of background media was increased to minimize the MHD effects.

In Chapter 5, the main fMREIT experiments were described. Results from 22 AAG, the ASW (control) and KCl (treatment) were presented. A 1 mA external current was applied. Significant differences were found between the two groups based on the Laplacian phase images analysis and differences were maintained in fitted histogram and differential analyses.

6.1.2 Future Experiments

Preliminary works have demonstrated that a retina fMREIT experiment is feasible. Use of salamander retinal samples and light-evoked responses synchronized to MREIT imaging should provide a more convenient method to evaluate the potential of fMREIT.

In our preliminary salamander retina fMREIT work, the retina dissection was operated under dim red light to prevent the retina blenching. After removal, the retinas were stored in Ringer's solution (Fisher Science Education). The Ringer's solution contained 5 mM glucose and was oxygenated with carbogen for half an hour before dissection commenced. Sodium bicarbonate was used to adjust the pH of the Ringer's solution to 8.0. Because of the possibility of MHD effects in 800 MHz MREIT, a working solution was made by adding a 0.7 g Methylcellulose powder (SIGMA) into a 20 ml solution to increase the viscosity of the media used to support the retinal samples.

We observed electrical activity in the retina around the onset of light exposure in the benchtop experiment using a microelectrode array. Experiments were performed

where imaging currents were applied synchronously with a light stimulus and these images were compared with those collected without light stimulus to determine differences could be discerned in fMREIT phase images. A candidate retinal fMREIT experimental protocol is shown in figure 6.1. The pulse sequence, including light schedule, is shown in figure 6.2. To examine the differences between the images with and without light-evoked activity, the experiments would be split into two sets: the first involving light stimulation and the second performed without light. The fMREIT imaging would be interleaved with flexMEA recordings lasting one minute each. Two scans in each set would be obtained with current application via a single pair of electrodes (separate positive and negative current injection images).

The data analysis performed would be similar to those already shown for AAG fMREIT experiments. MREIT phase images would be obtained by complex dividing the positive and negative current MREIT data. A homogeneous area within the retinal tissue would be chosen as an ROI. The standard deviation of the phase and Laplacian of the phase within the ROI would then be calculated and compared.

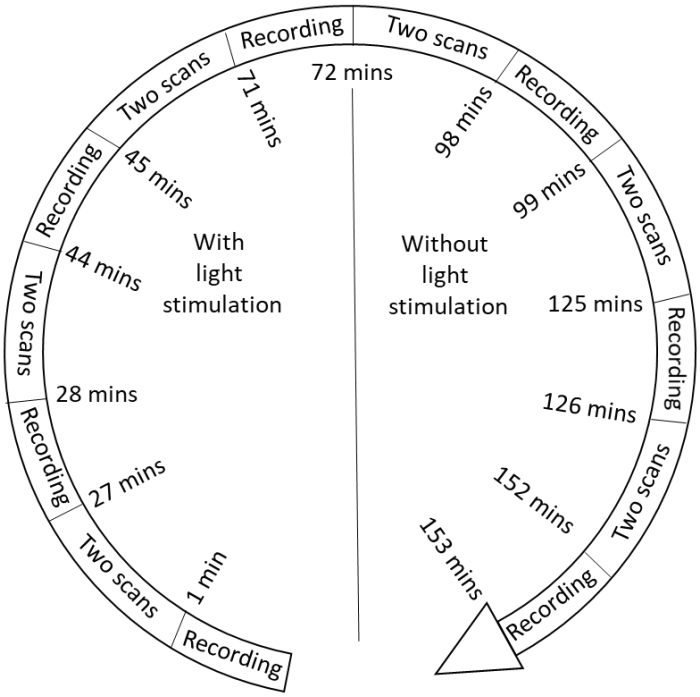

Figure 6.1 Example procedure for retinal fMREIT experiment. Blocks of MREIT scans are interleaved with the flexMEA recordings.

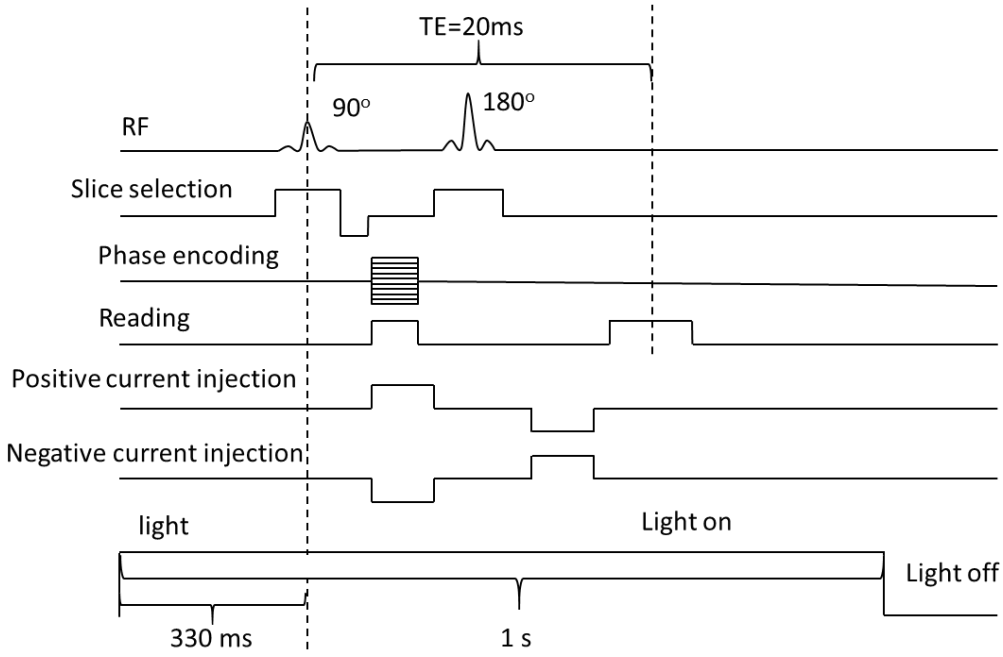

Figure 6.2 Spin-echo-based MREIT sequence for use with retinal fMREIT experiments. The first four lines show the standard sequence and the following two lines represent MREIT current injections. Positive and negative current injection images are obtained separately. The final line shows the light stimulation sequence to be used in experiments.

One of the challenges for retinal fMREIT is the thinness of the retina, which limits slice thickness and thus reduces the SNR. This can be partially overcome by using gadolinium and by increasing the number of averages in scans. Another challenge is the limited life circle of the retina inside an MRI machine. Our preliminary benchtop experiment showed that the retina can survive in the ringer's gel solution for about four hours without perfusion, which is shorter than the ~10 h lifetime of the AAG during imaging.

6.1.3 Future Directions

While these results showed that measurement of membrane conductance variations using fMREIT may be feasible, more work is required to apply this technique in vivo. Short scan times are necessary for studies in vivo. In these cases Multishot Echo Planar MREIT (Chauhan, Vidya Shankar, et al., 2018) may be a useful method for decreasing scan times. Another factor that may impede detection of membrane conductance changes in vivo is the effect of localized changes in blood flow volume on phase. The inhomogeneity caused by deoxyhemoglobin may also cause variations in phase images and could obscure fMREIT signals. Thus, development of methods to avoid BOLD and blood-flow-related effects on phase images is crucial.

REFERENCES

Agnew, W., Yuen, T., McCreery, D., & Bullara, L. (1986). Histopathologic evaluation of prolonged intracortical electrical stimulation. *Experimental neurology, 92*(1), 162-185.

Al-Fatly, B. (2018). Coherence: a unifying mechanism of deep brain stimulation. *Journal of neurophysiology*.

Antal, A., Boros, K., Poreisz, C., Chaieb, L., Terney, D., & Paulus, W. (2008). Comparatively weak after-effects of transcranial alternating current stimulation (tACS) on cortical excitability in humans. *Brain stimulation, 1*(2), 97-105.

Aristovich, K. Y., Packham, B. C., Koo, H., dos Santos, G. S., McEvoy, A., & Holder, D. S. (2016). Imaging fast electrical activity in the brain with electrical impedance tomography. *NeuroImage, 124*, 204-213.

Atkinson, M., & Bingman, C. (1997). Elemental composition of commercial seasalts. *Journal of Aquariculture and Aquatic Sciences, 8*(2), 39-43.

Balasubramanian, M., Mulkern, R. V., Wells, W. M., Sundaram, P., & Orbach, D. B. (2015). Magnetic resonance imaging of ionic currents in solution: the effect of magnetohydrodynamic flow. *Magnetic Resonance in Medicine, 74*(4), 1145-1155.

Bandettini, P., Petridou, N., & Bodurka, J. (2005). Direct detection of neuronal activity with MRI: fantasy, possibility, or reality? *Applied Magnetic Resonance, 29*(1), 65-88.

Barr, R. C., & Plonsey, R. (1995). Threshold variability in fibers with field stimulation of excitable membranes. *IEEE transactions on biomedical engineering, 42*(12), 1185-1191.

Bayford, R. H. (2006). Bioimpedance tomography (electrical impedance tomography). *Annu. Rev. Biomed. Eng., 8*, 63-91.

BeMent, S. L., & Ranck Jr, J. B. (1969). A quantitative study of electrical stimulation of central myelinated fibers.

Berridge, M. J., Lipp, P., & Bootman, M. D. (2000). The versatility and universality of calcium signalling. *Nature reviews Molecular cell biology, 1*(1), 11.

Beurrier, C., Bioulac, B., Audin, J., & Hammond, C. (2001). High-frequency stimulation produces a transient blockade of voltage-gated currents in subthalamic neurons. *Journal of neurophysiology, 85*(4), 1351-1356.

Bianciardi, M., Di Russo, F., Aprile, T., Maraviglia, B., & Hagberg, G. E. (2004). Combination of BOLD-fMRI and VEP recordings for spin-echo MRI detection of primary magnetic effects caused by neuronal currents. *Magnetic Resonance Imaging, 22*(10), 1429-1440.

Bitar, R., Leung, G., Perng, R., Tadros, S., Moody, A. R., Sarrazin, J., Nelson, A. (2006). MR pulse sequences: what every radiologist wants to know but is afraid to ask. *Radiographics, 26*(2), 513-537.

Bodurka, J., & Bandettini, P. A. (2002). Toward direct mapping of neuronal activity: MRI detection of ultraweak, transient magnetic field changes. *Magnetic Resonance in Medicine, 47*(6), 1052-1058.

Bodurka, J., Jesmanowicz, A., Hyde, J., Xu, H., Estkowski, L., & Li, S.-J. (1999). Current-induced magnetic resonance phase imaging. *Journal of Magnetic Resonance, 137*(1), 265-271.

Brown, P., & Eusebio, A. (2008). Paradoxes of functional neurosurgery: clues from basal ganglia recordings. *Movement Disorders, 23*(1), 12-20.

Burgess, R. (2014). Magnetoencephalography.

Cassarà, A. M., Hagberg, G. E., Bianciardi, M., Migliore, M., & Maraviglia, B. (2008). Realistic simulations of neuronal activity: a contribution to the debate on direct detection of neuronal currents by MRI. *NeuroImage, 39*(1), 87-106.

Chauhan, M., Indahlastari, A., Kasinadhuni, A. K., Schär, M., Mareci, T. H., & Sadleir, R. J. (2018). Low-Frequency Conductivity Tensor Imaging of the Human HeadIn VivoUsing DT-MREIT: First Study. *IEEE transactions on medical imaging, 37*(4), 966-976.

Chauhan, M., Vidya Shankar, R., Ashok Kumar, N., Kodibagkar, V. D., & Sadleir, R. (2018). Multishot echo‐planar MREIT for fast imaging of conductivity, current density, and electric field distributions. *Magnetic Resonance in Medicine, 79*(1), 71-82.

Chen, R., Classen, J., Gerloff, C., Celnik, P., Wassermann, E., Hallett, M., & Cohen, L. G. (1997). Depression of motor cortex excitability by low‐frequency transcranial magnetic stimulation. *Neurology, 48*(5), 1398-1403.

Chow, L. S., Cook, G. G., Whitby, E., & Paley, M. N. (2006). Investigation of MR signal modulation due to magnetic fields from neuronal currents in the adult human optic nerve and visual cortex. *Magnetic Resonance Imaging, 24*(6), 681-691.

Chow, L. S., Cook, G. G., Whitby, E., & Paley, M. N. (2007). Investigation of axonal magnetic fields in the human corpus callosum using visual stimulation based on MR signal modulation. *Journal of Magnetic Resonance Imaging, 26*(2), 265-273.

Chu, R., de Zwart, J. A., van Gelderen, P., Fukunaga, M., Kellman, P., Holroyd, T., & Duyn, J. H. (2004). Hunting for neuronal currents: absence of rapid MRI signal changes during visual-evoked response. *NeuroImage, 23*(3), 1059-1067.

Cogan, S. F. (2008). Neural stimulation and recording electrodes. *Annu. Rev. Biomed. Eng., 10*, 275-309.

Denk, W. (1994). Two-photon scanning photochemical microscopy: mapping ligand-gated ion channel distributions. *Proceedings of the National Academy of Sciences, 91*(14), 6629-6633.

Dittgen, T., Nimmerjahn, A., Komai, S., Licznerski, P., Waters, J., Margrie, T. W., Osten, P. (2004). Lentivirus-based genetic manipulations of cortical neurons and their optical and electrophysiological monitoring in vivo. *Proceedings of the National Academy of Sciences, 101*(52), 18206-18211.

Dominguez, G., & Fozzard, H. A. (1970). Influence of extracellular K+ concentration on cable properties and excitability of sheep cardiac Purkinje fibers. *Circulation Research, 26*(5), 565-574.

Dulhunty, A. (2006). Excitation–contraction coupling from the 1950s into the new millennium. *Clinical and Experimental Pharmacology and Physiology, 33*(9), 763-772.

Egert, U., & Meyer, T. (2005). Heart on a chip—extracellular multielectrode recordings from cardiac myocytes in vitro. *Practical Methods in Cardiovascular Research*, 432-453.

Faro, S. H., & Mohamed, F. B. (2006). *Functional MRI: basic principles and clinical applications*: Springer Science & Business Media.

Ferrari, M., Mottola, L., & Quaresima, V. (2004). Principles, techniques, and limitations of near infrared spectroscopy. *Canadian journal of applied physiology, 29*(4), 463-487.

Fiedler, T. M., Ladd, M. E., & Bitz, A. K. (2018). SAR simulations & safety. *NeuroImage, 168*, 33-58.

Filali, M., Hutchison, W. D., Palter, V. N., Lozano, A. M., & Dostrovsky, J. O. (2004). Stimulation-induced inhibition of neuronal firing in human subthalamic nucleus. *Experimental brain research, 156*(3), 274-281.

Filmer, H. L., Dux, P. E., & Mattingley, J. B. (2014). Applications of transcranial direct current stimulation for understanding brain function. *Trends in neurosciences, 37*(12), 742-753.

Foster, K. R., Bidinger, J. M., & Carpenter, D. (1976). The electrical resistivity of cytoplasm. *Biophys J, 16*(9), 991.

Frauenrath, T., Fuchs, K., Dieringer, M. A., Özerdem, C., Patel, N., Renz, W., Niendorf, T. (2012). Detailing the use of magnetohydrodynamic effects for synchronization of MRI with the cardiac cycle: a feasibility study. *Journal of Magnetic Resonance Imaging, 36*(2), 364-372.

Frazier, W. T., Kandel, E. R., Kupfermann, I., Waziri, R., & Coggeshall, R. E. (1967). Morphological and functional properties of identified neurons in the abdominal ganglion of Aplysia californica. *Journal of neurophysiology, 30*(6), 1288-1351.

Frostig, R. (2009). In Vivo Two-Photon Laser Scanning Microscopy with Concurrent Plasma-Mediated Ablation Principles and Hardware Realization--In Vivo Optical Imaging of Brain Function.

Fu, F., Chauhan, M., & Sadleir, R. (2018). The effect of potassium chloride on Aplysia Californica abdominal ganglion activity. *Biomedical Physics & Engineering Express, 4*(3), 035033.

Gradinaru, V., Mogri, M., Thompson, K. R., Henderson, J. M., & Deisseroth, K. (2009). Optical deconstruction of parkinsonian neural circuitry. *Science, 324*(5925), 354-359.

Grienberger, C., & Konnerth, A. (2012). Imaging calcium in neurons. *Neuron, 73*(5), 862-885.

Haas, K., Sin, W.-C., Javaherian, A., Li, Z., & Cline, H. T. (2001). Single-cell electroporationfor gene transfer in vivo. *Neuron, 29*(3), 583-591.

Hablitz, J. J., & Lundervold, A. (1981). Hippocampal excitability and changes in extracellular potassium. *Experimental neurology, 71*(2), 410-420.

Hagberg, G. E., Bianciardi, M., Brainovich, V., Cassarà, A. M., & Maraviglia, B. (2008). The effect of physiological noise in phase functional magnetic resonance imaging: from blood oxygen level-dependent effects to direct detection of neuronal currents. *Magnetic Resonance Imaging, 26*(7), 1026-1040.

Hagberg, G. E., Bianciardi, M., & Maraviglia, B. (2006). Challenges for detection of neuronal currents by MRI. *Magnetic Resonance Imaging, 24*(4), 483-493.

Hallett, M. (2007). Transcranial magnetic stimulation: a primer. *Neuron, 55*(2), 187-199.

Heekeren, H. R., Kohl, M., Obrig, H., Wenzel, R., von Pannwitz, W., Matcher, S. J., Villringer, A. (1999). Noninvasive assessment of changes in cytochrome-c oxidase oxidation in human subjects during visual stimulation. *Journal of Cerebral Blood Flow & Metabolism, 19*(6), 592-603.

Heilmaier, C., Theysohn, J. M., Maderwald, S., Kraff, O., Ladd, M. E., & Ladd, S. C. (2011). A large‐scale study on subjective perception of discomfort during 7 and 1.5 T MRI examinations. *Bioelectromagnetics, 32*(8), 610-619.

Helmchen, F., & Denk, W. (2005). Deep tissue two-photon microscopy. *Nature methods, 2*(12), 932.

Henriquez, C. S. (1993). Simulating the electrical behavior of cardiac tissue using the bidomain model. *Critical reviews in biomedical engineering, 21*(1), 1-77.

Hershey, T., Revilla, F., Wernle, A., McGee-Minnich, L., Antenor, J., Videen, T., Perlmutter, J. (2003). Cortical and subcortical blood flow effects of subthalamic nucleus stimulation in PD. *Neurology, 61*(6), 816-821.

Histed, M. H., Bonin, V., & Reid, R. C. (2009). Direct activation of sparse, distributed populations of cortical neurons by electrical microstimulation. *Neuron, 63*(4), 508-522.

Hodgkin, A. L., & Huxley, A. F. (1952). The dual effect of membrane potential on sodium conductance in the giant axon of Loligo. *The Journal of physiology, 116*(4), 497-506.

Hodgkin, A. L., & Huxley, A. F. (1952). A quantitative description of membrane current and its application to conduction and excitation in nerve. *The Journal of physiology, 117*(4), 500.

Hornak, J. P. (2008). The basics of MRI, 2008. *URL http://www. cis. rit. edu/htbooks/mri/index. html, 68*.

Huxley, A., & Stämpfli, R. (1951). Effect of potassium and sodium on resting and action potentials of single myelinated nerve fibres. *The Journal of physiology, 112*(3-4), 496-508.

Jeon, K., Minhas, A. S., Kim, Y. T., Jeong, W. C., Kim, H. J., Kang, B. T., Woo, E. J. (2009). MREIT conductivity imaging of the postmortem canine abdomen using CoReHA. *Physiol Meas, 30*(9), 957.

Jiang, X., Lu, H., Shigeno, S., Tan, L. H., Yang, Y., Ragsdale, C. W., & Gao, J. H. (2014). Octopus visual system: A functional MRI model for detecting neuronal electric currents without a blood‐oxygen‐level‐dependent confound. *Magnetic Resonance in Medicine, 72*(5), 1311-1319.

Kamei, H., Iramina, K., Yoshikawa, K., & Ueno, S. (1999). Neuronal current distribution imaging using magnetic resonance. *IEEE transactions on magnetics, 35*(5), 4109-4111.

Kasinadhuni, A., Indahlastari, A., Chauhan, M., Schär, M., Mareci, T., & Sadleir, R. (2017). Imaging of current flow in the human head during transcranial electrical therapy. *Brain stimulation, 10*(4), 764-772.

Keltner, J. R., Roos, M. S., Brakeman, P. R., & Budinger, T. F. (1990). Magnetohydrodynamics of blood flow. *Magnetic Resonance in Medicine, 16*(1), 139-149.

Khang, H. S., Lee, B. I., Oh, S. H., Woo, E. J., Lee, S. Y., Cho, M. H., Seo, J. K. (2002). J-substitution algorithm in magnetic resonance electrical impedance tomography (MREIT): phantom experiments for static resistivity images. *IEEE transactions on medical imaging, 21*(6), 695-702.

Kim, H. J., Kim, Y. T., Minhas, A. S., Jeong, W. C., Woo, E. J., Seo, J. K., & Kwon, O. J. (2009). In vivo high-resolutionconductivity imaging of the human leg using MREIT: the first human experiment. *IEEE transactions on medical imaging, 28*(11), 1681-1687.

Kim, H. J., Oh, T. I., Kim, Y. T., Lee, B. I., Woo, E. J., Seo, J. K., Kang, B. T. (2008). In vivo electrical conductivity imaging of a canine brain using a 3 T MREIT system. *Physiol Meas, 29*(10), 1145.

Kirson, E. D., Dbalý, V., Tovaryš, F., Vymazal, J., Soustiel, J. F., Itzhaki, A., Schneiderman, R. (2007). Alternating electric fields arrest cell proliferation in animal tumor models and human brain tumors. *Proceedings of the National Academy of Sciences, 104*(24), 10152-10157.

Kitamura, K., Judkewitz, B., Kano, M., Denk, W., & Häusser, M. (2008). Targeted patch-clamp recordings and single-cell electroporation of unlabeled neurons in vivo. *Nature methods, 5*(1), 61.

Ko, J. H., Tang, C. C., & Eidelberg, D. (2013). Brain stimulation and functional imaging with fMRI and PET. *Handb. Clin. Neurol., 116*, 77-65.

Konn, D., Gowland, P., & Bowtell, R. (2003). MRI detection of weak magnetic fields due to an extended current dipole in a conducting sphere: a model for direct detection of neuronal currents in the brain. *Magnetic Resonance in Medicine, 50*(1), 40-49.

Konn, D., Leach, S., Gowland, P., & Bowtell, R. (2004). Initial attempts at directly detecting alpha wave activity in the brain using MRI. *Magnetic Resonance Imaging, 22*(10), 1413-1427.

Krug, J. W., Rose, G., Clifford, G. D., & Oster, J. (2013). ECG-based gating in ultra high field cardiovascular magnetic resonance using an independent component analysis approach. *Journal of Cardiovascular Magnetic Resonance, 15*(1), 104.

Kuo, M.-F., Paulus, W., & Nitsche, M. A. (2014). Therapeutic effects of non-invasive brain stimulation with direct currents (tDCS) in neuropsychiatric diseases. *NeuroImage, 85*, 948-960.

Kwon, O., Woo, E. J., Yoon, J.-R., & Seo, J. K. (2002). Magnetic resonance electrical impedance tomography (MREIT): simulation study of J-substitution algorithm. *IEEE transactions on biomedical engineering, 49*(2), 160-167.

Ladd, M. E., Bachert, P., Meyerspeer, M., Moser, E., Nagel, A. M., Norris, D. G., Zaiss, M. (2018). Pros and cons of ultra-high-field MRI/MRS for human application. *Progress in nuclear magnetic resonance spectroscopy, 109*, 1-50.

Lapicque, L. (1901). Definition experimentale de l'excitabilite. *Soc Biol., 77*, 280-283.

Lendvai, B., Stern, E. A., Chen, B., & Svoboda, K. (2000). Experience-dependent plasticity of dendritic spines in the developing rat barrel cortex in vivo. *Nature, 404*(6780), 876.

Liang, Z.-P., & Lauterbur, P. C. (2000). *Principles of magnetic resonance imaging: a signal processing perspective*: SPIE Optical Engineering Press.

Lilly, J. C., Hughes, J. R., Alvord Jr, E. C., & Galkin, T. W. (1955). Brief, noninjurious electric waveform for stimulation of the brain. *Science*.

Lipton, M. L. (2010). *Totally accessible MRI: a user's guide to principles, technology, and applications*: Springer Science & Business Media.

Lozano, A. M., Dostrovsky, J., Chen, R., & Ashby, P. (2002). Deep brain stimulation for Parkinson's disease: disrupting the disruption. *The Lancet Neurology, 1*(4), 225-231.

Lu, K. P., & Means, A. R. (1993). Regulation of the cell cycle by calcium and calmodulin. *Endocrine reviews, 14*(1), 40-58.

Luo, Q., & Gao, J. H. (2010). Modeling magnitude and phase neuronal current MRI signal dependence on echo time. *Magnetic Resonance in Medicine, 64*(6), 1832-1837.

Luo, Q., Jiang, X., Chen, B., Zhu, Y., & Gao, J. H. (2011). Modeling neuronal current MRI signal with human neuron. *Magnetic Resonance in Medicine, 65*(6), 1680-1689.

Malenka, R. C., Kocsis, J. D., Ransom, B. R., & Waxman, S. G. (1981). Modulation of parallel fiber excitability by postsynaptically mediated changes in extracellular potassium. *Science, 214*(4518), 339-341.

Malmivuo, J., & Plonsey, R. (1995). *Bioelectromagnetism: principles and applications of bioelectric and biomagnetic fields*: Oxford University Press, USA.

McRobbie, D. W., Moore, E. A., Graves, M. J., & Prince, M. R. (2017). *MRI from Picture to Proton*: Cambridge university press.

Meister, M., Pine, J., & Baylor, D. A. (1994). Multi-neuronal signals from the retina: acquisition and analysis. *Journal of neuroscience methods, 51*(1), 95-106.

Merrill, D. R., Bikson, M., & Jefferys, J. G. (2005). Electrical stimulation of excitable tissue: design of efficacious and safe protocols. *Journal of neuroscience methods, 141*(2), 171-198.

Mezrich, R. (1995). A perspective on K-space. *Radiology, 195*(2), 297-315.

Minhas, A. S., Chauhan, M., Fu, F., & Sadleir, R. (2018). Evaluation of magnetohydrodynamic effects in magnetic resonance electrical impedance tomography at ultra‐high magnetic fields. *Magnetic Resonance in Medicine*.

Minhas, A. S., Jeong, W.-C., Kim, Y.-T., Kim, H.-J., Lee, T.-H., & Woo, E.-J. (2008). MREIT of postmortem swine legs using carbon-hydrogel electrodes. *Journal of Biomedical Engineering Research, 29*(6), 436-442.

Minhas, A. S., Kim, H. H., Meng, Z. J., Kim, Y. T., Kim, H. J., & Woo, E. J. (2011). Three-dimensional MREIT simulator of static bioelectromagnetism and MRI. *Biomedical Engineering Letters, 1*(2), 129-136.

Moliadze, V., Atalay, D., Antal, A., & Paulus, W. (2012). Close to threshold transcranial electrical stimulation preferentially activates inhibitory networks before switching to excitation with higher intensities. *Brain stimulation, 5*(4), 505-511.

Montgomery Jr, E. B., & Gale, J. T. (2008). Mechanisms of action of deep brain stimulation (DBS). *Neuroscience & Biobehavioral Reviews, 32*(3), 388-407.

Muftuler, L. T., Hamamura, M. J., Birgul, O., & Nalcioglu, O. (2006). In vivo MRI electrical impedance tomography (MREIT) of tumors. *Technology in cancer research & treatment, 5*(4), 381-387.

Mulleners, W., Chronicle, E., Palmer, J., Koehler, P., & Vredeveld, J. (2001). Suppression of perception in migraine evidence for reduced inhibition in the visual cortex. *Neurology, 56*(2), 178-183.

Nakada, T. (2007). Clinical application of high and ultra high-field MRI. *Brain and Development, 29*(6), 325-335.

Nicoll, R. (1979). Dorsal root potentials and changes in extracellular potassium in the spinal cord of the frog. *The Journal of physiology, 290*(2), 113-127.

Nitsche, M., Fricke, K., Henschke, U., Schlitterlau, A., Liebetanz, D., Lang, N., Paulus, W. (2003). Pharmacological modulation of cortical excitability shifts induced by transcranial direct current stimulation in humans. *The Journal of physiology, 553*(1), 293-301.

Nitsche, M. A., Boggio, P. S., Fregni, F., & Pascual-Leone, A. (2009). Treatment of depression with transcranial direct current stimulation (tDCS): a review. *Experimental neurology, 219*(1), 14-19.

Nitsche, M. A., Kuo, M.-F., Karrasch, R., Wächter, B., Liebetanz, D., & Paulus, W. (2009). Serotonin affects transcranial direct current–induced neuroplasticity in humans. *Biological psychiatry, 66*(5), 503-508.

Nitsche, M. A., Liebetanz, D., Schlitterlau, A., Henschke, U., Fricke, K., Frommann, K., . . . Tergau, F. (2004). GABAergic modulation of DC stimulation ‐ induced motor cortex excitability shifts in humans. *European Journal of Neuroscience, 19*(10), 2720-2726.

Nitsche, M. A., Seeber, A., Frommann, K., Klein, C. C., Rochford, C., Nitsche, M. S., Antal, A. (2005). Modulating parameters of excitability during and after transcranial direct current stimulation of the human motor cortex. *The Journal of physiology*, *568*(1), 291-303.

Nowak, L., & Bullier, J. (1998). Axons, but not cell bodies, are activated by electrical stimulation in cortical gray matter I. Evidence from chronaxie measurements. *Experimental brain research, 118*(4), 477-488.

Nowak, L. G., & Bullier, J. (1996). Spread of stimulating current in the cortical grey matter of rat visual cortex studied on a new in vitro slice preparation. *Journal of neuroscience methods, 67*(2), 237-248.

Ogawa, S., Lee, T.-M., Kay, A. R., & Tank, D. W. (1990). Brain magnetic resonance imaging with contrast dependent on blood oxygenation. *Proceedings of the National Academy of Sciences, 87*(24), 9868-9872.

Oh, S. H., Lee, B. I., Woo, E. J., Lee, S. Y., Cho, M. H., Kwon, O., & Seo, J. K. (2003). Conductivity and current density image reconstruction using harmonic Bz algorithm in magnetic resonance electrical impedance tomography. *Physics in Medicine & Biology, 48*(19), 3101.

Oh, T. I., Kim, Y. T., Minhas, A., Seo, J. K., Kwon, O. I., & Woo, E. J. (2011). Ion mobility imaging and contrast mechanism of apparent conductivity in MREIT. *Physics in Medicine & Biology, 56*(7), 2265.

Orrenius, S., Zhihotovsky, B., & Nicotera, P. Regulation of cell death: the calcium-apoptosis link. Nature Rev Cell Biol 2003; 4: 552-65.

Park, C., Lee, B. I., Kwon, O., & Woo, E. J. (2006). Measurement of induced magnetic flux density using injection current nonlinear encoding (ICNE) in MREIT. *Physiol Meas, 28*(2), 117.

Park, T. S., Lee, S. Y., Park, J.-H., Cho, M. H., & Lee, S. Y. (2006). Observation of the fast response of a magnetic resonance signal to neuronal activity: a snail ganglia study. *Physiol Meas, 27*(2), 181.

Pascual-Leone, A., Valls-Solé, J., Wassermann, E. M., & Hallett, M. (1994). Responses to rapid-rate transcranial magnetic stimulation of the human motor cortex. *Brain, 117*(4), 847-858.

Perrey, S., & Ferrari, M. (2017). Muscle oximetry in sports science: a systematic review. *Sports Medicine*, 1-20.

Peters, A. M., Brookes, M. J., Hoogenraad, F. G., Gowland, P. A., Francis, S. T., Morris, P. G., & Bowtell, R. (2007). T2* measurements in human brain at 1.5, 3 and 7 T. *Magnetic Resonance Imaging, 25*(6), 748-753.

Pichon, Y., & Treherne, J. (1976). The effects of osmotic stress on the electrical properties of the axons of a marine osmoconformer (Mala squinado. brachyura: crustacea). *Journal of Experimental Biology, 65*(3), 553-563.

Pinti, P., Tachtsidis, I., Hamilton, A., Hirsch, J., Aichelburg, C., Gilbert, S., & Burgess, P. W. (2018). The present and future use of functional near‐infrared spectroscopy (fNIRS) for cognitive neuroscience. *Annals of the New York Academy of Sciences*.

Plewes, D. B., & Kucharczyk, W. (2012). Physics of MRI: a primer. *Journal of Magnetic Resonance Imaging, 35*(5), 1038-1054.

Plonsey, R., & Barr, R. C. (2007). Bioelectricity: a quantitative approach. *Springer Science & Business Media*.

Polanía, R., Nitsche, M. A., Korman, C., Batsikadze, G., & Paulus, W. (2012). The importance of timing in segregated theta phase-coupling for cognitive performance. *Current Biology, 22*(14), 1314-1318.

Pouratian, N., Sheth, S., Bookheimer, S. Y., Martin, N. A., & Toga, A. W. (2003). Applications and limitations of perfusion-dependent functional brain mapping for neurosurgical guidance. *Neurosurgical focus, 15*(1), 1-8.

Quigg, M., & Quigg, M. (2006). *EEG pearls*: Mosby Elsevier.

Ruff, C. C., Driver, J., & Bestmann, S. (2009). Combining TMS and fMRI: from 'virtual lesions' to functional-network accounts of cognition. *Cortex, 45*(9), 1043-1049.

Sadleir, R., Grant, S., Zhang, S. U., Lee, B. I., Pyo, H. C., Oh, S. H., Kwon, O. (2005). Noise analysis in magnetic resonance electrical impedance tomography at 3 and 11 T field strengths. *Physiol Meas, 26*(5), 875.

Sadleir, R. J., Fu, F., & Chauhan, M. (2019). Functional magnetic resonance electrical impedance tomography (f MREIT) sensitivity analysis using an active bidomain finite‐element model of neural tissue. *Magnetic Resonance in Medicine, 81*(1), 602-614.

Sadleir, R. J., Fu, F., Falgas, C., Holland, S., Boggess, M., Grant, S. C., & Woo, E. J. (2017). Direct detection of neural activity in vitro using magnetic resonance electrical impedance tomography (MREIT). *NeuroImage, 161*, 104-119.

Sadleir, R. J., Grant, S. C., & Woo, E. J. (2010). Can high-field MREIT be used to directly detect neural activity? Theoretical considerations. *NeuroImage, 52*(1), 205-216.

Segev, R., Puchalla, J., & Berry, M. J. (2006). Functional organization of ganglion cells in the salamander retina. *Journal of neurophysiology, 95*(4), 2277-2292.

Seo, J. K., Yoon, J.-R., Woo, E. J., & Kwon, O. (2003). Reconstruction of conductivity and current density images using only one component of magnetic field measurements. *IEEE transactions on biomedical engineering, 50*(9), 1121-1124.

Shin, D., Samoilova, M., Cotic, M., Zhang, L., Brotchie, J., & Carlen, P. (2007). High frequency stimulation or elevated K+ depresses neuronal activity in the rat entopeduncular nucleus. *Neuroscience, 149*(1), 68-86.

Stagg, C. J., & Nitsche, M. A. (2011). Physiological basis of transcranial direct current stimulation. *The Neuroscientist, 17*(1), 37-53.

Stefurak, T., Mikulis, D., Mayberg, H., Lang, A. E., Hevenor, S., Pahapill, P., Lozano, A. (2003). Deep brain stimulation for Parkinson's disease dissociates mood and motor circuits: a functional MRI case study. *Movement disorders: official journal of the Movement Disorder Society, 18*(12), 1508-1516.

Strangman, G., Boas, D. A., & Sutton, J. P. (2002). Non-invasive neuroimaging using near-infrared light. *Biological psychiatry, 52*(7), 679-693.

Sullivan, G. M., & Feinn, R. (2012). Using effect size—or why the P value is not enough. *Journal of graduate medical education, 4*(3), 279-282.

Svoboda, K., Denk, W., Kleinfeld, D., & Tank, D. W. (1997). In vivo dendritic calcium dynamics in neocortical pyramidal neurons. *Nature, 385*(6612), 161.

Tehovnik, E. J. (1996). Electrical stimulation of neural tissue to evoke behavioral responses. *Journal of neuroscience methods, 65*(1), 1-17.

Truong, T.-K., Avram, A., & Song, A. W. (2008). Lorentz effect imaging of ionic currents in solution. *Journal of Magnetic Resonance, 191*(1), 93-99.

Tung, L. (1978). *A bi-domain model for describing ischemic myocardial dc potentials.* Massachusetts Institute of Technology.

Udupa, K., & Chen, R. (2015). The mechanisms of action of deep brain stimulation and ideas for the future development. *Progress in neurobiology, 133*, 27-49.

Uğurbil, K. (2014). Magnetic resonance imaging at ultrahigh fields. *IEEE transactions on biomedical engineering, 61*(5), 1364-1379.

Vigmond, E., Dos Santos, R. W., Prassl, A., Deo, M., & Plank, G. (2008). Solvers for the cardiac bidomain equations. *Progress in biophysics and molecular biology, 96*(1-3), 3-18.

Wagner, T., Fregni, F., Fecteau, S., Grodzinsky, A., Zahn, M., & Pascual-Leone, A. (2007). Transcranial direct current stimulation: a computer-based human model study. *NeuroImage, 35*(3), 1113-1124.

Wassermann, E. M. (1998). Risk and safety of repetitive transcranial magnetic stimulation: report and suggested guidelines from the International Workshop on the Safety of Repetitive Transcranial Magnetic Stimulation, June 5–7, 1996. *Electroencephalography and Clinical Neurophysiology/Evoked Potentials Section, 108*(1), 1-16.

Wassermann, E. M., McShane, L. M., Hallett, M., & Cohen, L. G. (1992). Noninvasive mapping of muscle representations in human motor cortex. *Electroencephalography and Clinical Neurophysiology/Evoked Potentials Section, 85*(1), 1-8.

Woods, A. J., Bryant, V., Sacchetti, D., Gervits, F., & Hamilton, R. (2015). Effects of electrode drift in transcranial direct current stimulation. *Brain stimulation, 8*(3), 515-519.

Xiong, J., Fox, P. T., & Gao, J. H. (2003). Directly mapping magnetic field effects of neuronal activity by magnetic resonance imaging. *Human brain mapping, 20*(1), 41-49.

Xue, Y., Gao, J.-H., & Xiong, J. (2006). Direct MRI detection of neuronal magnetic fields in the brain: theoretical modeling. *NeuroImage, 31*(2), 550-559.

Yücel, M. A., Selb, J. J., Huppert, T. J., Franceschini, M. A., & Boas, D. A. (2017). Functional near infrared spectroscopy: Enabling routine functional brain imaging. *Current opinion in biomedical engineering, 4*, 78-86.

Yaksi, E., & Friedrich, R. W. (2006). Reconstruction of firing rate changes across neuronal populations by temporally deconvolved Ca 2+ imaging. *Nature methods, 3*(5), 377.

Ziemann, U., Rothwell, J. C., & Ridding, M. C. (1996). Interaction between intracortical inhibition and facilitation in human motor cortex. *The Journal of physiology*, *496*(3), 873-881.

APPENDIX A

VARIABLES USED FOR ANALYSIS

Variable		Definition
M	M^{NC}	Magnitude image of MR scan without current injection
	$M^{+/-}$	Magnitude image of MR scan with positive/ negative current injection
Φ	Φ^{NC}	Phase image of MR scan without current injection
	$\Phi^{+/-}$	Phase image of MR scan with positive/ negative current injection
	Φ^{Bz}	MREIT phase image
μ_M		Mean value of the ROI in magnitude image
μ_Φ		Mean value of the ROI in phase image
σ_Φ		SD of the ROI in phase image
μ_{μ_M}		$\mu_{\mu_M} = (\sum_{i=1}^{n} \mu_{M_{(i)}})/n$
σ_{μ_M}		$\sigma_{\mu_M} = \sqrt{\frac{\sum_{i=1}^{n}(\mu_{M_{(i)}} - \mu_{\mu_M})}{n-1}}$
μ_{μ_Φ}		$\mu_{\mu_\Phi} = (\sum_{i=1}^{n} \mu_{\Phi(i)})/n$
μ_{σ_Φ}		$\mu_{\sigma_\Phi} = (\sum_{i=1}^{n} \sigma_{\Phi(i)})/n$
$\nabla^2\Phi$		Laplacian of phase image
$\mu_{\nabla^2\Phi}$		Mean value of ROI in Laplacian of phase image
$\sigma_{\nabla^2\Phi}$		SD of ROI in Laplacian of phase image
$\mu_{\mu_{\nabla^2\Phi}}$		$\mu_{\mu_{\nabla^2\Phi}} = (\sum_{i=1}^{n} \mu_{\nabla^2\Phi(i)})/n$
$\mu_{\sigma_{\nabla^2\Phi}}$		$\mu_{\sigma_{\nabla^2\Phi}} = (\sum_{i=1}^{n} \sigma_{\nabla^2\Phi(i)})/n$
Sd(Φ)		$sd(\Phi) = \frac{\sqrt{2}}{\gamma}$
s_Φ		$s_\Phi = \frac{1}{\sqrt{\frac{20}{\Delta^4}}} s_{\nabla^2\Phi}$
γ		SNR
μ_γ		Mean value of SNR
σ_γ		SD of SNR
$\Delta\Phi$		Differential phase image
$\mu_{\Delta\Phi}$		Mean value of differential phase image
$\sigma_{\Delta\Phi}$		SD of differential phase image
$\Delta\nabla^2\Phi$		Differential Laplacian of phase image
$\mu_{\Delta\nabla^2\Phi}$		Mean value of differential Laplacian of phase image
$\sigma_{\Delta\nabla^2\Phi}$		SD of differential Laplacian of phase image
$\mu_{\sigma_{\Delta\nabla^2\Phi}}$		$\mu_{\sigma_{\Delta\nabla^2\Phi}} = (\sum_{i=1}^{n} \sigma_{\Delta\nabla^2\Phi(i)})/n$
$\mu_{\Delta\Phi}^{Norm}$		Mean of the normal distribution of differential phase image
$\sigma_{\Delta\Phi}^{Norm}$		SD of the normal distribution of differential phase image
$\mu_{\Delta\nabla^2\Phi}^{Norm}$		Mean of normal distribution of differential Laplacian of phase image
$\sigma_{\Delta\nabla^2\Phi}^{Norm}$		SD of normal distribution of differential Laplacian of phase image